



HAL
open science

Functionalized semiconducting oxides based on bismuth vanadate with anchored organic dye molecules for photoactive applications

Karolina Ordon

► **To cite this version:**

Karolina Ordon. Functionalized semiconducting oxides based on bismuth vanadate with anchored organic dye molecules for photoactive applications. Physics [physics]. Le Mans Université; Uniwersytet Humanistyczno-Przyrodniczy im. Jana Długosza w Częstochowie, 2018. English. NNT : 2018LEMA1006 . tel-01849209

HAL Id: tel-01849209

<https://theses.hal.science/tel-01849209>

Submitted on 25 Jul 2018

HAL is a multi-disciplinary open access archive for the deposit and dissemination of scientific research documents, whether they are published or not. The documents may come from teaching and research institutions in France or abroad, or from public or private research centers.

L'archive ouverte pluridisciplinaire **HAL**, est destinée au dépôt et à la diffusion de documents scientifiques de niveau recherche, publiés ou non, émanant des établissements d'enseignement et de recherche français ou étrangers, des laboratoires publics ou privés.

THESE DE DOCTORAT DE

LE MANS UNIVERSITE

COMUE UNIVERSITE BRETAGNE LOIRE

ECOLE DOCTORALE N° 596

Matière, Molécules, Matériaux

Spécialité : « *Physique* »

Karolina ORDON

« Functionalized semiconducting oxides based on bismuth vanadate with anchored organic dye molecules for photoactive applications »

Thèse présentée et soutenue à « Université JD Czestochowa », le « 28 Juin 2018 »

Unité de recherche : Institut des Molécules et Matériaux du Mans

Thèse N° : 2018LEMA1006

Rapporteurs avant soutenance :

Ahmad MEHDI, Professeur Institut Charles Gerhardt UMR-CNRS, Université de Montpellier, France

Jaroslav MYSLIWIEC Professeur, Département de Physique et Chimie Théorique, Université de Wrocław, Pologne

Composition du Jury :

Jacek KASPERCZYK Professeur, Institut de Physique, Université Jan Dlugosz à Czestochowa, Pologne (Président du Jury)

Ahmad MEHDI Professeur Institut Charles Gerhardt UMR-CNRS, Université de Montpellier, France (Rapporteur)

Jaroslav MYSLIWIEC Professeur, Département de Physique et Chimie Théorique, Université de Wrocław, Pologne (Rapporteur)

Zorica BRANKOVIC, Professeur, Institut de Recherche Multidisciplinaire, Université de Belgrade, Serbie (Examinatrice)

Malgorzata MAKOWSKA-JANUSIK Professeur, Institut de Physique, Université Jan Dlugosz à Czestochowa, Pologne (Directeur de Thèse)

Abdel Hadi KASSIBA, Professeur, Institut des Molécules et Matériaux du Mans, UMR-CNRS, Le Mans Université, France (Directeur de Thèse)

Titre Oxydes Semi-conducteurs à base de bismuth vanadates fonctionnalisés par des colorants organiques pour des applications en photocatalyse

Mots clés : BiVO₄ Mésoporeux, Photocatalyse, Matériaux hybrides

La recherche de nouveaux matériaux en tant que photocatalyseurs en lumière visible pour la dépollution de l'environnement (eaux, atmosphères) est un domaine de recherche très actif et suscite l'intérêt d'une large communauté scientifique en Physique, Chimie et Sciences des matériaux. Des recherches exhaustives sont actuellement menées pour améliorer l'efficacité photocatalytique de certaines classes de matériaux photoactifs connus, et pour développer la synthèse de nouveaux matériaux fonctionnels. Dans ce contexte, les semi-conducteurs oxydes photoactifs à base de vanadates de bismuth (BiVO₄) possédant une bande électronique au milieu du spectre visible, offrent une sérieuse alternative aux photocatalyseurs classiques efficaces (TiO₂, ZnO) dont la photo-excitation requiert uniquement la fraction UV du spectre solaire. Le travail effectué dans le cadre de cette thèse est donc dédié aux matériaux à base BiVO₄ sous forme d'architectures mésoporeuses ou d'assemblages hybrides associant des groupes organiques à transfert de charges.

Deux contributions majeures ont été développées dont la première portant sur la réalisation expérimentale d'architectures mésoporeuses inédites, fonctionnalisées par des groupes organiques sensibilisateurs et l'étude de leurs propriétés électroniques et optiques en vue d'optimiser leurs efficacités photocatalytiques. La deuxième partie porte sur des simulations numériques de nanostructures hybrides par des approches exploitant la méthode DFT, *ab-initio* ou des modèles de chimie quantique. Des systèmes modèles ont été construits associant des nanoclusters (NC) et des groupes organiques (GO). Les propriétés électroniques et optiques ainsi que les caractéristiques structurelles et vibrationnelles des systèmes (NC-GO) ont été déterminées et confrontées aux données expérimentales. Les phénomènes de transfert de charges impliqués entre les groupes organiques et la structure inorganique ont été caractérisés ainsi que leur rôle dans l'efficacité des réponses photo-catalytiques des systèmes hybrides

Functionalized semiconducting oxides based on bismuth vanadate with anchored organic dye molecules for photoactive applications

Keywords : Mesoporous BiVO₄ , Photocatalysis, Hybrid Materials

The search for new materials as photocatalysts in visible light for the depollution of the environment (waters, atmospheres) is a very active field of research and attracts the interest of a large scientific community in Physics, Chemistry and Materials Science. Recent research developments are conducted to improve the photocatalytic efficiency of certain classes of known photoactive materials, and to develop the synthesis of new functional materials. In this context, photoactive oxide semiconductors based on bismuth vanadate (BiVO₄) having an electronic band in the middle of the visible spectrum, offer a serious alternative to efficient conventional photocatalysts (TiO₂, ZnO) whose photo-excitation requires only the UV fraction of the solar spectrum. The work done in this thesis is therefore dedicated to BiVO₄-based materials in the form of mesoporous architectures or hybrid assemblies associating organic groups with charge transfer processes.

Two major contributions have been developed, one of which is the experimental realization of novel mesoporous architectures, functionalized by sensitizing organic groups and the study of their electronic and optical properties in order to optimize their photocatalytic efficiencies. The second part deals with numerical simulations of hybrid nanostructures using approaches as the DFT method, *ab-initio* or quantum chemistry codes. Model systems have been constructed associating BiVO₄ nanoclusters (NC) and organic groups (GO). The electronic and optical properties as well as the structural and vibrational characteristics of the systems (NC-GO) were determined and compared with the experimental data. The charge transfer phenomena involved between the organic groups and the inorganic structure were characterized as well as their role in the efficiency of photo-catalytic responses of hybrid systems

Acknowledgement

First and foremost I want to thank my supervisor **Prof. Malgorzata Makowska-Janusik**, the person without whom this thesis would never come to life. She has been a constant source of guidance and support during every stage of my research work. Her constant feedback helped me in honing my knowledge. At the same time, I would like to thank my co-supervisor **Prof. Abdelhadi Kassiba** for inspiration for experimental research, irreplaceable help in planning experiments and creative approach in finding solutions to research problems. I would also like to thank him for help in editing my work and motivation for further development. It has been an honor to be their Ph.D. student.

I am particularly grateful for the assistance given by **Dr. Sandrine Coste, Dr. Olivier Noël, Prof. Alain Bulou** and all those who have helped me to realize the experimental part of my work.

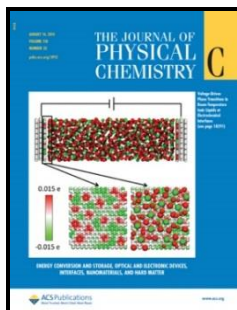
I would like to express my gratitude to **Prof. Barbara Morzyk-Ociepa** for help during the PhD studies in Poland.

I am also grateful to my friends for their support, in particular **Lucia Mydlova, Karolina Dysz, Renata Majgier, Tetiana Babuka, Mina Ider** and **Victor Merupo**.

I would especially like to thank my **Mother** for her patience, forbearance and unlimited support in every situation.

I dedicate the Thesis to my Grandmother

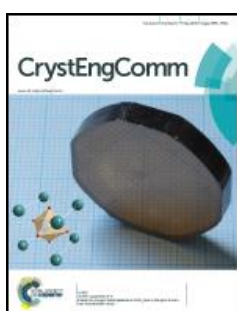
List of publications



Imen Guezgue, Awatef Ayad, Karolina Ordon, Konstantinos Iliopoulos, Diana G. Branzea, Anna Migalska-Zalas, Malgorzata Makowska-Janusik, Abdelkrim El-Ghayoury, Bouchta Sahraoui

Zinc induced a dramatic enhancement of the non-linear optical properties of an azo-based iminopyridine ligand

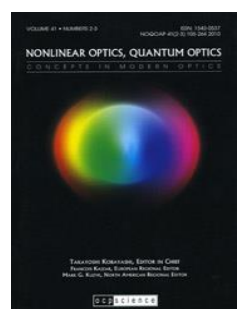
J. Phys. Chem. C **2014**, 118, 7545–7553



Victor-Ishrayelu Merupo, Subramaniam Velumani, Karolina Ordon, Nicolas Errien, Jacek Szade, Abdel-Hadi Kassiba

Structural and optical characterizations of ball milled copper doped bismuth vanadium oxide (BiVO₄)

CrystEngComm **2015**, 17, 3366-3375



M. Makowska-Janusik, K. Ordon, R.Jaroszewicz

Effect of the PEK Polymer Matrix on the NLO

Properties of Guest Chromophores - Computational Approach

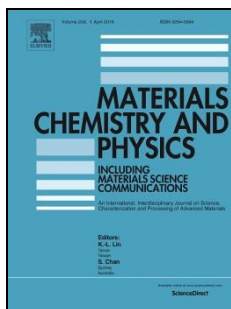
Nonlinear Optics and Quantum Optics **2015**, 47, 33-44



K. Ordon, A. Kassiba and M. Makowska-Janusik

Electronic, optical and vibrational features of BiVO₄ nanostructures investigated by first-principles calculations

RSC Adv. **2016**, 6, 110695–110705



R. Venkatesana, S. Velumani, K. Ordon, M. Makowska-Janusik, G. Corbel, A. Kassiba
Nanostructured bismuth vanadate (BiVO_4) thin films for efficient visible light photocatalysis
Materials Chemistry and Physics **2018**, 205, 325-333

Prize and Awards

1. Excellence grant program **EIFFEL**, Le Mans, France, 2015/2016, annual scholarship for scientific research
2. The prize for the best oral presentation *Semiconducting hybrid systems based on bismuth vanadate sensitized organics dyes to photocatalytic applications*, XX National Conference Molecular Crystals, 12-16 September 2016, Kazimierz Dolny, Poland
3. Grant **PRELUDIUM** from National Center of Sciences, Poland, No. 2016/21/N/ST3/00455, *Photocatalytic properties of mesoporous hybrid materials based on bismuth vanadate*, 2017-2018, project manager

Participation in the conferences

Oral communications:

1. Karolina Ordon, Abdel Hadi Kassiba, Małgorzata Makowska-Janusik, *Photocatalytic properties of BiVO₄ - theoretical and experimental studies*, The IInd National Conference of "Between the Sciences" Congress of Physicists and Chemists, 26th September 2014, Chorzow, Poland
2. Karolina Ordon, *Bismuth vanadate photocatalytic alternatives for titanium dioxide*, The VIIth The conference of young scientists - The influence of the young scientists on achievements of Polish Science, 6th December 2014, Krakow, Poland
3. Karolina Ordon, Małgorzata Makowska-Janusik, Abdel Hadi Kassiba, *Doping and adding organic dye to BiVO₄-change of the electronic properties*, International conference of students and young researchers in theoretical and experimental physics HEUREKA, 13-15 May 2015, Lviv, Ukraine
4. Karolina Ordon, Małgorzata Makowska-Janusik, Abdel Hadi Kassiba, *Photocatalytic property of BiVO₄- theoretical and experimental studies*, The XXth International Seminar on Physics and Chemistry of Solids, 13-16 September 2015, Lviv, Ukraine
5. Karolina Ordon, Małgorzata Makowska-Janusik, Abdel Hadi Kassiba, *The impact of the doping of the bismuth vanadate to the electronic properties of those systems*, The IIIrd National Conference of "Between the Sciences" Congress of Physicists and Chemists, 18th September 2015, Chorzow, Poland
6. Karolina Ordon, Małgorzata Makowska-Janusik, Abdel Hadi Kassiba, *Mesoporous BiVO₄ thin film for photocatalytic applications: experimental and theoretical studies*, XXVth International Materials Research Congress (IMRC), 14-19 August 2016, Cancun, Mexico
7. Karolina Ordon, Małgorzata Makowska-Janusik, Abdel Hadi Kassiba, *Semiconducting hybrid systems based on bismuth vanadate sensitized organics dyes to photocatalytic applications*, XX National Conference Molecular Crystals, 12-16 September 2016, Kazimierz Dolny, Poland

8. Karolina Ordon, Małgorzata Makowska-Janusik, Abdel Hadi Kassiba, *Analysis of the photocatalytic properties of the thin film of mesoporous materials based on bismuth vanadate*, The 59th Meeting of The Polish Chemical Society and The Society of Engineers and Technicians of Chemical Industry, 19-23 September 2016, Poznan, Poland
9. Karolina Ordon, *Hybrid materials based on BiVO₄ activated organic molecules for photocatalytic applications*, II Forum Młodych, 13th June 2017, Czestochowa, Poland
10. Karolina Ordon, Sandrine Coste, Małgorzata Makowska-Janusik, Abdel Hadi Kassiba, *Mesoporous BiVO₄ thin films as efficient visible light driven photocatalyst*, 2nd International Conference on Sustainable Materials Science and Technology (SMST17), 19-21 July 2017 Las Palmas, Spain
11. Karolina Ordon, Małgorzata Makowska-Janusik, Abdel Hadi Kassiba, *Bismuth vanadate photocatalyst of the future*, The IV National Conference of "Between the Sciences" Congress of Physicists and Chemists, 10-15th September 2017 Chorzow, Poland
12. Karolina Ordon, Małgorzata Makowska-Janusik, Abdel Hadi Kassiba, *Analysis of the functional semiconducting materials based on the Bismuth Vanadate with anchored organic dye molecules*, The 22nd International Conference on Semiconductor Photocatalysis and Solar Energy Conversion SPASEC-22, 13-16.11.2017 Florida, USA

Posters:

1. Karolina Ordon, Małgorzata Makowska-Janusik, *Environmental effects on the NLO properties of organic composite materials*, XIXth International Seminar on Physics and Chemistry of solids and advanced materials, 12-15 June 2013, Czestochowa, Poland
2. Karolina Ordon, Abdelhadi Kassiba, Małgorzata Makowska-Janusik, *Photocatalytic properties of BiVO₄ - theoretical and experimental studies*, 57th Meeting of The Polish Chemical Society and The Society of Engineers and Technicians of Chemical Industry, 14-18 September 2014, Czestochowa, Poland
3. Karolina Ordon, Małgorzata Makowska-Janusik, Abdel Hadi Kassiba, *Photoactive semiconducting oxides (TiO₂, BiVO₄), doping and anchored dyes effects: numerical simulations approaches and experiments*, XXV International Materials Research Congress (IMRC), 14-19 August 2016, Cancun, Mexico
4. Karolina Ordon, Małgorzata Makowska-Janusik, Abdel Hadi Kassiba, *Analysis of electronic, structural and optical properties of hybrid systems based on bismuth vanadate activated with organic dyes*, 44. Congress of Polish Physicists, 10-15 September 2017 Wroclaw, Poland

Abbreviations

Å - Ångström (10^{-10} m)

GPa - Gigapascal

kHz- kilohertz

keV- kiloelectron-volt

µm- micrometer

nm - nanometer

pm - picometre

mW- milliwatt

mV- millivolt

EDA - Ethylenediamine

EDTA - Ethyl Enediamin Etetra Acetic

EG - Ethylene Glycol

MB - Methylene Blue

MO - Methyl orange

O_2^- - Super oxygen radicals

OH^- - Hydroxyl radicals

P123- Poly(ethylene glycol)-block-
poly(propylene glycol)-block-
poly(ethylene glycol) PVP -
Polyvinyl Pyrrolidone

RhB - Rhodamine B

AFM - Atomic Force Microscope

CVD - Chemical Vapor Deposition

IR - Infrared

KFM - Kelvin Probe Force Microscopy

PC - Photocatalyst

PDT - Photodynamic Therapy

SEM - Scanning Electron Eicroscope

STM - Scanning Tunnelling Microscope

UV - Ultraviolet

XRD - X-Ray Diffraction

Vis - Visible Light

A - Absorbance

α - Absorption coefficient

U - Accelerating voltage

A_A - Acceptor electron affinity

$\delta_{as}(VO_4^{3-})$ - Asymmetric deformation

Z - Atomic number

e - Charge of an electron

C - Concentration

CBM - Conducting band minimum

CB - Conduction Band

V_{CPD} - Contact potential difference

l_c - Critical length

D- π -A - Donor- π -acceptor

I_D - Donor ionization energy

e^- - Electron

E_n - Electron levels

m_0 - Electron rest mass

m_e^* - Effective mass of an electron

m_h^* - Effective mass of a hole

E_g - Energy of band gap

E_e - Energy of the electrons

E_{os} - Energy of oscillation

E_{rot} - Energy of rotation

EF - Fermi level

EF_{D-A} - Fermi pinning level

FWHM - Full width at half maximum

HOMO - Highest Occupied Molecular
Orbital

h^+ - Hole

HD - Hybrid system (BiVO₄)₁₈/D149

HL - Hybrid system
(BiVO₄)₁₈/LIGAND

HC - Hybrid system
(BiVO₄)₁₈/COMPLEX

ν_0 - Incident radiation at frequencies

LUMO - Lowest Unoccupied Molecular
Orbital

m_e - Mass of the electron

ϵ_{max} - Molar absorption coefficient

h - Planck constant

ΔV - potential difference

R - Reflectance

RT- Room temperature

I_n - Rotational levels

$\delta_s(VO_4^{3-})$ - Symmetric deformation

T- Transmittance

λ_{max} - Wavelength of absorption
maximum

λ - Wavelength of light

Φ_A^- - Work function acceptor

Φ_D^+ - Work function donor

Φ_{point} - Work function of the tip

Φ_{sample} - Work function of the sample

VB - Valence Band
VBM - Valence band maximum

B3LYP - Becke, three-parameter,
Lee-Yang-Parr
BFGS - Broyden-Fletcher-Goldfarb-
Shanno algorithm
E_{cut-off} - Energy Cut-off
GGA - Generalized Gradient
Approximation
KS - Kohn-Sham equation
LDA - Local Density Approximation
PBE - Perdew-Burke-Ernzerhof
functional
PCM - Polarizable Continuum Model
PDOS - Partial Electron Density of
States
PM3 - Parameterized Model number 3
PM6 - Parameterization Method 6
PPP - Pariser-Parr-Pople method
RHF - Restricted Hartree-Fock
RMS - Root Mean Square
SCF - Self-Consistent Field
QA - Quadratic Approximation

V_n - Vibration levels
 J_{ij} - Coulomb integrals
 \hat{W} - Coulomb interaction operator
 E_{XC} - Correlation-exchange energy
 $v_{xc}(r)$ - Correlation-exchange potential
 \vec{v}_{ef} - Effective potential
 $\rho(r)$ - Electron density
 E_n - Energy of the state n
 K_{ij} - Exchange integrals
 \hat{T} - Kinetic energy operator
 \hat{H} - Hamilton operator
 ∇ - Nabla symbol
 r_i, r_j - Position of the i and j electrons
 a_i - Primitive vectors of the lattice
F - Reduced density gradient
 \vec{G} - Space vector
 φ_i - Spinorbital
 Ψ_n - Wave function
 \vec{k} - Wave vector
 R_k, R_l - Vectors of the k and l nuclei
positions

Contents:

Chapter 1 Introduction	1
1.1. Photocatalytic phenomena and applications.....	2
1.2. Photoactive semiconducting oxides.....	5
1.2.1. Oxide materials for photocatalysis.....	5
1.2.2. Role of the material morphology and nano-structuration in the photocatalytic efficiency.....	8
1.2.3. Physical features of bismuth vanadate (BiVO ₄).....	10
1.2.4. Synthesis methods of the BiVO ₄ and related samples morphologies.....	14
1.2.4. Photocatalytic properties of the bulk and thin films BiVO ₄ systems.....	18
1.3. Peculiarities of hybrid systems in photoactive processes.....	24
1.4. Conclusions.....	26
1.5. References.....	27
Chapter 2 Quantum-chemical calculations	43
2.1. Hartree-Fock methodology.....	45
2.2. Density functional theory (DFT).....	47
2.2.1. Generalized gradient approximation (GGA).....	49
2.2.2. Perdew-Burke-Ernzerhof (PBE) functional.....	50
2.3. Plane-wave method.....	51
2.3.1. Born-von Karman boundary conditions.....	52
2.4. Semi-empirical methods in quantum chemistry.....	53
2.5. References.....	54

Chapter 3 Characterization techniques	57
3.1. X-ray diffractions (XRD).....	57
3.2. Scanning electron microscopy (SEM).....	60
3.3. Atomic force microscopy (AFM).....	64
3.4. Kelvin probe force microscopy (KFM).....	66
3.5. UV-visible Spectrophotometry.....	68
3.6. Raman spectroscopy.....	72
3.7. Photocatalytic test.....	74
3.8. References.....	77

Thesis and Hypothesis	81
------------------------------	-----------

Chapter 4 Physico-chemistry of BiVO₄	83
4.1. Synthesis of the mesoporous BiVO ₄	83
4.2. Hybrid composites based on mesoporous BiVO ₄ with anchored dyes.....	86
4.3. References.....	87

Chapter 5 Results and discussion	89
5.1. Quantum-chemical calculations and experimental investigations of the BiVO ₄ in bulk and nanosized form.....	89
5.1.1. Electronic and structural properties.....	89
5.1.2. UV-Vis absorption spectra of mesoporous BiVO ₄ films.....	104
5.1.3. Analysis of the active vibrations using IR and Raman spectroscopy.....	107
5.1.4. Study of the photocatalytic properties.....	112
5.1.5. Conclusions.....	114
5.2. Quantum-chemical calculations and experimental investigations of semiconducting-organic hybrid systems.....	116
5.2.1. Analysis of the structure and electronic properties.....	116
5.2.2. Optical properties of BiVO ₄ /dye thin films.....	126
5.2.3. Impact of anchored organic dye molecules on the Raman activity.....	127
5.2.4. Photocatalytic properties of the hybrid systems.....	129

5.2.5. Conclusions.....	130
5.3. References.....	131

Chapter 6 General Conclusions 138

List of Figures.....	145
List of Tables.....	149
List of Schemas.....	151

Abstract

Photoactivated processes are involved in several phenomena and serve as the basis of technological applications in different domains such as eco-construction, energy, environment, medicine, optoelectronics or cosmetology. Among the whole range of photoactivated processes, the key part lies in the photocatalytic reactions. Therefore, photoactive materials are used under radiations within defined spectral ranges contributing inter alia to photodynamic therapy, the production of self-cleaning glasses, hydrogen production for new sources of energy as well as in eco-friendly water purification from harmful organic pollutants.

From the pioneer work of Fujishima et al. (*Nature* 1979, 277, 637–638), the most commonly used semiconductors in photocatalysis is titanium dioxide (TiO_2). An alternatives to the TiO_2 were searched based on ZnO materials (*Chem. Rev.* 1995, 95, 69-96). Unfortunately, due to the high values of their band gap they cannot absorb visible light radiation limiting then their applications. Therefore, the search of new materials as visible light photocatalysts has attracted a wide research community. Among the promising systems, the monoclinic bismuth vanadate (BiVO_4) with energy gap equal to 2.4 eV is proposed as an alternative to the mentioned materials because it can harvest large fraction of the solar visible light radiations. Nowadays, exhaustive investigations are carried out to improve the properties of some families of known photocatalytic materials, as well as to develop the synthesis of new functional materials that would replace classic photocatalysts. Among numerous methods, the photocatalytic properties of semiconducting oxides can be improved by increasing their active surfaces, a narrowing of their band gap as well as the use of photoactive organic dyes to sensitize the inorganic semiconducting surfaces.

The aim of the presented work is to realize mesoporous architectures based on bismuth vanadate and to investigate an influence of selected organic sensitizers on the electronic, optical, vibrational and photocatalytic properties of the monoclinic BiVO_4 . The increase of the active surface area was proposed as the first element improving the photocatalytic properties of the crystalline BiVO_4 . For this purpose, the BiVO_4 was synthesized in a mesoporous form applying an original approach based on the P123 surfactant. Then, the structural, electronic and optical properties of the obtained materials were exhaustively

investigated and optimized. It was found that the mesoporous BiVO_4 is a good starting material to obtain an efficient photocatalyst. In addition, it was determined that the synthesis of hybrid materials by anchoring organic dye molecules on a surface of the mesoporous BiVO_4 will allow a more efficient transfer of electric charge between the organic molecule and inorganic oxide positively affecting its photocatalytic properties. Therefore, commercial D149 and two new dyes based on imino-pyridine moieties were selected as the organic sensitizers and their performances compared in the process of photoinduced charge transfer .

In order to determine the mechanisms of physical phenomena responsible for photocatalytic effects occurring in hybrid materials, a series of computer simulations and quantum-chemical calculations were performed. Applying the cluster methodology the electronic and optical parameters as well as structural and vibrational features of nanostructured BiVO_4 were calculated. The considered simulations were also performed for organic dyes and hybrid materials using a semi-empirical method with the PM6 parameterization. The obtained results from computer simulations were compared to the experimental data in order to validate the relevance of the developed theoretical models. Thus, based on computer simulations through quantum-chemical methods and the carried out experimental works, the involved charge transfer phenomena were characterized in the aim to understand the transfer of electric charges in the hybrid material and the effect of the photocatalytic responses. The role of dyes in enhancing the photocatalytic effects for some organic groups or a quenching of such effects by using other molecules was also explained. It was shown that the combination of experimental and theoretical research methods leads to quantitative understanding of the physical phenomena governing the photocatalytic properties of the photoactive semiconducting structures as BiVO_4 .

The performed work develops a relevant methodology applied on a promising class of photoactive materials for visible-light driven photocatalysis. The numerical approaches offer the support of experimental investigations for exhaustive understanding of the phenomena involved in the photoinduced charge transfer efficiency in the hybrid systems. The works associate complementary expertise contributions of two research teams responsible for quantum-chemical calculations carried out at the Jan Dlugosz University in Czestochowa (Poland) and the experimental developments of relevant materials features carried out at Le Mans University (France). The results of the present

work were disseminated by publishing in high impact journals and by communications during international conferences.

Streszczenie

Procesy fotoaktywowane stanowią ważną grupę zjawisk wykorzystywanych w wielu zastosowaniach technologicznych w eko-budownictwie, elektronice, inżynierii materiałowej i środowiska, medycynie i kosmetologii. Materiały fotoaktywne działające w zakresie światła widzialnego oraz w nadfiolecie stosowane są między innymi w terapii fotodynamicznej, jako nowoczesne źródła energii, do produkcji szkieł samoczyszczących jak również podczas przyjaznego dla środowiska oczyszczania wody ze szkodliwych związków organicznych. Wśród całej gamy procesów fotoaktywowanych, kluczową część stanowi fotokataliza.

Dotychczas, jednym z najczęściej wykorzystywanych w fotokatalizie półprzewodników jest dwutlenek tytanu (TiO_2), którego właściwości zostały opisane w pionierskiej pracy Fujishima i współpracowników (*Nature* 1979, 277, 637–638). Prowadzone były również badania nad poszukiwaniem materiałów alternatywnych na bazie tlenek cynku (ZnO) (*Chem. Rev.* 1995, 95, 69-96). Niestety, ze względu na duże wartości wzbronionej przerwy energetycznej wymienione materiały nie mogą absorbować promieniowania w zakresie światła widzialnego, co znacząco ogranicza ich stosowalność. Alternatywą dla ZnO i TiO_2 może okazać się jednoskośna odmiana wanadanu bizmutu (BiVO_4), który posiada wzbronioną przerwę energetyczną równą 2,4 eV dla postaci objętościowej, co pozwala wykorzystać światło widzialne jako źródło fotoaktywacji. Obecnie prowadzone są badania mające na celu poprawienie właściwości znanych materiałów fotokatalitycznych, jak również syntezę nowych materiałów funkcjonalnych, które zastąpiłyby klasyczne fotokatalizatory. Wśród licznych sposobów poprawy właściwości fotokatalitycznych półprzewodników tlenkowych, na uwagę zasługuje zwiększenie ich powierzchni czynnej, zmniejszenie wzbronionej przerwy energetycznej oraz aktywowanie ich barwnikami organicznymi.

Celem niniejszej pracy jest zbadanie wpływu wybranych sensybilizatorów organicznych na właściwości elektronowe, optyczne, wibracyjne oraz fotokatalityczne jednoskośnego BiVO_4 o strukturze mezoporowatej w odniesieniu do materiału objętościowego. Jako pierwszy element poprawiający właściwości fotokatalityczne krystalicznego BiVO_4 zastosowano zwiększenie jego powierzchni czynnej. W tym celu zsyntezowano wymieniony materiał w postaci mezoporowatej stosując pionierską

metodę wykorzystującą surfaktant P123. Następnie przeprowadzono analizę własności strukturalnych, elektronowych i optycznych otrzymanych materiałów. Stwierdzono, że badany BiVO_4 jest dobrą bazą do stworzenia wydajnego fotokatalizatora. Ponadto ustalono, że synteza materiałów hybrydowych poprzez zakotwiczenie cząsteczek barwnika organicznego na powierzchni BiVO_4 pozwoli na bardziej wydajny transfer ładunku elektrycznego pomiędzy molekułą organiczną a nieorganicznym tlenkiem, co również wpłynie pozytywnie na jego własności fotokatalityczne. W związku z tym jako barwniki organiczne wybrano komercyjny D149 oraz dwa barwniki na bazie iminopirydyny.

W celu określenia mechanizmów zjawisk fizycznych, zachodzących w materiałach hybrydowych, odpowiadających za efekty fotokatalityczne przeprowadzono szereg symulacji komputerowych i obliczeń kwantowo-chemicznych. Obliczono parametry elektronowe i optyczne jak również strukturalne i wibracyjne nanostruktur BiVO_4 w podejściu klasterowym. Wymienione symulacje prowadzono także dla barwników organicznych i badanych materiałów hybrydowych wykorzystując metodę półempiryczną z parametryzacją PM6. Jako weryfikator poprawności stosowanych modeli teoretycznych korzystano z porównań wyników badań teoretycznych z danymi eksperymentalnymi.

Na drodze symulacji komputerowych oraz prac doświadczalnych stwierdzono, że zwiększenie powierzchni czynnej BiVO_4 oraz sensybilizowanie go barwnikami organicznymi polepszyło transfer ładunków elektrycznych w materiale hybrydowym, co pozytywnie wpłynęło na poprawienie własności fotokatalitycznych badanego materiału. Wyjaśniono również, dlaczego niektóre barwniki wpływają pozytywnie na efekty fotokatalityczne zachodzące w materiałach hybrydowych a inne wręcz je gaszą i mogą służyć jako inhibitory powierzchniowych reakcji chemicznych. Obliczenia kwantowo-chemiczne obrazujące wpływ poszczególnych komponentów układu hybrydowego na jego własności elektronowe dały możliwość wyjaśnienia mechanizmu fotoindukowanego transferu ładunku elektrycznego zachodzącego w materiale barwnik/nanostruktura. Pokazano, że dzięki połączeniu eksperymentalnych i teoretycznych metod badawczych można otrzymać pełny obraz zjawisk fizycznych rządzących właściwościami fotokatalitycznymi BiVO_4 .

Prace badawcze wykonane w ramach niniejszej rozprawy pozwoliły rozwinąć metodologię badawczą oraz analizę zjawisk fizycznych zachodzących w materiałach fotokatalitycznych na bazie BiVO_4 pracujących w zakresie światła widzialnego.

Wykonane prace numeryczne były wsparciem dla badań eksperymentalnych pozwalającym wyjaśnić fotoindukowane zjawiska fizyczne zachodzące w półprzewodniku, wpływające na zwiększenie efektywności transferu ładunku w systemach hybrydowych. Niniejsza praca jest wynikiem współpracy dwóch zespołów badawczych, z których jeden był odpowiedzialny za obliczenia kwantowo-chemiczne prowadzone na Akademii im. Jana Długosza w Częstochowie (Polska) oraz drugi z Uniwersytetu Le Mans (Francja), w którym prowadzono prace eksperymentalne oraz syntezę badanych materiałów. Wyniki naukowe referowanych badań opublikowano w znaczących czasopiśmie naukowych oraz przedstawiono na międzynarodowych konferencjach.

Résumé

Les procédés photocatalytiques sont mises en œuvre dans plusieurs phénomènes physico-chimiques et servent de base à des applications technologiques dans différents domaines tels que l'écoconstruction, l'énergie, l'environnement, la médecine, l'optoélectronique, la cosmétologie. L'ensemble de ces procédés fait intervenir des réactions catalytiques impliquant différentes classes de matériaux semi-conducteurs voire métalliques. Dans ce cadre, les matériaux photoactifs sont utilisés sous rayonnements dans des gammes spectrales adaptées à la structure électronique des matériaux. Ceci contribue notamment à des applications en thérapie photodynamique, dans la production de verres autonettoyants, la production d'hydrogène pour de nouvelles sources d'énergie et à la purification des eaux polluées. D'après le travail pionnier de Fujishima et al. (*Nature* 1979, 277, 637), les semi-conducteurs les plus étudiés pour la photocatalyse sont le dioxyde de titane (TiO_2). Une alternative au TiO_2 a été recherchée sur la base de matériaux ZnO (*Chem Rev.* 1995, 95, 69). Cependant, en raison des valeurs élevées de leur bande interdite, ils ne peuvent pas absorber les rayonnements de la lumière visible, ce qui limite leurs performances pour exploiter le rayonnement solaire. La recherche de nouveaux matériaux en tant que photocatalyseurs en lumière visible a attiré une large communauté de chercheurs en sciences des matériaux. Parmi les systèmes prometteurs, les vanadates de bismuth de structure monoclinique sheelite (BiVO_4) possédant une bande électronique égale à 2,4 eV peut s'avérer comme une alternative aux matériaux large bande car ils peuvent absorber une grande partie du rayonnement solaire. Aussi, des recherches exhaustives sont actuellement menées pour améliorer les propriétés de certaines classes de matériaux photocatalytiques connus, ainsi que pour développer la synthèse de nouveaux matériaux fonctionnels qui remplaceraient les photocatalyseurs classiques. Parmi les nombreuses méthodes, les propriétés photocatalytiques des oxydes semi-conducteurs peuvent être améliorées en augmentant leurs surfaces actives notamment par une nanostructuration, ou en contribuant à un rétrécissement de leur bande interdite par dopage ou par l'utilisation de colorants organiques photo-actifs pour sensibiliser les surfaces semi-conductrices inorganiques. Ainsi, le but du travail effectué dans le cadre de cette thèse

est de réaliser des architectures mésoporeuses à base de vanadates de bismuth et d'étudier l'influence de certains sensibilisateurs organiques sur les propriétés structurale, morphologiques, électroniques, optiques et photocatalytiques du BiVO_4 à structure monoclinique sheelite. L'augmentation de la surface active via les structures mésoporeuses a été proposée comme premier élément améliorant les propriétés photocatalytiques du BiVO_4 cristallin. Dans ce but, le BiVO_4 a été synthétisé sous une forme mésoporeuse en appliquant une approche originale basée sur le tensioactif P123. Ensuite, les propriétés structurales, électroniques et optiques des matériaux obtenus ont été étudiées et optimisées de manière exhaustive. Il a été montré que le BiVO_4 mésoporeux est un bon matériau de départ pour obtenir un photocatalyseur efficace. La synthèse de matériaux hybrides en greffant des molécules de colorants organiques sur la surface du BiVO_4 mésoporeux a été effectuée. Les propriétés du transfert de charges induit ont été étudiés pour évaluer leurs effets sur les propriétés photocatalytiques. Ainsi, le colorant organique D149 commercial et deux nouveaux colorants originaux basés sur des fragments imino-pyridine ont été sélectionnés en tant que sensibilisateurs organiques potentiels et leurs performances comparées sur le processus de transfert de charges.

Afin d'élucider les phénomènes physiques responsables des effets photocatalytiques survenant dans les matériaux hybrides, des simulations numériques par les méthodes de chimie quantique ont été réalisées. En appliquant la méthodologie de simulation de nanoclusters, les paramètres électroniques et optiques ainsi que les caractéristiques structurales et vibrationnelles du BiVO_4 nanostructuré ont été calculées. Les simulations considérées ont également été réalisées pour des colorants organiques associés aux structures inorganiques en utilisant une méthode semi-empirique avec le paramétrage PM6. Les résultats obtenus à partir de simulations ont été comparés aux données expérimentales afin de valider la pertinence des modèles théoriques développés. Ainsi, à partir de ces travaux, les phénomènes de transfert de charges impliqués entre les groupes organiques et la structure inorganique ont été caractérisés ainsi que les réponses photo-catalytiques des systèmes hybrides. En conclusion, le travail effectué développe une méthodologie pertinente appliquée à une classe prometteuse de matériaux photoactifs incluant leurs variantes hybrides dédiées à des applications à la photocatalyse en lumière visible. Les approches numériques offrent le support pour une compréhension exhaustive des investigations expérimentales dans le but d'optimiser l'efficacité des réponses photocatalytiques.

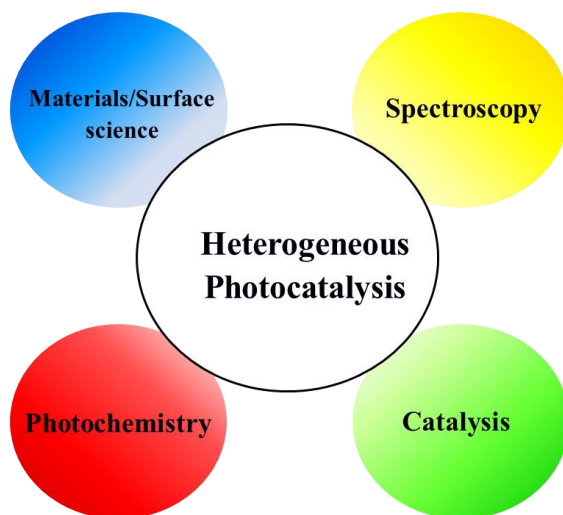
Les travaux associent les expertises complémentaires de deux équipes de recherche en matière de simulation par des méthodes de chimie quantique à l'Institut de Physique de l'université Jan Dlugosz de Czestochowa (Pologne) et l'expérimentation à l'Institut de molécules et matériaux (CNRS) à Le Mans Université (France). Il convient de souligner que l'ensemble de ces travaux ont été valorisés dans des publications dans des journaux internationaux à fort impact et dans des communications dans des conférences internationales.

Chapter 1

Introduction

Recently researchers gave the hope that photocatalysis is the phenomenon which can be used to purify water and air from pollutants. It is an ambition that the photoactivation can be achieved for non-toxic and eco-friendly compounds as be some semiconducting oxides. These materials can be activated by light resulting in decomposition of organic pollutants to small, non-toxic molecules like water and carbon dioxide. Photocatalytic phenomena have their origin in a photochemistry, heterogeneous catalysis, molecular spectroscopy, solid state physics, materials science and surface science of semiconductors. The interpenetration of the physics fields on which photocatalysis is based is presented in **Schema 1.1**

First time the word „photocatalysis” was used in 1910 by Plotnikow [1]. Today, the photocatalysis describes the processes activated by ultraviolet, visible or infrared radiation on the surface of the substance called „photocatalyst” (PC).



Schema 1.1. The system of dependencies of physics fields on which photocatalysis is based

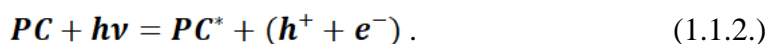
1. Photocatalytic phenomena and applications

According to IUPAC definition, photocatalysis describes a change of the speed of chemical reactions or its initiation under influence of a radiation from UV to IR range. The mentioned reaction occurs on a substrate called photocatalyst, which is able to absorb incident radiation. Photocatalyst promotes the reaction under an influence of light and it is not degraded during photocatalysis [2].

The heterogeneous photocatalysis deals with the interaction between the photocatalyst in solid state and liquid or gas phase of reagents and substrates. The first step of the photocatalytic reaction is an absorption of the incident radiation by the photocatalyst. When the photon of radiation energy is equal or slightly higher than the band gap of the photocatalyst, the electron-hole ($h^+ + e^-$) pairs are created with the electrons in the conduction band and the holes in the valence band. **Equation 1.1.1.** describes the relationship between the band gap and the wavelength necessary to excite electrons in the semiconducting material.

$$\lambda = \frac{1240}{E_g} \text{ (unit)}. \quad (1.1.1.)$$

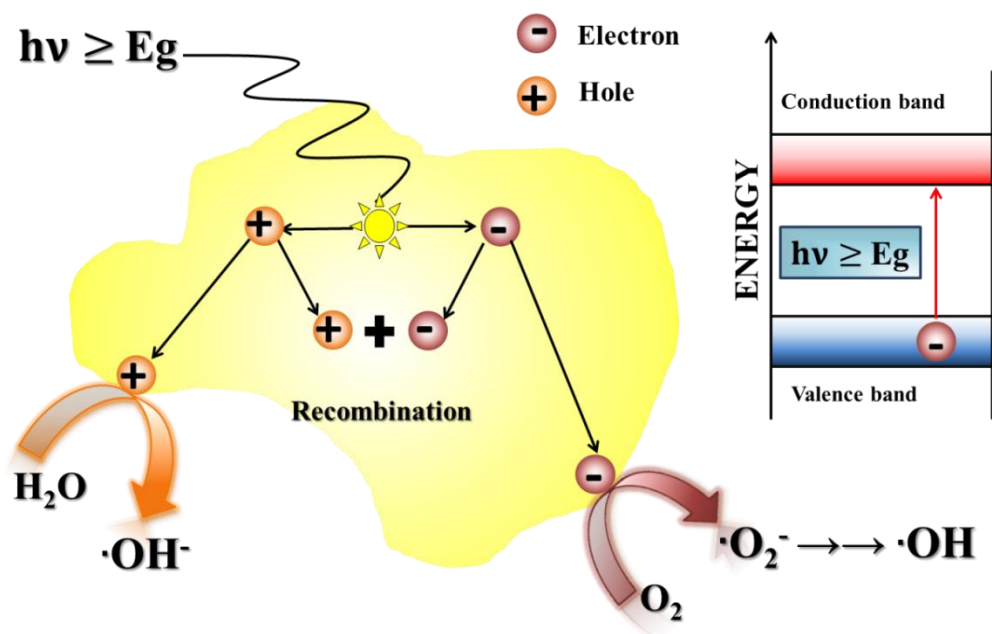
The process can be described by following expression:



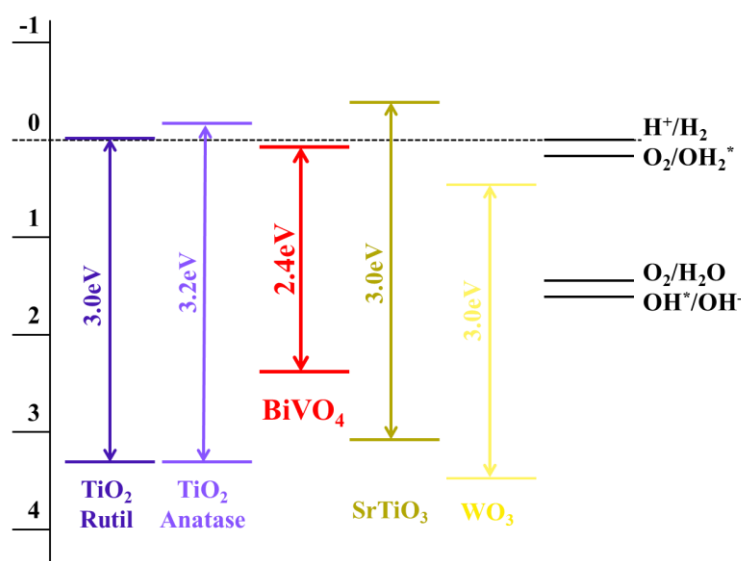
The electron-hole pairs generation took place in all PC volume reached by the light with the required energy. The reaction with the environment occurs when the electrons and hole are at the surface of photocatalyst. Therefore, when the migration time of the electrons and holes to the surface of photocatalyst will be shorter than the time of the recombination, the efficiency of the photocatalytic process will be higher. Thus, the ($h^+ + e^-$) pairs lifetime plays a key role in the PC efficiency. **Schema 1.1.1.** illustrates the process that take place at the semiconducting PC activated by radiation with energy adapted for its energy band gap [3].

The organic or biological molecules adsorbed on the PC surface can be oxidized when their redox potential is located above the valence band of the semiconductor. The reduction process occurs when the redox potential of the substrate is below the conduction band of photocatalyst.

Schema 1.1.2. compares the valence and conduction bands for selected photocatalysts relative to the redox potentials of hydrogen and oxygen [4].



Schema 1.1.1. Processes occurring in the semiconductor after absorption of suitable radiation



Schema 1.1.2. Location of valence and conduction band for the selected semiconducting oxides used as photocatalysts and redox potentials for water species

The photoactive semiconducting materials are used to purify water and air from harmful organic substances as dyes, carboxylic acids and their derivatives, aromatic compounds, pesticides, etc. [5,6].

The photocatalytic reactions are used to create hydrogen from water splitting as new energy source or alternatively to decompose waste organic molecules on a window panels. In medicine, photoactive compounds are used in photodynamic therapy applied for cancer treatment.

The photoactive materials are also used in dye sensitized solar cell (DSSC) systems known as the 3rd generation photovoltaic cells. Purification properties of the photocatalysts allow safe and friendly degradation of toxic substances through their mineralisation as nontoxic inorganic molecules including water and carbon dioxide. During the photoactivation process the catalytic material creates active radicals able to decompose organic compounds in reduction and oxidation processes [7,8]. Photocatalytic decomposition process may be also used in production of the hydrogen from water, biomass and monohydroxyl or polihydroxy alcohols. The hydrogen generated in this process serves as substrate in chemical reaction: production hydrogen chloride, methanol, ammonia or synthetic gasoline as well as fuel for a new type of hydrogen powered cars.

Self-cleaning surfaces are built with hydrophilic-photocatalytic coating. Photoinduced reactions occurring in the coating benefit from their activation by solar radiation. The process leads to decomposition of surface organic pollutants and prevents their adhesion at the coating layer. Glasses with such photoactive surfaces are installed on the skyscrapers and high rise buildings for practical reasons [9]. One example worthy of interest concerns the facade of a Mexican hospital in a polluted environment. The entire building was covered by the film of the semiconducting titanium dioxide as photocatalyst. The photocatalytic decomposition of pollutants from air turned out to be good solution for smog in the centre of Mexico City [10].

Photoactive materials contribute also to therapeutic solutions as illustrated in the photodynamic therapy (PDT). This form of medical treatment uses photosensitive materials acting on cancer cells after their exposure to radiation. The PDT process also has the ability to kill microorganisms, including bacteria, fungi and viruses. The method has found application in treatment of many diseases including malignant tumours. It was considered as low invasive and minimal toxic medical treatment strategy [11-14]. Photovoltaic devices are also a key illustration of photoactive materials for solar to electrical energy conversion.

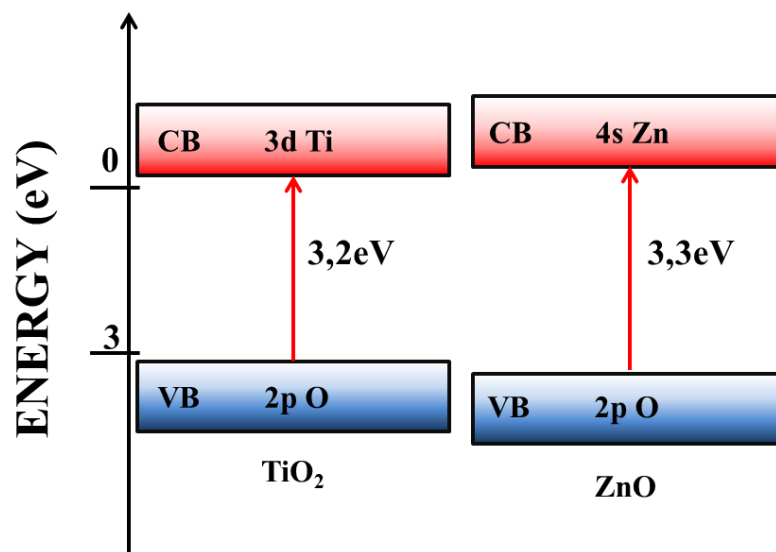
Dye sensitized solar cells (DSSC) combine semiconducting materials with organic dye molecules in the way to possess adequate charge transfer between the two components in the aim to obtain the highest conversion efficiency compared to actual reached values about 15% [15-17].

1.2. Photoactive semiconducting oxides

In photocatalytic processes, semiconducting oxides are widely exploited because of their suitable physical peculiarities. Even limited to oxides, the number of relevant composition is wide. In this case a limitation of the purpose to the most investigated materials with respect to their efficiency and their promising applications in visible light driven photocatalysts will be applied. Beyond the photoactivity, the nontoxic nature, chemical stability and environmental friendliness are major requirement from photocatalysts to be used in applications according to the environmental preservation.

1.2.1. Oxide materials for photocatalysis

So far, relevant and representative semiconducting oxides for photoactive applications are zinc oxides (ZnO) and titanium dioxides (TiO₂). Their valence band (VB) is mainly composed from 2p orbitals of oxygen atoms, whereas metal d orbitals contribute to the conduction band (CB) (**Schema 1.2.1.1**)



Schema 1.2.1.1 Band structure of the zinc oxide and titanium dioxide [18,19]

Zinc oxide shows two structural variants as hexagonal wurtzite and cubic zinc blende lattice. The second structure is most stable at ambient conditions and thus the most commonly used. Its space group is the $P6_3mc$ and the point group is the C_{6v}^4 . In this form, ZnO possesses a direct band gap equal to 3,37 eV and it can absorb radiation with wavelength about 375 nm [20] corresponding to the maximum absorption in the near ultraviolet.

The shift of absorption maximum to higher wavelengths can be made by doping or sensitizing process [21]. The doping operations use metallic elements as Mn [22], Ag [23], La [24], Cu [25], Mg [26], Co [27] and non-metallic ones as C [28] or N [29]. Among the improvement, it is worth noting that the absorption spectra of the ZnO doped by the Cu_2O coincide with the solar spectrum (**Fig. 1.2.1.1.**) [30]. It was also shown that the mentioned doping increases the photovoltaic efficiency of the ZnO. A similar impact was induced by carbon nanofibers [31] as sensitizing agent for the ZnO based photocatalyst (**Fig. 1.2.1.2.**).

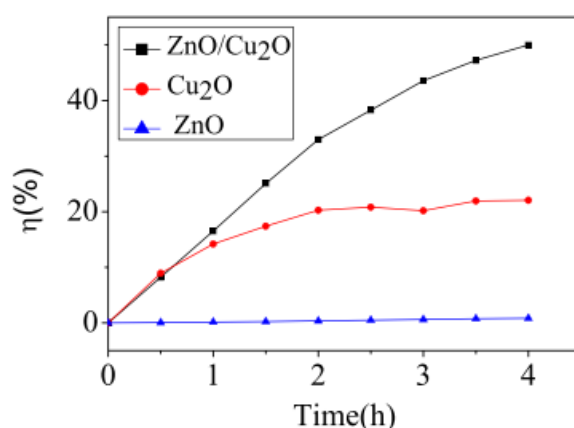


Figure 1.2.1.1. Photocatalytic efficiency of ZnO/ Cu_2O based photocatalysts in the photodegradation of methyl orange [30]

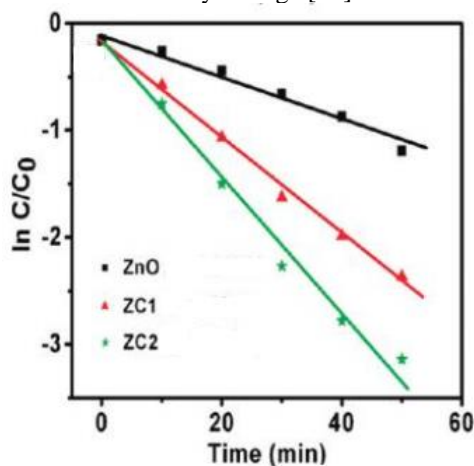


Figure 1.2.1.2. Rates of photocatalytic degradation of Rhodamine B concentration $[C(t)]$ by ZnO/carbon nanofiber (mass ratio ZnO: carbon electrospun nanofibers for ZC1- 4:1 and ZC2- 8:1) [31]

Titanium dioxide (TiO₂) is among the most popular photocatalyst. It crystallizes in three structural variants: anatase, rutile and brookite form.

For photocatalytic reactions, the most commonly used polymorph consists in the anatase form, which shows a direct band gap equal to 3,2 eV. In a similar way as the ZnO, pure TiO₂ presents limitation in harvesting a wide spectral range radiation due to its limited absorption only in the UV range. Over the years, many research teams investigated the properties of titanium dioxide in the aim to increase its activity in the visible light by introducing a variety of dopants into photocatalyst. In 2001, Asahi et al. published the study describing the photocatalytic activity under visible radiation, investigated for the TiO₂ doped by nitrogen anions. According to the authors, the introduction of an admixture into the structure of TiO₂ should lead to:

- the occurrence of additional energy states in the band gap area of photocatalyst that will allow the absorption of visible light by a photocatalytic tandem,
- overlapping additional energy states with photocatalyst bands, which is conducive transfer of excited charge carriers to reactive sites on the surface of photocatalytic tandem (during their lifetime),
- preserve the position of the conduction band of the semiconducting oxides or location of this band so that maintain its photoreductive activity [32].

In last years, various attempts have been carried out by introduction of non-metals in the structure. Thus, carbon [33,34], nitrogen [35,36], sulphur [37], fluorine [38], iodine [39] and boron [40] were considered and successfully cause enhanced photocatalytic activity. Among these elements, nitrogen was thought as the most effective substitution doping non-metal due to a similar size to oxygen atom as well as low ionization energy. Consequently, the nitrogen can be easily introduced into semiconducting oxides lattice and substitute the oxygen leading to higher photocatalytic activity.

The TiO₂ has been doped also by metal ions as Ag [41,42], Pt [43], Fe [44], W [45], La [46,47], Ln [48], Au [49], Mo [50], Cu [51] as well as non-metals F [52], B/N [53] and Co [54,55] or inorganic compounds like Fe₂O₃ [56], SnO₂ [57]. Good improvements were demonstrated by dopants which contribute to separate the photogenerated electron-hole pairs resulting in increased recombination times and then an enhancement of photocatalytic activity for both, oxidation and reduction.

1.2.2. Role of the material morphology and nano-structuration in the photocatalytic efficiency

Suitable photocatalytic responses of the semiconducting materials depend on their surface available for the reactions, their morphology, size and crystalline structure. During a photocatalytic process, the suitable radiation induces the formation of electron-hole pairs ($h^+ + e^-$) with the electrons being transferred from the valence to the conduction band. The charges ($h^+ + e^-$) migrate to the surface of the compound and interact with the surrounding media (water, organic groups, small inorganic particles) to create reactive radicals as superoxide (O_2^- and OH^-). In such case the material with the highest interface with surrounding media is required. A promising strategy to contribute to high contact surface is based on the synthesis of meso- or nanoporous structures as well as nanostructured surfaces. A simple geometry model can be used roughly to underline the large difference between samples prepared as thin layers with an area of $0.1 \times 0.1 \mu m^2$ presenting nanostructured surface and the samples with smooth surface without any unevenness or convexity. For the nanostructured sample, its surface was treated as composed by hemispheric nanoislands with a radius about 5 nm distributed on the film. In the case the 100 pieces are distributed uniformly on the substrate (**Fig. 1.2.2.1**). The estimation of available surface can be as follows:

$$\text{Film surface: } P_s = 100 \cdot 100 = 10000 nm^2 ,$$

$$\text{Nanoisland surface : } P_m = \frac{1}{2} 4\pi r^2 = 2\pi r^2; P_m = 2 \cdot 3.14 \cdot 5^2 = 157 nm^2 ,$$

$$\text{Total surface of particles: } 100P_m = 15700 nm^2 ,$$

$$\text{Total nanostructured film surface : } P_{ns} = 17850 nm^2 .$$

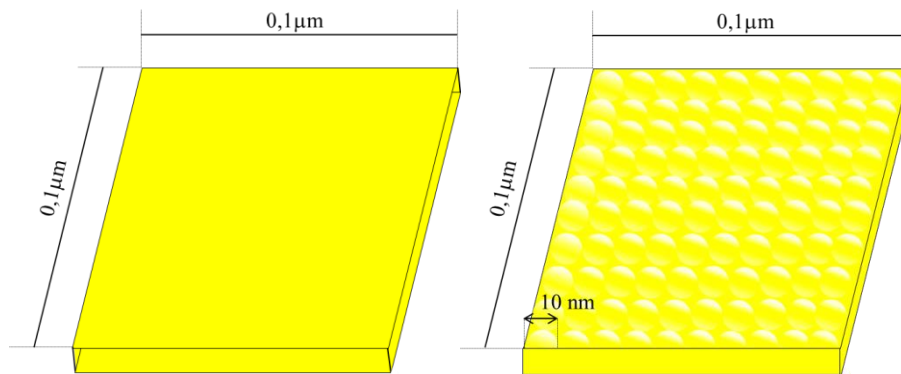


Figure 1.2.2.1. Smooth and porous surface

This simple model illustrates the difference of contact area between smooth and porous surface, which can be activated during a photocatalytic process. The calculations show that the nanostructured surface is more than 1,7 times larger than the smooth area. Similar calculations can be made on nanoporous films which were experimentally realized by Guisheng Li, et al. for bismuth vanadate samples [58]. The synthesis of the nanostructured BiVO₄ network is based on a hydrothermal method using a template from mesoporous silica (KIT-6). Based on the experimental investigations, the photoefficiency of the mesoporous material increased more than by 80 % compared to conventional bulk BiVO₄ [58]. Beyond the above aspects, the shape of the particles has shown a significant impact on their photocatalytic activity. This was demonstrated by using nanoparticles synthesized following different chemical procedures. Thus, several shapes were obtained as flowers [59], stars [60], butterfly wings [61] or peanuts [62] and many others. The carried out experiments have shown a strong correlation between the nanoparticle shape with a high contact surface and the efficiency of the photocatalytic process.

Semiconducting nanostructures as 0D, 1D, 2D and 3D-dimensional objects were currently synthesised with stable morphologies and sizes [63-67]. For the particular case of the 2D systems formed as thin films, they can be deposited on several substrates as single or multilayers structures with the thickness from nano- to micrometer scale [68-71]. The thickness and the nature of the substrates play crucial role in the efficiency of the photocatalytic processes. From one hand, this is understood from the light penetration in the sample and then from photogeneration more or less density of electron-hole pairs in the film. On the other hand, the nature of the substrate favour the formation of interfaces with more or less defects or dislocations which may overcome the transport of the photogenerated charge carriers at the surface of the film. When the synthesis of the film can be realized by chemical routes as sol-gel method, the possibility to increase the contact surface of the film can be realized thanks to surfactants. The obtained films exhibit mesoporous organisation with the pores surfaces controlled by the synthesis conditions and the features of the surfactants [72,73]. The contact surfaces of such structures are enough high to favour enhanced efficiencies of the photocatalytic process.

It is worth noting that the nanostructures peculiarities show drastic changes on their physical properties due to the size quantum confinement effects. This occurs when at least one dimension of the system became lower than a defined critical length l_c leading to modification of the electronic, optical and vibrational properties compared to those in the bulk system. The l_c depends on the physical properties of the material and differs from a semiconducting, metallic or magnetic structure. In semiconductors, the Bohr radius of the bounded state of electron-hole pair defines the l_c and below such length, the band gap is affected by the size quantum confinement effect [74] leading to a gradual increase with decreasing the size as it is illustrated for the TiO_2 (**Fig. 1.2.2.2.**).

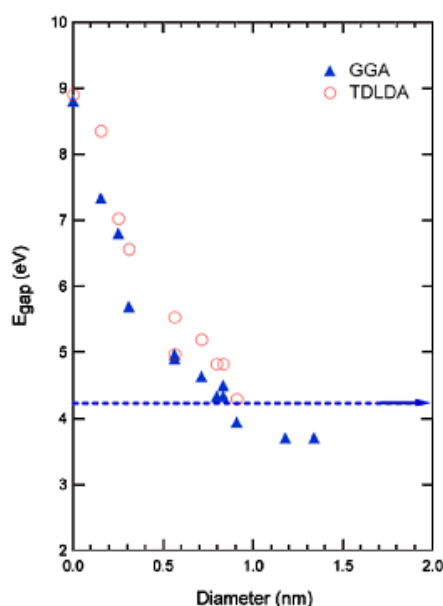


Figure 1.2.2.2. The HOMO–LUMO energy gap splitting vs size calculated by the density functional theory methods as GGA and TDLDA for unpassivated $(\text{TiO}_2)_n$ anatase structures [74]

1.2.3. Physical features of bismuth vanadate (BiVO_4)

Bismuth vanadate is a yellow solid compound with regard to its band gap in the visible light possessing the features to be non-toxic and chemically stable in several solvents including water. After being investigated for its ferroelastic phase transition three decade earlier, the interest was reactivated in a recent period as visible light driven photocatalyst offering good alternative to the UV-photoactive TiO_2 . The BiVO_4 exhibits three crystalline polymorphs such as tetragonal-scheelite (t - s), monoclinic scheelite (m - s), and zircon-type (z - t) structure (**Fig. 1.2.3.1.**) [75]. However, the most commonly used structure for photocatalytic applications consist in the m - s phase [76].

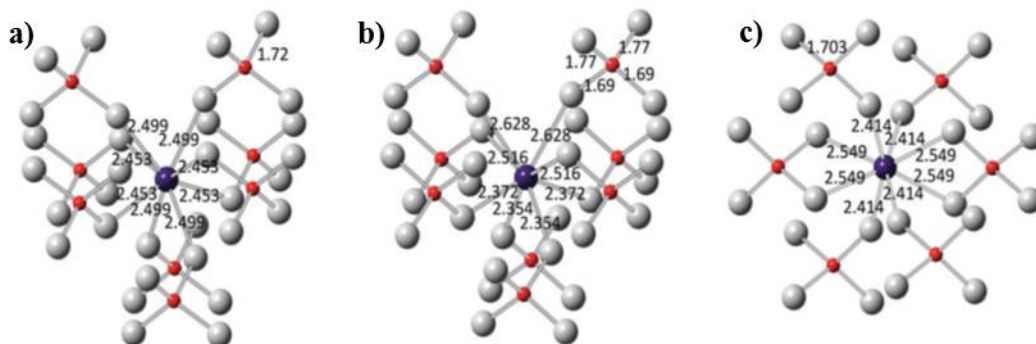


Figure 1.2.3.1. Local coordination of V and Bi ions in (a) tetragonal scheelite (*t-s*), (b) monoclinic scheelite (*m-s*), (c) and zircon-type (*z-t*) of BiVO_4 structure. The bond lengths are demonstrated in Å (red: V, purple: Bi, and gray: O atoms) [75]

Depending on the thermal treatment, bismuth vanadate can transform from one crystalline phase to another. The transition from the tetragonal-type to monoclinic structure occurs at room temperature with reversible features at 255°C . Heating the sample in the range $400\text{--}500^\circ\text{C}$ causes an irreversible transition from zircon to monoclinic BiVO_4 structure [77,78]. From structural side, *m-s* polymorph of bismuth vanadate crystallizes in the space group C_{2h}^6 with the point group $C2/c$. It is composed by vanadium ions surrounded by four oxygen ions. The BiO_8 groups have some oxygen ions sheared with VO_4 tetrahedron vertices and BiO_8 dodecahedron (**Fig. 1.2.3.2.**). Therefore, the oxygen ions can be divided into two groups O_1 and O_2 . The O_1 represents oxygen ions participating to the coordination of one Bi and one V ion. The O_2 represents the oxygen ions involved in the coordination with two Bi ions and one V ion.

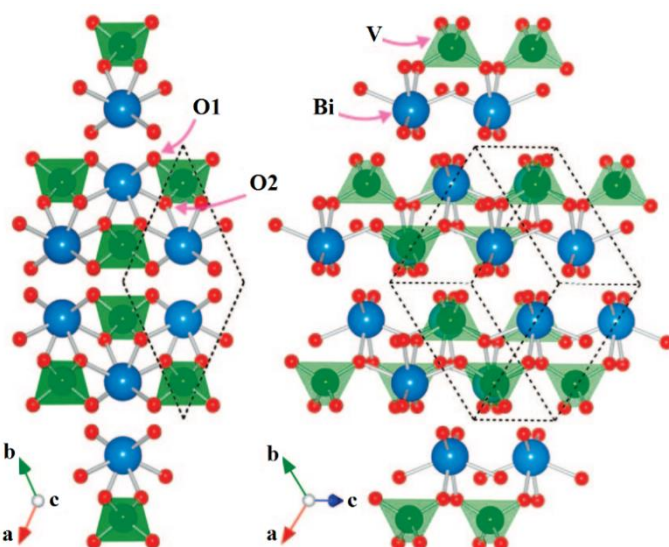


Figure 1.2.3.2. Representation of the of BiVO_4 crystal structure (blue: Bi, red: O, green: V). The base centered monoclinic primitive cell is indicated by the dashed black lines [79]

The BiVO_4 crystal has semiconducting properties. The top of the valence band in monoclinic BiVO_4 is built by hybridization of the Bi 6s and the O 2p atomic orbitals. Generally, a significant contribution of the oxygen orbitals occurs in the valence band of the semiconducting structure. The bottom of the conduction band has the largest contribution from the d orbitals of vanadium ions (**Fig. 1.2.3.3.**) [80].

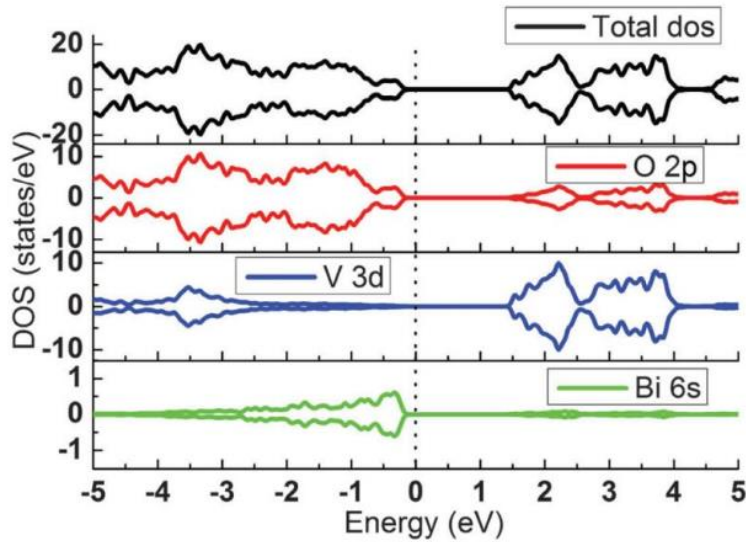


Figure 1.2.3.3. Partial density of states (PDOS) for the monoclinic BiVO_4 crystal form [80]

The electronic properties of the BiVO_4 were studied also theoretically using the DFT methodology [81]. By this approach, Zhao and co-authors confirmed the hybridization between the Bi 6s and the O 2p orbitals at the top of the VB and proved that they are responsible for the band gap of the monoclinic BiVO_4 , while the CB is composed mainly by the V 3d orbitals with almost negligible influence of the O 2p and the Bi 6p orbitals. These authors point out the indirect band gap nature of the BiVO_4 , with an energy gap equal to 2.17 eV (**Fig. 1.2.3.4.**).

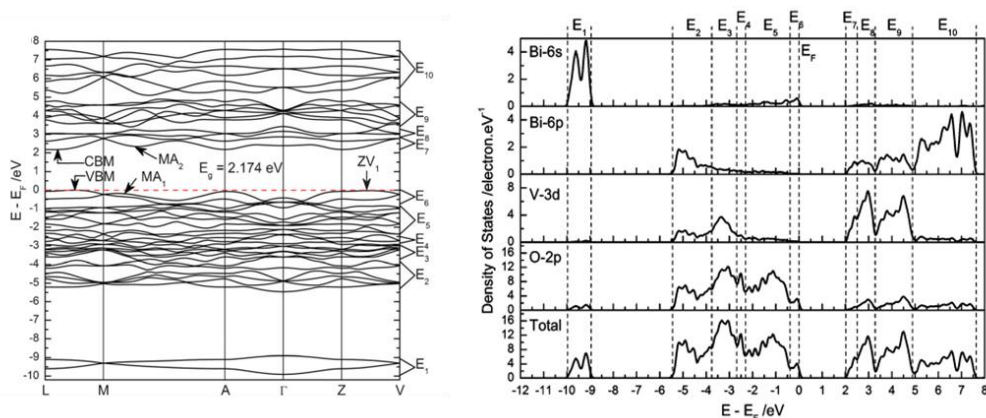


Figure 1.2.3.4. The calculated energy band structure (**left**) and PDOS (**right**) of monoclinic BiVO_4 [82]

Zhao and co-authors calculated also the partial electronic density of states for *m-s* BiVO₄. It can be seen that the top of the VB mainly compounds by two non-bonded states as the Bi 6s and O 2p_π. The bottom of conduction band is composed by V d_{3x²-y²} (or d_{3z²}) states, without the involvement of oxygen orbitals. The electron transfer between VB and CB occurs between the hybrid orbitals of O/Bi and the d orbitals of V ions. Furthermore, the spatial distance between Bi and V atoms is about 3.61–3.85 Å and then, the probability is quite low for electron transitions from the occupied Bi 6s states to the unoccupied V 3d states. Reduction of the distance between VB and CB is caused by O 2p state. Moreover, Zhao et al. found that the effective mass of an photogenerated electrons on the bottom of the CB is equal to 0.9 m_e, while the mass of holes on the top of the VB is equal to 0.7 m_e. However in work of Walsh and co-authors the effective masses of the generated electrons and holes are equivalent and equal to 0.3 m_e [82,83]. This can mean that the mobility of electrons and holes in BiVO₄ is expected to be similar for both charge carriers and it may have good contribution to the photocatalytic properties of the mentioned material.

As mentioned earlier, the monoclinic BiVO₄ has been considered as one of the most active visible-light photocatalyst regarding its low band gap. For the electronic properties, the hybridization of the Bi 6s and O 2p orbitals causes an increase of the top of VB and then a reduction of the band gap of the monoclinic BiVO₄. For semiconducting photocatalysts different attempts have been made in order to improve their electronic and optical properties and particularly to enhance their light absorption in the visible spectral range.

Kudo et al. demonstrated that by mixing of parental reactants followed by calcination process it is possible to obtain material with band gap equal to 2,4 eV contrary to the BiVO₄ in tetragonal phase where the energy gap is equal to 2.9 eV [84].

One of the most common estimation method to determinate the value of the band gap is the Kubelka–Munk (K-M) function $F(R)$ which use the reflectance R value of a sample in order to approximate the optical absorbance of a semiconductor:

$$F(R) = \frac{(1-R)^n}{2R} . \quad (1.2.3.1.)$$

After this manipulation a Tauc Plot can be constructed with:

$$\alpha h\nu = A(h\nu - E_g)^n , \quad (1.2.3.2.)$$

where α is the absorption coefficient of the material, the $h\nu$ is the energy of light, $n = 1/2$ is used to determine the energy gap for a direct band gap materials and

$n=2$ for indirect semiconductors [85]. For the thin films of the BiVO_4 annealed with different temperatures, the extrapolation of the curve to the $h\nu$ axis gives the semiconductor band gap (**Fig. 1.2.3.5.**). The value of the band gap decreases from 2.53 to 2.47 eV as annealing temperature increases from 400°C to 600°C, respectively [86]. Similar dependency was examined by Zhang et al. for mixture of the t-s with m-s phase of the BiVO_4 in the powder form. Attention was focused on annealing temperatures as 140, 160, 180 and 200°C which gave rise to band gap equal to 2.52, 2.51, 2.41 and 2.34 eV, respectively [87]. Experimental investigations proved that value of the energy gap depends on the processing temperature which control the involved crystalline phases.

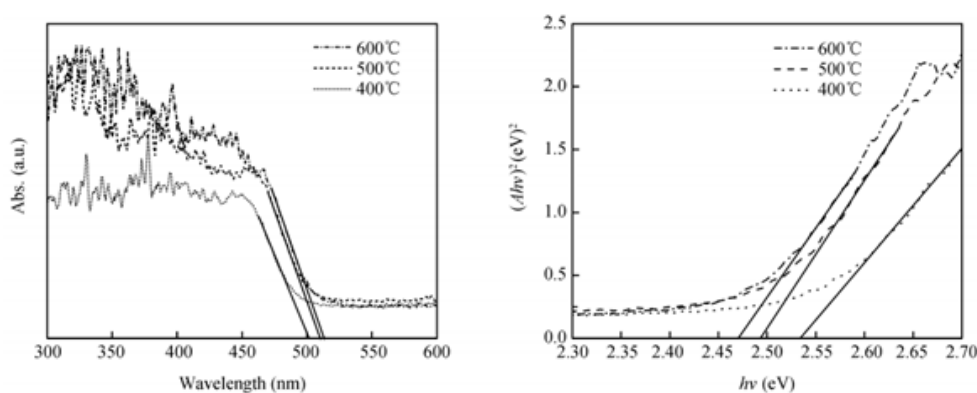


Figure 1.2.3.5. UV-Vis absorption spectra of the BiVO_4 thin films annealed at 400, 500 and 600°C with a ramping rate of 3°C/min (**left**) and the calculated band gap extrapolation according to UV-Vis absorption spectra and Kubelka-Munk function (**right**) [85]

1.2.4. Synthesis methods of the BiVO_4 and related samples morphologies

Depending on the considered method, the morphology and structural properties of the synthesized material can be modulated in large extent. The objective of this chapter section is to highlight the main features of the synthesis methods to obtain BiVO_4 with defined structural organization.

Based on the synthesis methods, it has been shown the close correlation between the morphology, the structural order of the samples and the modulation of their electronic behavior. In heterogeneous photocatalysis, the reaction rate constants are highly dependent on the contact surfaces. Therefore, in the final network, the relevant synthesis methods must enhance the accessible surfaces as mesoporous organization, nanoparticles, nanoislands involved in the most external part of the thin films.

Beyond the numerous synthesis methods [88,89], only few experiments lead to the required features of the BiVO₄ showing satisfactory photocatalytic properties. Based on experimental investigations of Fan and co-authors [90] was exhibited that the best photocatalytic efficiencies were confirmed for pure tetragonal or monoclinic phase of the BiVO₄ (70%) compared to the non-pure polymorphs. According to the theoretical predictions [90] related to nanosized media, the main difference between the phases concerns the hybridization of Bi 6s and O 2p orbital in the bottom of VB of the monoclinic form which cause the photocatalytic properties of the BiVO₄. For monoclinic phase, the hybridization narrows the value of the energy gap and thus stimulates more efficient photogeneration of the ($h^+ + e^-$) pairs. Consequently, more active radicals are formed in heterogeneous photocatalysis and then efficient decomposition occurs for organic molecules in water solution [90].

In the report of Zhang [91] related to the synthesis methods, the pH effect on structural, optical and photocatalytic properties was investigated. It has been shown that as the concentration of hydrogen ions in the solution increases, the synthesized particle size also increases. Therefore, the diethylene glycol was used as a solvent to maintain the appropriate pH of the final solution. With the increase in pH the size of the BiVO₄ particles increased, and at pH = 8 the stoichiometry of the compound was changed. As a consequence, the photoactivity of the samples has also changed. It has been confirmed that the photocatalytic activity decreases with the increase in particle size what can be caused by the increase in the solution pH at the final stage of the synthesis process [91]. Chen and co-authors have demonstrated that a higher concentration of the CH₃COOH results in smaller BiVO₄ particles with better photocatalytic properties than the bulk material [92]. Smaller particle sizes can reduce the length of migration of the photogenerated charge carriers and further reduce the rate of electrons-holes pairs recombination. The rough and relatively high specific surface provide more active sites, which is advantageous for catalytic reactions.

Sol-gel and hydrothermal synthesis are the most commonly used methods to produce nano- to micrometer sized materials with different particle morphologies. **Fig. 1.2.4.1.** illustrates the diversity of the BiVO₄ particle forms synthesized by the sol-gel method. Irrespective to the used solvents such as 2-propanol + ethanol or water + nitric acid, **Fig. 1.2.4.1.a.** and **Fig. 1.2.4.1.c.**, the used synthesis sol-gel pathway lead to the same shape of the BiVO₄ particles.

The size of a particles presented in **Fig. 1.2.4.1a.** is in the range 200 to 400 nm, whereas the sample illustrated in **Fig. 1.2.4.1.c.** has the size between 300 and 500 nm. In both cases, a tendency to agglomeration has been observed [93,94]. Pookmanee et al. performed the experimental procedure for preparing BiVO_4 powder by the sol-gel method. The obtained material had an irregular shape with an agglomeration tendency. SEM studies have shown that the particle size varies from 0.3 - 0.5 μm up to 0.7-1.0 μm with the temperature increase for 400°C up to 600°C, respectively [94]. It has been also shown that the acetic acid added in the synthesis process can have a significant effect on the size of the crystals.

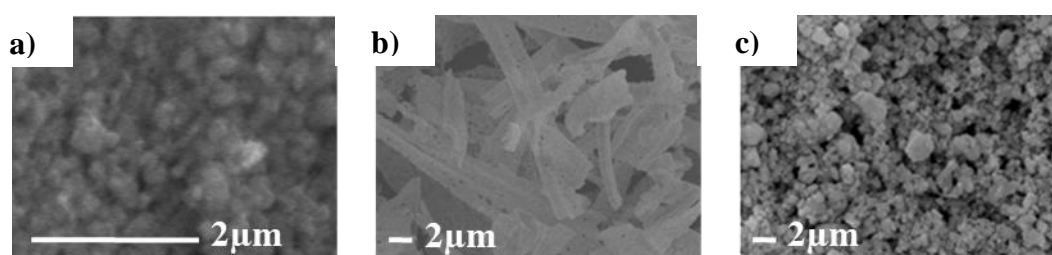


Figure 1.2.4.1. SEM images of BiVO_4 prepared by the sol-gel method calcinated at a) 400°C [93]
b) 450°C [95] c) 400°C [94]

Fig. 1.2.4.2.b. shows the shape of particles formed by the polyvinyl pyrrolidone (PVP) and anhydrous ethanol supplementation in the hydrothermal process. The resulting ribbon-like structure with the width of about 3 μm , and the length about 10-50 microns in length and thickness of about 0.4 μm simultaneously demonstrates the effect of the polymer precursor on the structure of the obtained material [95].

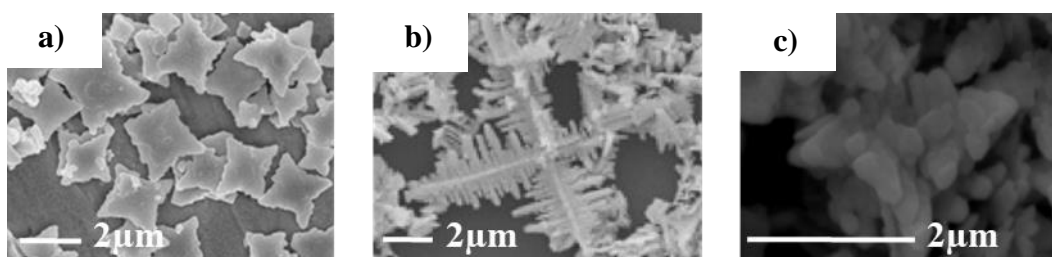


Figure 1.2.4.2. SEM images of the BiVO_4 prepared by the hydrothermal method. Autoclave was heated at a) 120°C, 6h [96] b) 120°C, 12h [97] c) 160°C, 24h [98]

The use of hydrothermal pathways for the BiVO_4 synthesis allows greater manipulation of its form compared to the sol-gel reaction. Sun et al. modify the reaction mixture by adding a chelating complex such as Ethylene Diamine Tetra Acetic acid (EDTA).

As illustrated in (Fig. 1.2.4.2.a.), the product consists in quasi-quadratic star-like morphology built from smaller nanoplates and possessing a length of about 1-2 μm and thickness of about 100 nm [96]. Controlling the pH of the reaction mixture one can also modify the morphology of the particles. Modifying the pH by changing the amount of NaOH leads to BiVO_4 with dendrimers form [97]. The obtained material for pH=6 had the length of the trunks equal to 4 – 6 μm ; while the length of the branches ranges is from 400 nm to 1 μm (Fig. 1.2.4.2.b.) [97]. At a similar value of pH=7, Hojamberdiev et al. obtained samples of the BiVO_4 microstructures from flower-like to star-like with the microstructures composed by nanoplates. A key parameter in the synthesis was also related to use of the ethylene glycol (EG) and ethylenediamine (EDA) to fine-tune the pH of the reaction mixture (Fig. 1.2.4.2.c.) [98] toward the achievement of defined sample sizes and morphologies.

The best photocatalytic efficiency is obtained for nano- or mesoporous samples as it was confirmed experimentally [99-101]. To achieve the intended structure, a synthesis approach using a organic precursor or porous silica was used. For this purpose, the structures such as surfactants Poly(ethylene glycol)-block-poly(propylene glycol)-block-poly(ethylene glycol) (P123) [102], porous silica as SBA-15, KIT-5 [103], KIT-6 [58] or polymers [104-107] were used to obtain BiVO_4 batches with high surface area (Fig. 1.2.4.3.). In this case more organic dye molecules can be adsorbed on the surface of the photocatalyst.

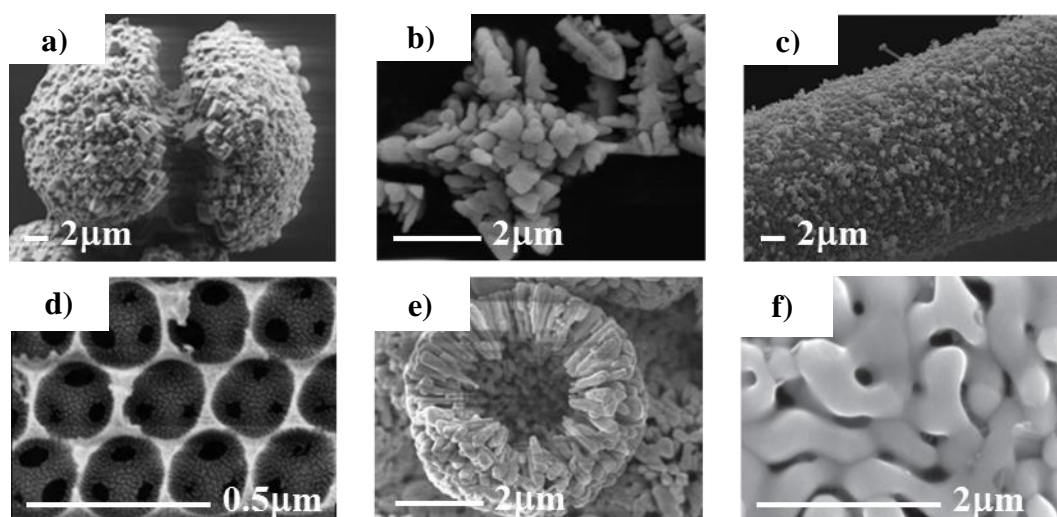


Figure 1.2.4.3. SEM images of porous BiVO_4 synthesized with surfactant a) DMMP [108] b) P123 [102] porous silica template c) silica fiber immobilized-CNFs [109] polymer d) colloidal PS spheres [107] e) PVA [110] f) PS balls [111]

The nanostructures exhibited in **Fig. 1.2.4.3.**, despite the apparent differences in their morphology, show similar photocatalytic properties. Irrespective to the surfactant nature, when the silicon precursor or the polymers were used for the synthesis, the obtained structures show higher available surface. For the material synthesized by using surfactants, porous structures were obtained with agglomerated large clusters such as dumbbell-shaped spheroids, stars and fiber morphologies. Each one from these samples consists in smaller BiVO_4 particles as nanocubes, nanoplates or nanotubes [108,102,109]. It has also been demonstrated that the use of the same chemical compound, like a PS, changes the reaction parameters leading to different morphologies of the obtained compounds (**Fig. 1.2.4.3.d.** and **Fig. 1.2.4.3.f.**) [107,111].

1.2.5. Photocatalytic properties of the bulk and thin film BiVO_4 systems

The photoactivity of semiconducting oxides as bismuth vanadate was investigated intensively in the last decade. Their vast majority focused on the phase composition of the BiVO_4 . Frequently, the photocatalytic properties of the BiVO_4 were defined in relation to the TiO_2 in anatase crystal forms because the second one is very popular semiconducting oxide used in photocatalysis and photovoltaics processes. Its main drawback, it has a significant limitation in absorption of radiation in the visible range ($E_g = 3,2$ eV). The monoclinic BiVO_4 is capable to absorb of visible light due to its lower energy gap ($E_g = 2,4$ eV). Kohtani and co-authors performed a comparison of photoactive properties between the TiO_2 in anatase form to the monoclinic BiVO_4 [112]. The impact of the shape and size of particles was also considered as a key factor in the efficiency of a photocatalytic responses. In the same context, commercial TiO_2 (Degussa P25) and synthesized monoclinic BiVO_4 were considered for the photodegradation of the (*n*-4-nonylphenol) compound. Despite significant differences in the size of the active area, the photodegradation of nanostructures in the solution after 60 minutes was practically identical for both samples [140]. At the next stage of the study, investigations were devoted to the photoactivity of monoclinic scheelite bismuth vanadate (*m*- BiVO_4) and tetragonal (*t*- BiVO_4) structures. The authors [140] carried out a study on photocatalytic properties through the evolution of the O_2 from the AgNO_3 solution using the monoclinic and tetragonal form of the BiVO_4 . The study was conducted for two different electromagnetic radiation wavelength, in which the samples were exposed.

Based on the time dependent changes of the O₂ production, monoclinic form has shown a much more effective photoactivity whatever the excitation radiation in the visible or in the UV range (**Fig. 1.2.5.1**).

The differences in the photocatalytic production of oxygen are caused by the distortion of the Bi-O polyhedron in the monoclinic form of the BiVO₄. The *m*-BiVO₄ form has four different Bi-O lengths (2.354 Å, 2.372 Å, 2.516 Å, 2.628 Å) while the *t*-BiVO₄ forms only two ones (2.453 Å, 2.499 Å), which means that it has a more symmetrical structure. The major difference between *m*-BiVO₄ and *t*-BiVO₄ is the distortion of the Bi-O polyhedron by 6s² lone pairs of Bi³⁺. Therefore, it was concluded that the mentioned distortion dominantly affects the photocatalytic properties of the BiVO₄ probably through the charge separation and delocalization of photogenerated electrons and holes. A similar approach was shown by Yu and Kudo [47] who compared the photocatalytic evolution of O₂ from the AgNO₃ solution using radiation less than 420 nm. The samples were synthesized at different pH values of the primary solution without (*h*-BiVO₄, pH less than 1) and with an ammonia (pH = 1, 4, 9) as well as with organic urea precursor (*u*-BiVO₄). It has been shown that the highest degree of O₂ photoevolution from the solution shows samples synthesized using urea and pH = 1, while the lowest efficiency was observed for the sample synthesized with pH = 9. The most significant influence on photocatalytic properties has the distortion occurring in *u*-BiVO₄ and *h*-BiVO₄ determined by analysing the vibrational properties of the discussed materials [113].

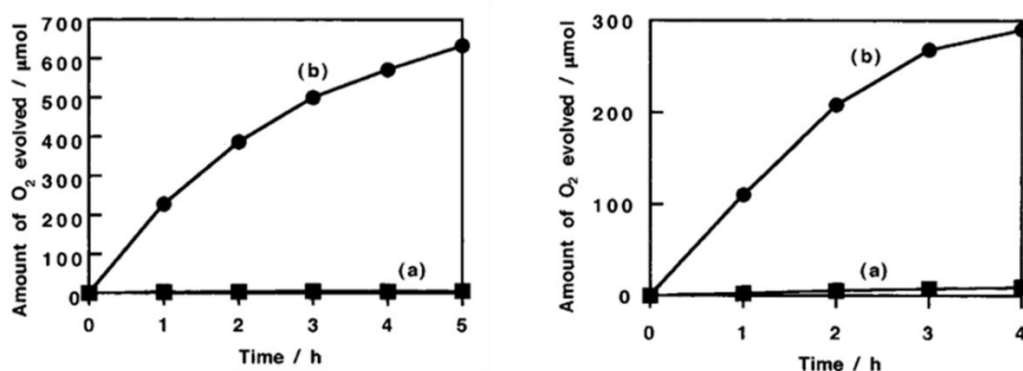

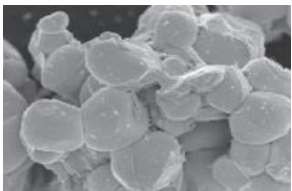
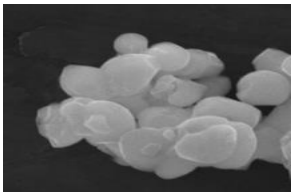


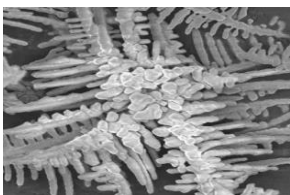
Figure 1.2.5.1. Photocatalytic evolution of the O₂ from aqueous AgNO₃ solutions (0.05 mol/L, 320 mL) under visible light irradiation (λ > 420 nm) (**left**) and under ultraviolet light irradiation (300 < λ < 380 nm) (**right**) on (a) tetragonal BiVO₄ and (b) monoclinic BiVO₄ structure [114]

The influence of structure at the material properties is also of great importance. The **Table 1.2.5.1.** underlines the impact of shapes and size of the BiVO₄ on photocatalytic properties expressed by their efficiency. In addition, morphologies with increased active surface such as dendrites, microtubes or mesoporous structures have satisfactory photocatalytic property greater than 80 % irrespective to the dye used in the photocatalytic test. Achieving high photocatalytic yields for the bulk BiVO₄ material has opened the way for improving the photocatalytic processes through the increase in their characteristic parameter which is the reaction constant rates.

The development of thin films and nanostructures attracts a great interest to the BiVO₄ based materials. These systems were mainly analyzed for their electrochemical properties to create the most efficient photoactivity [115-117]. Nevertheless, the O₂ photoevolution analysis has confirmed satisfying photocatalytic properties of the BiVO₄ in thin film form with nanoparticle size equal to 200-400 nm as well as to 20-40 nm [93,118]. Zhou and co-workers obtained similar results in the photodegradation process of 2,4-dichlorophenol by the BiVO₄ thin films under visible radiations ($\lambda > 420$ nm) [86].

Table 1.2.5.1. Summary of several monoclinic BiVO₄ samples synthesized by different routes relative to the photocatalytic efficiency

Samples morphology	Kind of organic dye molecules and concentration in solution [mmol/L]	Time of irradiation [min.]	The wavelength of the used radiation [nm]	Photocatalytic efficiency [%]	Ref.
 Spherical-shaped particles with diameters in a range from 10 to 40 nm	Methylene Blue (MB) [0,03]	150	$\lambda > 400$ nm	up to about 70	[90]
 Crystallites size more than 100 nm	Methylene Blue (MB) [0,04]	240	$\lambda > 420$ nm	96,7	[119]
 Spherical-shaped particles with diameters in a range from 200 to 300 nm	Methylene Blue (MB) [2]	180	320–800 nm	76	[120]



Dendrites of size from 500 nm to 10 μ m

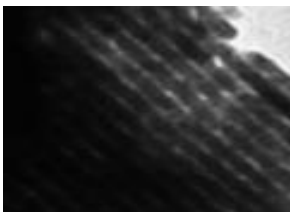
Methylene Blue (**MB**)
[0,06]

180

$\lambda > 420$ nm

More than 90

[87]



Mesoporous structure with single crystals
 $\sim 7,5$ nm

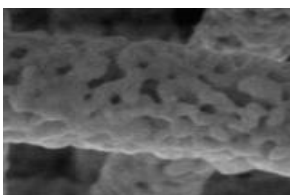
Methylene Blue (**MB**)
[0,12]

180

$\lambda > 400$ nm

About 85

[58]



Mesoporous nanofibers with diameter ~ 300 nm,
numerous pores (diameter ~ 20 nm)

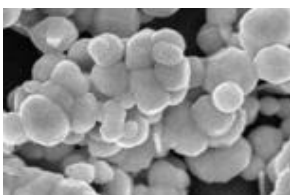
Rhodamine B (**RhB**)
[0,03]

180

$\lambda > 420$ nm

87.1

[121]



Spherical-shaped particles with size in a
range from 400 to 700 nm

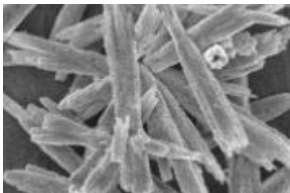
Rhodamine B (**RhB**)
[0,01]

20

$\lambda > 420$ nm

More than
90

[122]



Microtubes length of 2-5 μm ,
and a wall thickness of ~ 100 nm

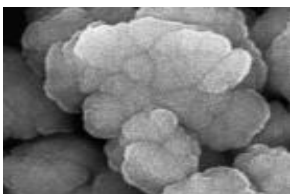
Rhodamine B (**RhB**)
[0,01]

180

$\lambda > 400$ nm

96

[123]



Particles with the size ranging from 100
to 300 nm, particles are composed of
many primary crystals, which are
confirmed to be ~ 50 nm

Methyl orange (**MO**)
[0,12]

30

$\lambda > 400$ nm

up to 90

[124]



Flower-like structure with a diameter 1-2
 μm

Methyl orange (**MO**)
[0,03]

240

$\lambda > 420$ nm

64

[125]

1.3. Peculiarities of hybrid systems in photoactive processes

Hybrid systems based on semiconductor materials are divided into two groups:

1. The combination of two inorganic materials forming photocatalytic tandem [126,127];
2. The combination of inorganic material with graphene [128,129], nanotubes [130] or an organic component such as organic dyes [131-133] and polymers [134] creating a composite system.

For hybrid systems, analyses of the charge transfer of donor- π -acceptor (D- π -A) dyes/photocatalyst systems were carried out [135,136]. In this case the main part of the hybrid system is composed by porous oxide formed as nanometric particles deposited on semiconducting and semitransparent substrates such as fluorine doped thin oxide (FTO). It is commonly used material as a substrate [137]. The used semiconductor oxides are titanium dioxide, zinc, vanadium or niobium oxides. On the surfaces of the semiconducting thin films organic dyes can be anchored. Their electronic features are chosen in such way that an effective absorption of visible solar radiation occurs and causes charge transfer from organic dye to the inorganic photoactive film. In the elaboration process of inorganic film sensitized by dyes, the organic molecules are permanently attached to the surface of the oxide layer by chemical bonding between the surface of the semiconducting oxide and dye through the carboxyl group [138,139]. The chemical compound exhibits color if it absorbs selectively visible electromagnetic radiation. The absorption of radiation from the visible part of the spectrum is generally due to the presence in the dye the chromophore group possessing conjugated π electrons. The presence of chromophore is essential, but the color of the compound becomes more intense only after the introduction into the molecule of electron donor group (auxochrome). Thus, suitable dyes for photoactive processes must be formed by couples of chromophore and auxochrome. In view of the chemical structure, dyes are divided into a number of classes, usually from the chromophore architecture. In this frame, azo, triarylmethane, anthraquinone, indigo, xanthene, phthalocyanine define classes of dyes.

The D- π -A structures used in such molecules should have the following requirement:

- Wide range of absorption of solar radiation;
- Presence of moieties such as -COOH, -H₂PO₃, -SO₃H allowing an effective bonding to the inorganic photoactive film surface;
- Excitation energy of the dye higher than the edge of the oxide conduction band allowing an efficient electron transfer process between the dye excited state and the CB of photocatalyst;
- Resistance to photodegradation as well as thermal and electrochemical stability.

Sensitizing photoactive materials with organic dyes were commonly synthesized using the D102 [140], D149 [133], N719 [141], Z907 [142] or black dye [143].

Creating the hybrid systems, the properties of the organic components must be correctly chosen with respect to those of the inorganic photoactive film. In particular, the HOMO orbitals should be located around the donor group of the molecule and the HOMO energy level should be above the VB of the photocatalyst. The LUMO orbitals should be located at the anchoring/acceptor group of the dye and should lie above the CB of semiconductor to facilitate the injection of electrons into the semiconductor to obtain photocatalyst-ligand charge transfer (**Fig. 1.3.1.**) [144]. Such requirements imply that the dye oxidation injects electrons into the conduction band of photocatalyst.

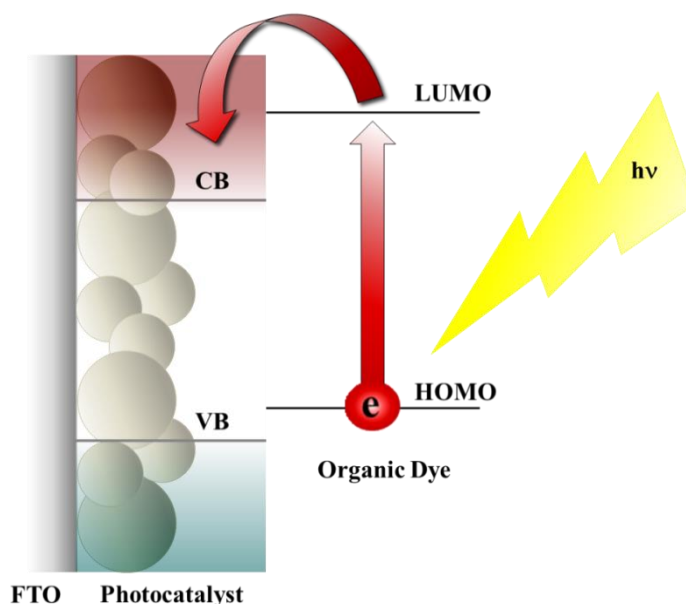


Figure 1.3.1. Schematic diagram for the charge transfer under radiation for the hybrid organic/inorganic system

The absorption characteristic of organic dye should be situated within the visible light range. In order to minimize the charge recombination between the injected electrons and the oxidized dye, the charge should be located around the dye donor part away from the photocatalyst surface. In addition, the donor group of the dye should be hydrophobic to avoid direct contact with any aqueous medium. This criterion contributes also to increase the long-term stability of the hybrid photoactive network [145].

The approach to anchor organic dye molecules to the surface of the TiO_2 was developed. This enables the absorption of the visible light by the organic groups and contributes to efficient photoinduced charge transfer to the inorganic surfaces improving the photoactivity of the whole hybrid composites. The organic molecules as dyes D149 [146], family of the merocyanine dyes [147] and carbon nanotube [148] were considered for titanium dioxide with the aim of increasing its photocatalytic efficiency. At the present time studies on the sensitization of the BiVO_4 by organic dyes for photocatalytic applications are not widely discussed. It will be the aim of the presented work.

1.4. Conclusions

Present chapter discusses the nature of the photocatalytic process and the applications of semiconducting materials, which are able to generate active electron-hole pairs under the radiation with different wavelengths. For this purpose, the properties of the two most commonly used photocatalysts: zinc oxide and titanium dioxide were presented. The electronic, structural, optical and photocatalytic properties of bismuth vanadate in bulk and thin film form were also discussed. At the same time an analysis was made concerning the key factors affecting the photocatalytic properties of the semiconducting oxides. On the basis of literature data, it can be concluded that:

- crystalline monoclinic BiVO_4 is the most commonly used for photoactivated processes,
- synthesis way allows to achieve the intended surface affecting the photocatalytic properties of material,
- annealing temperature and pH of the solution from which the BiVO_4 crystallize also affects the photocatalytic properties of the material.

The selection of reaction parameters allows to control the morphology of the tested material and thus to affect its properties. Additionally, by doping or sensitizing the photocatalyst, the absorption limits can be significantly increased by controlling the range of radiation in which the material will be active. These actions are aimed at obtaining a materials which can be activated by a visible radiation and act in the photocatalytic reactions.

1.5. References

- [1] A.V. Emeline, V.N. Kuznetsov, V.K. Ryabchuk, N. Serpone, New and Future Developments in Catalysis: Solar Photocatalysis, *Elsevier* 2013, 1-5
- [2] International Union of Pure and Applied Chemistry, Compendium of Chemical Terminology Gold Book, Version 2.3.3, 2014-02-24, 1106
- [3] J.-M. Herrmann, Heterogeneous photocatalysis: fundamentals and applications to the removal of various types of aqueous pollutants, *Catalysis Today* 1999, 53, 115–129
- [4] M.A. Fox, M.T. Dulay, Heterogeneous Photocatalysis, *Chem. Rev.* 1993, 93, 341-357
- [5] D. Bahnemann, Photocatalytic water treatment: solar energy applications, *Solar Energy* 2004, 77, 445–459
- [6] R. Andreozzi, V. Caprio, A. Insola, R. Marotta, Advanced oxidation processes (AOP) for water purification and recovery, *Catalysis Today* 1999, 53, 51–59
- [7] A. Mills, R.H. Davies, D. Worsley, Water Purification by Semiconductor Photocatalysism, *Chemical Society Reviews* 1993, 6, 417-425
- [8] M.N. Chong, B. Jin, C.W.K. Chow, C. Saint, Recent developments in photocatalytic water treatment technology: A review, *Water Research* 2010, 44, 2997-3027
- [9] I.P. Parkin, R.G. Palgrave, Self-cleaning coatings, *J. Mater. Chem.* 2005, 15, 1689–1695
- [10] M. Dolasia, Revolutionary Mexico City Hospital Facade Absorbs Toxins From The Environment, *DOGOnews*, 2013

- [11] J.-W. Seo, H. Chung, M.-Y Kim, J. Lee, I.-H. Choi, J. Cheon, Development of Water-Soluble SingleCrystalline TiO₂ Nanoparticles for Photocatalytic Cancer-Cell Treatment, *Small* 2007, 3, 5, 850 – 853
- [12] H.S. Qian, H.C. Guo, P. C.-L. Ho, R. Mahendran, Y. Zhang, Mesoporous-Silica-Coated Up-Conversion Fluorescent Nanoparticles for Photodynamic Therapy, *Small* 2009, 5, 20, 2285–2290
- [13] A.C.S. Samia, S. Dayal, C. Burda, Quantum Dot-based Energy Transfer: Perspectives and Potential for Applications in Photodynamic Therapy, *Photochemistry and Photobiology* 2006, 82, 617-625
- [14] K. Sunada, Y. Kikuchi, K. Hashimoto, A. Fujishima, Bactericidal and Detoxification Effects of TiO₂ Thin Film Photocatalysts, *Environ. Sci. Technol.* 1998, 32, 5, 726–728
- [15] H.N. Tsao, C. Yi, T. Moehl, J.-H. Yum, S. M. Zakeeruddin, M.K. Nazeeruddin, M. Grtzel, Cyclopentadithiophene Bridged Donor–Acceptor Dyes Achieve High Power Conversion Efficiencies in Dye-Sensitized Solar Cells Based on the trisCobalt Bipyridine Redox Couple, *ChemSusChem* 2011, 4, 591 – 594
- [16] S. Mori, M. Nagata, Y. Nakahata, K. Yasuta, R. Goto, M. Kimura, M. Taya, Enhancement of Incident Photon-to-Current Conversion Efficiency for Phthalocyanine-Sensitized Solar Cells by 3D Molecular Structuralization, *J. Am. Chem. Soc.* 2010, 132, 12, 4054–4055
- [17] P. Liska, K. R. Thampi, and M. Grätzel, D. Brémaud and D. Rudmann, H. M. Upadhyaya, A. N. Tiwari, Nanocrystalline dye-sensitized solar cell/copper indium gallium selenide thin-film tandem showing greater than 15% conversion efficiency, *Applied Physics Letters* 2006, 88, 203103
- [18] L. Honglin, L. Yingbo, L. Jinzhu, Y. Ke, First-principles study of p-type conductivity of N-Al/Ga/In co-doped ZnO, *Physica Scripta* 2015, 90, 25803-25810
- [19] D. O. Scanlon, C. W. Dunnill, J. Buckeridge, S. A. Shevlin, An. J. Logsdail, S. M. Woodley, C. R. A. Catlow, M. J. Powell, R. G. Palgrave, I. P. Parkin, G. W. Watson, T. W. Keal, P. Sherwood, A. Walsh, A. A. Sokol, Band alignment of rutile and anatase TiO₂, *Nature Materials* 2013, 12, 798–801

- [20] H.C. Wu, Y.C. Peng, T.-P. Shen, Electronic and Optical Properties of Substitutional and Interstitial Si-Doped ZnO, *Materials* 2012, 5, 2088-2100
- [21] S. Rehman, R. Ullah, A.M. Butt, N.D. Gohar, Strategies of making TiO₂ and ZnO visible light active, *Journal of Hazardous Materials* 2009, 170, 560–569
- [22] R. Ullah, J. Dutta, Photocatalytic degradation of organic dyes with manganese-doped ZnO nanoparticles, *Journal of Hazardous Materials* 2008, 156, 194–200
- [23] R. Wanga, J. H. Xin , Y. Yang , H. Liu , Liming Xu , J. Hu, The characteristics and photocatalytic activities of silver doped ZnO nanocrystallites, *Applied Surface Science* 2004, 227, 312–317
- [24] S. Anandan, A. Vinu, K.L.P. Sheeja Lovely, N. Gokulakrishnan, P. Srinivasu, T. Mori, V. Murugesan, V. Sivamurugan, K. Ariga, Photocatalytic activity of La-doped ZnO for the degradation of monocrotophos in aqueous suspension, *Journal of Molecular Catalysis A: Chemical* 2007, 266, 149–157
- [25] K.G. Kanade, B.B. Kale, J.O. Baeg, S.M. Lee, C.W. Lee, S.J. Moon, H. Chang, Self-assembled aligned Cu doped ZnO nanoparticles for photocatalytic hydrogen production under visible light irradiation, *Materials Chemistry and Physics* 2007, 102, 1, 98–104
- [26] X. Qiu, L. Li, J. Zheng, J. Liu, X. Sun, G. Li, Origin of the Enhanced Photocatalytic Activities of Semiconductors: A Case Study of ZnO Doped with Mg²⁺, *J. Phys. Chem. C* 2008, 112, 32, 2242–2248
- [27] C. Xu, L. Cao, G. Su, W. Liu, X. Qu, Y. Yu, Preparation, characterization and photocatalytic activity of Co-doped ZnO powders, *Journal of Alloys and Compounds* 2010, 497, 1–2, 373–376
- [28] S. Liu, C. Li, J. Yu, Q. Xiang, Improved visible-light photocatalytic activity of porous carbon self-doped ZnO nanosheet-assembled flowers, *CrystEngComm* 2011,13, 2533-2541
- [29] S. Kumar, A. Baruah, S. Tonda, B. Kumar, V. Shanker, B. Sreedhar, Cost-effective and eco-friendly synthesis of novel and stable N-doped ZnO/g-C₃N₄ core–shell nanoplates with excellent visible-light responsive photocatalysis, *Nanoscale* 2014, 6, 4830-4842

- [30] S. T. Ren, G. H. Fan, M. L. Liang, Q. Wang, G. L. Zhao, Electrodeposition of hierarchical ZnO/Cu₂O nanorod films for highly efficient visiblelight-driven photocatalytic applications, *Journal of Applied Physics* 2014, 115, 64301
- [31] Z. Zhang, P. Zhang, M. Zhang, Y. C. Liu, High Photocatalytic Activity of ZnO-Carbon Nanofiber Heteroarchitectures, *ACS Appl. Mater. Interfaces* 2011, 3, 590–596
- [32] R. Asahi, T. Morikawa, T. Ohwaki, K. Aoki, Y. Taga, Visible-light photocatalysis in nitrogen-doped titanium, *Science* 2001, 293, 269-271
- [33] Z.B. Wu, F. Dong, W.R. Zhao, H.Q. Wang, Y. Liu, B H. Guan, The fabrication and characterization of novel carbon doped TiO₂ nanotubes, nanowires and nanorods with high visible light photocatalytic activity, *Nanotechnology* 2009, 20, 23, 235701-235709
- [34] S. Sakthivel, H. Kisch, Daylight Photocatalysis by Carbon-Modified Titanium Dioxide, *Angew. Chem. Int. Ed* 2003, 42, 4908–4911
- [35] Y. Cong, J L. Zhang, F. Chen, M. Anpo, Synthesis and characterization of nitrogen-doped TiO₂ nanophotocatalyst with high visible light activity, *Journal of Physical Chemistry C*. 2007, 111,19, 6976-6982
- [36] H. Irie, Y. Watanabe, K. Hashimoto, Nitrogen-Concentration Dependence on Photocatalytic Activity of TiO_{2-x}N_x Powders, *J. Phys. Chem. B* 2003, 107, 23, 5483–5486
- [37] T. Umebayashi, T. Yamaki, S. Yamamoto, A. Miyashita, S. Tanaka, T. Sumita, K. Asai. Sulfur-doping of rutile-titanium dioxide by ion implantation: Photocurrent spectroscopy and first-principles band calculation studies, *Journal of Applied Physics* 2003, 93,9, 5156-5160
- [38] T. Yamaki, T. Sumita and S. Yamamoto, Formation of TiO_{2-x}F_x compounds in fluorine-implanted TiO₂, *Journal of Materials Science Letters*. 2002, 21, 1, 33-35
- [39] X.T. Hong, Z.P. Wang, W.M. Cai, F. Lu, J. Zhang, Y.Z. Yang, N. Ma, Y.J. Liu. Visible-light-activated nanoparticle photocatalyst of iodine-doped titanium dioxide, *Chem. Mater.* 2005, 17, 6, 1548-1552
- [40] A. Zaleska, J W. Sobczak, E. Grabowska, J. Hupka, Preparation and photocatalytic activity of boron-modified TiO₂ under UV and visible light, *Applied catalysis B-environmental* 2008, 78, 1-2, 92-100

- [41] Y. Zheng, L. Zheng, Y. Zhan, X. Lin, Q. Zheng, K. Wei, Ag/ZnO Heterostructure Nanocrystals: Synthesis, Characterization, and Photocatalysis, *Inorg. Chem.* 2007, 46, 17, 6980–6986
- [42] B. Xin, L. Jing, Z. Ren, B. Wang, H. Fu, Effects of Simultaneously Doped and Deposited Ag on the Photocatalytic Activity and Surface States of TiO₂, *J. Phys. Chem. B* 2005, 109, 7, 2805–2809
- [43] M. Qamar, Photodegradation of acridine orange catalyzed by nanostructured titanium dioxide modified with platinum and silver metals, *Desalination* 2010, 254, 1-3, 108-113
- [44] H.K. Shon, D.L. Cho, S.H. Na, J.B. Kim, H.J. Park, J.H. Kim, Development of a novel method to prepare Fe and Al-doped TiO₂ from wastewater, *Journal of industrial and Engineering Chemistry* 2009, 15, 4, 476-482
- [45] S.A.K. Leghari, S. Sajjad, F. Chen, J.L. Zhang, WO₃/TiO₂ composite with morphology change via hydrothermal template-free route as an efficient visible light photocatalyst, *Chemistry Engineering Journal* 2010, 166, 3, 906-915
- [46] F.B. Li, X.Z. Li, M.F. Hou, Photocatalytic degradation of 2-mercaptobenzothiazole in aqueous La³⁺-TiO₂ suspension for odor control, *Applied Catalysis B-Environmental* 2004, 48, 3, 185-194
- [47] S. Anandan, A. Vinu, K.L.P. Sheeja, Lovely, N. Gokulakrishnan, P. Srinivasu, T. Mori, V. Murugesan, V. Sivamurugan, K. Ariga, Photocatalytic activity of La-doped ZnO for the degradation of monocrotophos in aqueous suspension, *Journal of Molecular Catalysis A: Chemical* 2007, 266, 1-2, 149-157
- [48] Y. Xie, C. Yuan, X. Li, Photosensitized and photocatalyzed degradation of azo dye using Lnⁿ⁺-TiO₂ sol in aqueous solution under visible light irradiation, *Materials Science and Engineering B-solid state materials for advanced technology* 2005, 117, 3, 325-333
- [49] H. Li, Z. Bian, J. Zhu, Y. Huo, H. Li, Y. Lu, Mesoporous Au/TiO₂ Nanocomposites with Enhanced Photocatalytic Activity, *J. Am. Chem. Soc.* 2007, 129, 15, 4538–4539
- [50] Y. Yang, X. Li, J. Chen, L. Wang, Effect of doping mode on the photocatalytic activities of Mo/TiO₂, *Journal of Photochemistry and Photobiology A: Chemistry* 2004, 163, 3, 517–522

- [51] M. Fu, Y. Li, S. Wu, P. Lu, J. Liu, F. Dong, Sol-gel preparation and enhanced photocatalytic performance of Cu-doped ZnO nanoparticles, *Applied Surface Science* 2011, 258, 1587–1591
- [52] J. C. Yu, Jianguo, Wingkei, Zitao, Effects of F- Doping on the Photocatalytic Activity and Microstructures of Nanocrystalline TiO₂ Powders, *Chem. Mater.* 2002, 14, 9, 3808–3816
- [53] S. In, A. Orlov, R. Berg, F. García, S. Pedrosa-Jimenez, M. S. Tikhov, D. S. Wright, R. M. Lambert, Effective Visible Light-Activated B-Doped and B,N-Codoped TiO₂ Photocatalysts, *J. Am. Chem. Soc.* 2007, 129, 45, 13790–13791
- [54] M. Iwasaki, M. Hara, H. Kawada, H. Tada, S. Ito, Cobalt Ion-Doped TiO₂ Photocatalyst Response to Visible Light, *Journal of Colloid and Interface Science* 2000, 224, 1, 1, 202-204
- [55] C. Xu, L. Cao, G. Su, W. Liu X. Qu, Y. Yu, Preparation, characterization and photocatalytic activity of Co-doped ZnO powders, *Journal of Alloys and Compounds* 2010, 497, 373-376
- [56] Y. Liu, L. Su, J. Wu, T. Fang, R. Cai, A. Wei, Preparation and photocatalytic activity of ZnO/Fe₂O₃ nanotube composites, *Materials Science and Engineering: B* 2015, 194, 9-13
- [57] L. Zheng, Y. Zheng, C. Chen, Y. Zhan, X. Lin, Q. Zheng, K. Wei, J. Zhu, Network Structured SnO₂/ZnO Heterojunction Nanocatalyst with High Photocatalytic Activity, *Inorg. Chem.* 2009, 48, 5, 1819–1825
- [58] G. Li, D. Zhang, J. C. Yu, Ordered Mesoporous BiVO₄ through Nanocasting: A Superior Visible Light-Driven Photocatalyst, *Chem. Mater.* 2008, 20, 3983–3992
- [59] X. Yu, J. Yu, B. Cheng, M. Jaroniec, Synthesis of Hierarchical Flower-like AlOOH and TiO₂/AlOOH Superstructures and their Enhanced Photocatalytic Properties, *J. Phys. Chem. C* 2009, 113, 40, 17527–17535
- [60] Y. Lv, C. Li, L. Guo, Q. Wang, R. Wang, H. Xu, S. Yang, X. AI, J. Zhang, Nanostructured stars of ZnO microcrystals with intense stimulated emission, *Appl. Phys. Lett.* 2005, 87, 163103 (1-3)

- [61] L. Ding, H. Zhou, S. Lou, J. Ding, D. Zhang, H. Zhu, T. Fan, Butterfly wing architecture assisted CdS/Au/TiO₂ Z-schema type photocatalytic water splitting, *International Journal of Hydrogen Energy* 2013, 38, 8244-8253
- [62] B. Cao, J. Peng, Y. Xu, Simulated Sunlight-Driven Degradation of Rhodamine B by Porous Peanut-Like TiO₂/BiVO₄ Composite, *J Clust Sci* 2013, 24, 771-786
- [63] L. Samuelson, C. Thelander, M.T. Bjork, M. Borgstrom, K. Deppert, K.A. Dick, A.E. Hansena, T. Martensson, N. Paneva, A.I. Persson, W. Seifert, N. Skold, M.W. Larsson, L.R. Wallenberg, Semiconductor nanowires for 0D and 1D physics and applications, *Physica E* 2004, 25, 313–318
- [64] M. Luo, K. Cheng, W. Weng, C. Song, P. Du, G. Shen, G. Xu, G. Han, Size- and density-controlled synthesis of TiO₂ nanodots on a substrate by phase-separation-induced self-assembly, *Nanotechnology* 2009, 20, 215605-215612
- [65] J. Wu, C. Yum, Aligned TiO₂ Nanorods and Nanowalls, *J. Phys. Chem. B* 2004, 108, 11, 3377–3379
- [66] J. Liu, H. Bai, Y. Wang, Z. Liu, X. Zhang, D.D. Sun, Self-assembling TiO₂ nanorods on large graphene oxide sheets at a two-phase interface and their antirecombination in photocatalytic applications, *Adv. Funct. Mater.* 2010, 20, 4175–4181
- [67] C. Pacholski, A. Kornowski, H. Weller, Self-Assembly of ZnO: From Nanodots to Nanorods, *Angew. Chem. Int. Ed.* 2002, 41, 7, 1188-1191
- [68] E.S. Shim, H.S. Kang, J.S. Kang, J.H. Kim, S.Y. Lee, Effect of the variation of film thickness on the structural and optical properties of ZnO thin films deposited on sapphire substrate using PLD, *Applied Surface Science* 2002, 186, 1–4, 474-476
- [69] X.L. Cheng, H. Zhao, L.H. Huo, S. Gao, J.G. Zhao, ZnO nanoparticulate thin film: preparation, characterization and gas-sensing property, *Sensors and Actuators B* 2004, 102, 248–252
- [70] N. Nobuaki, I. Tomokazu, H. Kazuhito, F. Akira, Preparation of Transparent TiO₂ Thin Film Photocatalyst and Its Photocatalytic Activity, *Chemistry Letters* 1995, 24, 9, 841-842

- [71] J.-G. Yu, H.-G. Yu, B. Cheng, X.-J. Zhao, J.C. Yu, W.-K. Ho, The Effect of Calcination Temperature on the Surface Microstructure and Photocatalytic Activity of TiO₂ Thin Films Prepared by Liquid Phase Deposition, *J. Phys. Chem. B* 2003, 107, 50, 13871–13879
- [72] H. Choi, Y.J. Kim, R.S. Varma, D.D. Dionysiou, Thermally Stable Nanocrystalline TiO₂ Photocatalysts Synthesized via Sol-Gel Methods Modified with Ionic Liquid and Surfactant Molecules, *Chem. Mater.* 2006, 18, 5377-5384
- [73] S. Zhan, D. Chen, X. Jiao, C. Tao, Long TiO₂ Hollow Fibers with Mesoporous Walls: Sol-Gel Combined Electrospun Fabrication and Photocatalytic Properties, *J. Phys. Chem. B* 2006, 110, 23, 11199–11204
- [74] J.-Y. Raty, G. Galli, C. Bostedt, T.W. van Buuren, L.J. Terminello, Quantum Confinement and Fullerene-like Surface Reconstructions in Nanodiamonds, *Phys. Rev. Lett.* 2003, 90, 37401(1-4)
- [75] Y. Park, K. J. McDonald, K.S. Choi, Progress in bismuth vanadate photoanodes for use in solar water oxidation, *Chem Soc Rev* 2013, 42, 6, 2321-2337
- [76] C. Martinez Suarez, S. Hernández, N. Russo, BiVO₄ as photocatalyst for solar fuels production through water splitting: A short review, *Applied Catalysis A: General* 2015, 504, 158–170
- [77] Y. Park, K. J. McDonald, K.S. Choi, Progress in bismuth vanadate photoanodes for use in solar water oxidation, *Chem Soc Rev* 2013, 42, 6, 2321-2337
- [78] G.P. Nagabhushana, A.H. Tavakoli, A. Navrotsky, Energetics of bismuth vanadate, *Journal of Solid State Chemistry* 2015, 225, 187-192
- [79] J. K. Cooper, S. Gul, F. M. Toma, L. Chen, P.A. Glans, J. Guo, J. W. Ager, J. Yano, I. D. Sharp, Electronic Structure of Monoclinic BiVO₄, *Chem. Mater.* 2014, 26, 5365-5373
- [80] T. Liu, X. Zhou, M. Dupuis, C. Li, The nature of photogenerated charge separation among different crystal facets of BiVO₄ studied by a density functional theory, *Phys. Chem. Chem. Phys.* 2015, 17, 23503-23510

- [81] K. Ding, B. Chen, Z. Fang, Y. Zhang, Density functional theory study on the electronic and optical properties of three crystalline phases of BiVO₄, *Theor Chem Acc* 2013, 132, 1352-1359
- [82] X. Zhao, Z. Li, Z. Zou, Electronic structure and optical properties of monoclinic clinobisvanite BiVO₄, *Phys. Chem. Chem. Phys.* 2011, 13, 4746-4753
- [83] A. Walsh, Y. Yan, M. N. Huda, M. M. Al-Jassim, S.H. Wei, Band Edge Electronic Structure of BiVO₄: Elucidating the Role of the Bi s and V d Orbitals, *Chem. Mater.* 2009, 21, 547-551
- [84] A. Kudo, K. Omori, H. Kato, A Novel Aqueous Process for Preparation of Crystal Form-Controlled and Highly Crystalline BiVO₄ Powder from Layered Vanadates at Room Temperature and Its Photocatalytic and Photophysical Properties, *J. Am. Chem. Soc.* 1999, 121, 49, 11459-11467
- [85] R. López, R. Gómez, Band-gap energy estimation from diffuse reflectance measurements on sol-gel and commercial TiO₂: a comparative study, *J Sol-Gel Sci Technol* 2012, 61, 1-7
- [86] B. Zhou, J. Qu, X. Zhao, H. Liu, Fabrication and photoelectrocatalytic properties of nanocrystalline monoclinic BiVO₄ thin-film electrode, *J. Environ. Sci.* 2011, 23, 151-159
- [87] X. Zhang, Z. Ai, F. Jia, L. Zhang, X. Fan, Z. Zou, Selective synthesis and visible-light photocatalytic activities of BiVO₄ with different crystalline phases, *Materials Chemistry and Physics* 2007, 103, 162-167
- [88] Z. Liu, Q. Lu, C. Wang, J. Liua, G. Liu, Preparation of bamboo-shaped BiVO₄ nanofibers by electrospinning method and the enhanced visible-light photocatalytic activity, *Journal of Alloys and Compounds* 2015, 651, 29-33
- [89] M. Gotić, S. Musić, M. Ivanda, M. Šoufek, S. Popović, Synthesis and characterisation of bismuth(III) vanadate, *Journal of Molecular Structure* 2005, 744-747, 535-540
- [90] H. Fan, T. Jiang, H. Li, D. Wang, L. Wang, J. Zhai, D. He, P. Wang, T. Xie, Effect of BiVO₄ Crystalline Phases on the Photoinduced Carriers Behavior and Photocatalytic Activity, *J. Phys. Chem. C* 2012, 116, 3, 2425-2430

- [91] Y. Zhanga, G. Lia, X. Yanga, H. Yanga, Z. Lua, R. Chen, Monoclinic BiVO₄ micro-/nanostructures: Microwave and ultrasonic wave combined synthesis and their visible-light photocatalytic activities, *Journal of Alloys and Compounds* 2013, 551, 544-550
- [92] L. Chen, J. Wang, D. Meng, Y. Xing, X. Tian, X. Yu, K. Xu, X. Wu, Effects of citric acid and urea on the structural and morphological characteristics of BiVO₄ synthesized by the sol–gel combustion method, *J Sol-Gel Sci Technol* 2015, 76, 562–571
- [93] H. Liu, R. Nakamura, Y. Nakato, Promoted Photo-oxidation Reactivity of Particulate BiVO₄ Photocatalyst Prepared by a Photoassisted Sol-gel Method, *J. Electrochem. Soc.* 2005, 152, 11, 856-861
- [94] P. Pookmanee, S. Kojinok, S. Phanichphant, Bismuth Vanadate (BiVO₄) Powder Prepared by the Sol-gel Method, *Journal of Metals, Materials and Minerals* 2012, 22, 2, 49-53
- [95] G. Liu, S. Liu, Q. Lu, H. Sun, F. Xu, G. Zhao, Synthesis of monoclinic BiVO₄ microribbons by sol–gel combined with electrospinning process and photocatalytic degradation performances, *J Sol-Gel Sci Technol* 2014, 70, 1, 24-32
- [96] S. Sun, W. Wang, L. Zhou, H. Xu, Efficient Methylene Blue Removal over hydrothermally Synthesized Starlike BiVO₄, *Ind. Eng. Chem. Res.* 2009, 48, 1735–1739
- [97] Y. Guo, X. Yang, F. Ma, K. Li, L. Xu, X. Yuan, Y. Guo, Additive-free controllable fabrication of bismuth vanadates and their photocatalytic activity toward dye degradation, *Applied Surface Science* 2010, 256, 2215–2222
- [98] M. Hojamberdiev, G. Zhu, Z. C. Kadirova, J. Han, J. Liang, J. Zhou, X. Wei, P. Liu, Morphology-controlled growth of BiVO₄ crystals by hydrothermal method assisted with ethylene glycol and ethylenediamine and their photocatalytic activity, *Materials Chemistry and Physics* 2015, 165, 188-195
- [99] S. Hernandez, G. Barbero, G. Saracco, A.L. Alexe-Ionescu, Considerations on Oxygen Bubble Formation and Evolution on BiVO₄ Porous Anodes Used in Water Splitting Photoelectrochemical Cells, *J. Phys. Chem. C* 2015, 119, 9916–9925

- [100] H. Jiang, H. Dai, X. Meng, K. Ji, L. Zhang, J. Deng, Porous olive-like BiVO₄: Alcoho-hydrothermal preparation and excellent visible-light-driven photocatalytic performance for the degradation of phenol, *Applied Catalysis B: Environmental* 2011, 105, 326–334
- [101] M. Ge, L. Liu, W. Chen, Z. Zhou, Sunlight-driven degradation of Rhodamine B by peanut-shaped porous BiVO₄ nanostructures in the H₂O₂-containing system, *CrystEngComm* 2012, 14, 1038-1044
- [102] H. Jiang, X. Meng, H. Dai, J. Deng, Y. Liu, L. Zhang, Z. Zhao, R. Zhang, High-performance porous spherical or octapod-like single-crystalline BiVO₄ photocatalysts for the removal of phenol and methylene blue under visible-light illumination, *Journal of Hazardous Materials* 2012, 217–218, 92–99
- [103] T. Tsoncheva, L. Ivanova, J. Rosenholm, M. Linden, Cobalt oxide species supported on SBA-15, KIT-5 and KIT-6 mesoporous silicas for ethyl acetate total oxidation, *Applied Catalysis B: Environmental* 2009, 89, 365–374
- [104] A. Martínez-de la Cruz, U.M. García-Pérez, S. Sepúlveda-Guzmán, Characterization of the visible-light-driven BiVO₄ photocatalyst synthesized via a polymer-assisted hydrothermal method, *Res Chem Intermed* 2013, 39, 881–894
- [105] U.M. García-Pérez, S. Sepúlveda-Guzmán, A. Martínez-de la Cruz, Nanostructured BiVO₄ photocatalysts synthesized via a polymer-assisted coprecipitation method and their photocatalytic properties under visible-light irradiation, *Solid State Sciences* 2012, 14, 293-298
- [106] Z. Wang, W. Luo, S. Yan, J. Feng, Z. Zhao, Y. Zhu, Z. Li, Z. Zou, BiVO₄ nano-leaves: Mild synthesis and improved photocatalytic activity for O₂ production under visible light irradiation, *CrystEngComm* 2011, 13, 2500–2504
- [107] M. Zhou, H.B. Wu, J. Bao, L. Liang, X.W. Lou, Yi Xie, Ordered Macroporous BiVO₄ Architectures with Controllable Dual, Porosity for Efficient Solar Water Splitting, *Angew. Chem. Int. Ed.* 2013, 52, 8579 –8583
- [108] D. Ressnig, R. Kontic, G.R. Patzke, Morphology control of BiVO₄ photocatalysts: pH optimization vs. self-organization, *Materials Chemistry and Physics* 2012, 135, 457-466

- [109] Q. Wu, P. Chen, L. Zhao, J. Wu, X. Qi, W. Yao, Photocatalytic behavior of BiVO₄ immobilized on silica fiber via a combined alcohol-thermal and carbon nanofibers template route, *Catalysis Communications* 2014, 49, 29–33
- [110] S. Sarkar, K.K. Chattopadhyay, Visible light photocatalysis and electron emission from porous hollow spherical BiVO₄ nanostructures synthesized by a novel route, *Physica E: Low-dimensional Systems and Nanostructures* 2014, 58, 52-58
- [111] L. Dong, X. Zhang, X. Dong, X. Zhang, C. Ma, H. Ma, M. Xue, F. Shi, Structuring porous “sponge-like” BiVO₄ film for efficient photocatalysis under visible light illumination, *Journal of Colloid and Interface Science* 2013, 393, 126–129
- [112] S. Kohtani, S. Makino, A. Kudo, K. Tokumura, Y. Ishigaki, T. Matsunaga, O. Nikaido, K. Hayakawa, R. Nakagaki, Photocatalytic Degradation of 4-n-Nonylphenol under Irradiation from Solar Simulator: Comparison between BiVO₄ and TiO₂ Photocatalysts, *Chemistry Letters* 2002, 660-661
- [113] J. Yu, A. Kudo, Effects of Structural Variation on the Photocatalytic Performance of Hydrothermally Synthesized BiVO₄, *Adv. Funct. Mater.* 2006, 16, 2163–2169
- [114] C.A. Kudo, Selective Preparation of Monoclinic and Tetragonal BiVO₄ with Scheelite Structure and Their Photocatalytic Properties, *Chem. Mater.* 2001, 13, 4624-4628
- [115] C F.F. Abdi, R. van de Krol, R. Liu, Z. Huang, H.J. Lewerenz, B. Dam, M. Zeman, A.H.M. Smets, Efficient Water-Splitting Device Based on a Bismuth Vanadate Photoanode and Thin-Film Silicon Solar Cells, *ChemSusChem* 2014, 7, 2832 – 2838
- [116] K. Sayama, A. Nomura, T. Arai, T. Sugita, R. Abe, M. Yanagida, T. Oi, Y. Iwasaki, Y. Abe, H. Sugihara, Photoelectrochemical Decomposition of Water into H₂ and O₂ on Porous BiVO₄ Thin-Film Electrodes under Visible Light and Significant Effect of Ag Ion Treatment, *J. Phys. Chem. B* 2006, 110, 11352-11360
- [117] Y. Qiu, W. Liu, W. Chen, W. Chen, G. Zhou, P.C. Hsu, R. Zhang, Z. Liang, S. Fan, Y. Zhang, Y. Cui, Efficient solar-driven water splitting by nanocone BiVO₄-perovskite tandem cells, *Sci. Adv.* 2016, 2,6, 1501764-1501772

- [118] D. Ke, T. Peng, L. Ma, P. Cai, P. Jiang, Photocatalytic water splitting for O₂ production under visible-light irradiation on BiVO₄ nanoparticles in different sacrificial reagent solutions, *Applied Catalysis A: General* 208, 350, 111–117
- [119] J. Yu, Y. Zhang, A. Kudo, Synthesis and photocatalytic performances of BiVO₄ by ammonia co-precipitation process, *Journal of Solid State Chemistry* 2009, 182, 223–228
- [120] H. Jiang, H. Endo, H. Natori, M. Nagai, K. Kobayashi, Fabrication and photoactivities of spherical-shaped BiVO₄ photocatalysts through solution combustion synthesis method, *Journal of the European Ceramic Society* 2008, 28, 2955–2962
- [121] H. Liu, H. Hou, F. Gao, X. Yao, W. Yang, Tailored Fabrication of BiVO₄ Thoroughly Mesoporous Nanofibers and Their Visible Light Photocatalytic Activities, *ACS Appl. Mater. Interfaces* 2016, 8, 3, 1929–1936
- [122] W. Yin, W. Wang, L. Zhou, S. Sun, L. Zhang, CTAB-assisted synthesis of monoclinic BiVO₄ photocatalyst and its highly efficient degradation of organic dye under visible-light irradiation, *Journal of Hazardous Materials* 2010, 173, 194–199
- [123] L. Zhou, W. Wang, L. Zhang, H. Xu, W. Zhu, Single-Crystalline BiVO₄ Microtubes with Square Cross-Sections: Microstructure, Growth Mechanism, and Photocatalytic Property, *J. Phys. Chem. C* 2007, 111, 13659–13664
- [124] L. Zhou, W. Wang, S. Liu, L. Zhang, H. Xu, W. Zhu, A sonochemical route to visible-light-driven high-activity BiVO₄ photocatalyst, *Journal of Molecular Catalysis A: Chemical* 2006, 252, 120–124
- [125] H. Li, G. Liu, X. Duan, Monoclinic BiVO₄ with regular morphologies: Hydrothermal synthesis, characterization and photocatalytic properties, *Materials Chemistry and Physics* 2009, 115, 9–13
- [126] W.H. Zhang, W.D. Zhang, Fabrication of SnO₂–ZnO nanocomposite sensor for selective sensing of trimethylamine and the freshness of fishes, *Sensors and Actuators B: Chemical* 2008, 134, 403–408
- [127] M. Yan, H. Zhang, S. Li, X. Ma, M. Wang, D. Yang, A selective NH₃ gas sensor based on Fe₂O₃–ZnO nanocomposites at room temperature, *Sensors and Actuators B: Chemical* 2006, 114, 2, 910–915

- [128] T. Lu, L. Pan, H. Li, G. Zhu, T. Lv, X. Liu, Z. Sun, T. Chen, D.H.C. Chua, Microwave-assisted synthesis of graphene–ZnO nanocomposite for electrochemical supercapacitors, *Journal of Alloys and Compounds* 2011, 509, 5488–5492
- [129] Y. Zhang, Z.R. Tang, X. Fu, Y.J. Xu, TiO₂–Graphene Nanocomposites for Gas-Phase Photocatalytic Degradation of Volatile Aromatic Pollutant: Is TiO₂–Graphene Truly Different from Other TiO₂–Carbon Composite Materials, *ACS Nano* 2010, 4, 12, 7303–7314
- [130] L. Jiang, L. Gao, Fabrication and characterization of ZnO-coated multi-walled carbon nanotubes with enhanced photocatalytic activity, *Materials Chemistry and Physics* 2005, 91, 2–3, 313-316
- [131] R. Josel, A. Kumar, V. Thavasi, S. Ramakrishna, Conversion efficiency versus sensitizer for electrospun TiO₂ nanorod electrodes in dye-sensitized solar cells, *Nanotechnology* 2008, 19, 424004-424011
- [132] X. Yin, Z. Xue, L. Wang, Y. Cheng, B. Liu, High-Performance Plastic Dye-sensitized Solar Cells Based on Low-Cost Commercial P25 TiO₂ and Organic Dye, *ACS Appl. Mater. Interfaces* 2012, 4, 3, 1709–1715
- [133] K. Miyoshi, M. Numao, M. Ikegami, T. Miyasaka, Effect of Thin TiO₂ Buffer Layer on the Performance of Plastic-based Dye-sensitized Solar Cells Using Indoline Dye, *Electrochemistry* 2008, 2, 158-160
- [134] S.C. Liufu, H.N. Xiao, Y.P. Li, Thermal analysis and degradation mechanism of polyacrylate/ZnO nanocomposites, *Polymer Degradation and Stability* 2005, 87, 103-110
- [135] Y. Ooyama, S. Inoue, T. Nagano, K. Kushimoto, J. Ohshita, I. Imae, K. Komaguchi, Y. Harima, Dye-Sensitized Solar Cells Based On Donor–Acceptor p-Conjugated Fluorescent Dyes with a Pyridine Ring as an Electron-Withdrawing Anchoring Group, *Angew. Chem.* 2011, 123, 7567 –7571
- [136] N. Hirata, J.J. Lagref, E.J. Palomares, J.R. Durrant, M.K. Nazeeruddin, M. Gratzel, D. Di Censo, Supramolecular Control of Charge-Transfer Dynamics on Dye sensitized Nanocrystalline TiO₂ Films, *Chem. Eur. J.* 2004, 10, 595 -602

- [137] S. Haid, M. Marszalek, A. Mishra, M. Wielopolski, J. Teuscher, J.E. Moser, R. Humphry-Baker, S.M. Zakeeruddin, M. Grätzel, P. Bäuerle, Significant Improvement of Dye-Sensitized Solar Cell Performance by Small Structural Modification in π -Conjugated Donor–Acceptor Dyes, *Adv. Funct. Mater.* 2012, 22, 1291–1302
- [138] K. Hara, M. Kurashige, Y. Dan-Oh, C. Kasada, A. Shinpo, S. Suga, K. Sayama, H. Arakawa, Design of new coumarin dyes having thiophene moieties for highly efficient organic-dye-sensitized solar cells, *New J. Chem.* 2003, 27, 783–785
- [139] H. Tian, X. Yang, R. Chen, Y. Pan, L. Li, A. Hagfeldt, L. Sun, Phenothiazine derivatives for efficient organic dye-sensitized solar cells, *Chem. Commun.* 2007, 3741–3743
- [140] L. Schmidt-Mende, U. Bach, R. Humphry-Baker, T. Horiuchi, H. Miura, S. Ito, S. Uchida, M. Grätzel, Organic Dye for Highly Efficient Solid-State Dye-Sensitized Solar Cells, *Adv. Mater.* 2005, 17, 7, 813-815
- [141] M. Saito, S. Fujihara, Large photocurrent generation in dye-sensitized ZnO solar cells, *Energy Environ. Sci.* 2008, 1, 280-283
- [142] A. Fattori, L.M. Peter, K.L. McCall, N. Robertson, F. Marken, Adsorption and redox chemistry of cis-RuLL'(SCN)₂ with L=4,4'-dicarboxylic acid-2,2'-bipyridine and L'=4,4'-dinonyl-2,2'-bipyridine (Z907) at FTO and TiO₂ electrode surfaces, *J. Solid State Electrochem* 2010, 14, 1929-1936
- [143] A. Mishra, M.K.R. Fischer, P. Buerle, Metal-Free Organic Dyes for Dye-Sensitized Solar Cells: From Structure: Property Relationships to Design Rules, *Angew. Chem. Int. Ed.* 2009, 48, 2474–2499
- [144] I.N. Obotowo, I.B. Obot, U.J. Ekpe, Organic sensitizers for dye-sensitized solar cell (DSSC): Properties from computation, progress and future perspectives, *Journal of Molecular Structure* 2016, 1122, 80-87
- [145] D. Kuang, S. Uchida, R. Humphry-Baker, S.M. Zakeeruddin, M. Grätzel, Organic Dye-Sensitized Ionic Liquid Based Solar Cells: Remarkable Enhancement in Performance through Molecular Design of Indoline Sensitizers, *Angew. Chem. Int. Ed.* 2008, 47, 1923 –1927

- [146] M. Liang, W. Xu, F. Cai, P. Chen, B. Peng, J. Chen, Zh. Li, New Triphenylamine-Based Organic Dyes for Efficient Dye-Sensitized Solar Cells, *J. Phys. Chem. C* 2007, 111, 4465-4472
- [147] K. Sayama, K. Hara, N. Mori, M. Satsuki, S. Suga, S. Tsukagoshi, Y. Abe, H. Sugihara, H. Arakawa, Photosensitization of a porous TiO₂ electrode with merocyanine dyes containing a carboxyl group and a long alkyl chain, *Chem. Commun.* 2000, 1173-1174
- [148] K. Woan, G. Pyrgiotakis, W. Sigmund, Photocatalytic Carbon-Nanotube–TiO₂ Composites, *Advanced Materials* 2009, 21, 5, 2233–2239

Chapter 2

Quantum-chemical calculations

Schrödinger's equation is the basic differential equation for quantum chemistry, dependent on time and on all of the spatial coordinates necessary to describe the system at hand. The equation was formulated at the end of 1925 by Erwin Schrödinger. It describes changes in the quantum state of electronic systems over time. The system status is described by the wave function Ψ also called the quantum state of the system under discussion. In the standard interpretation of the quantum mechanics, the wave function gives a complete description of a physical system. Description of the change in wave function over time gives a possibility to call the Schrödinger equation time depending. The solution of differential wave equation allows to find the wave function Ψ that carries information about the distribution of electrons and nuclei in a space defining a molecule. The time form of the Schrodinger equation is defined as:

$$\hat{H}\Psi_n = i\hbar \frac{\partial \Psi_n}{\partial t} \quad \text{where} \quad n = 1, 2, \dots, \infty. \quad (2.1.)$$

The \hat{H} is Hamilton operator corresponding to the total energy of the system; Ψ_n is a wave function describing the quantum state n . When the Hamilton operator is independent of time the stationary Schrödinger equation looks as follows:

$$\hat{H}\Psi_n = E_n \Psi_n \quad \text{where} \quad n = 1, 2, \dots, \infty. \quad (2.2.)$$

The E_n is the energy of the state n . The Hamilton operator takes a form:

$$\hat{H} = -\frac{\hbar^2}{2m_e} \sum_i \nabla_i^2 - \sum_k \frac{\hbar^2}{2M_k} \nabla_k^2 + \sum_{j>i=1} \frac{1}{4\pi\epsilon_0} \frac{e^2}{|r_i - r_j|} - \sum_{i,k} \frac{1}{4\pi\epsilon_0} \frac{Z_e e^2}{|r_i - R_k|} + \sum_{l>k=1} \frac{1}{4\pi\epsilon_0} \frac{Z_k Z_l e^2}{|R_k - R_l|} \quad (2.3.)$$

where: R_k, R_l - are vectors of the k and l nuclei positions; r_i, r_j - define a position of the i and j electrons; M - mass of nuclei; m_e - mass of electron and $\nabla_i^2 = \frac{\partial^2}{\partial x_i^2} + \frac{\partial^2}{\partial y_i^2} + \frac{\partial^2}{\partial z_i^2}$

[1]. The part of the above presented equation corresponding to the $-\frac{\hbar^2}{2m_e} \sum_i \nabla_i^2$ and the

$\sum_k \frac{\hbar^2}{2M_k} \nabla_k^2$ represents the kinetic energy of electrons and nucleus, respectively. The $\sum_{j>i=1} \frac{1}{4\pi\epsilon_0} \frac{e^2}{|r_i - r_j|}$, $\sum_{i,k} \frac{1}{4\pi\epsilon_0} \frac{Z_e e^2}{|r_i - R_k|}$ and $\sum_{l>k=1} \frac{1}{4\pi\epsilon_0} \frac{Z_k Z_l e^2}{|R_k - R_l|}$ presents the potential energy

of an electrostatic interactions: electron-electron, electron-nucleus and nucleus-nucleus, respectively.

Electrons are much lighter than nucleons located in the atomic nucleus. The rest mass of the electron is equal to $9,1094 \cdot 10^{-31} kg$ but the rest mass of the proton is equal to $1,6726 \cdot 10^{-27} kg$. This means that the motion of the nuclei relative to electron motion is practically negligible. One may say also that observing the movement of "heavy" nuclei the rapidly moving electrons will be practically indescribable to the observer.

Assuming that the motion of the nuclei is insignificant in relation to electron motion the motion of nuclei may be suppressed. Separation of the electron system from the nucleus in a given atom is called adiabatic approximation. In consequence of the mentioned approximation the total wave function may be written as:

$$\Psi_n = \psi_n(r, R) f_n(\vec{R}) \quad (2.4)$$

The $\psi_n(r, R)$ is an electron part of wave function depending on coordinates of the electrons r and parameterised on nucleus position. The nucleus part of the wave function $f_n(\vec{R})$ shows dependence not only on the value of the parameter R , but also on the direction of its vector [2]. The resulting assumption allows to separate electron Hamiltonian from nuclear part. As a result of this operation is received:

$$\text{the electron part} \quad \hat{H}^e(r, R) \psi_n(r, R) = E_n^e(r, R) \psi_n(r, R) \quad (2.5.)$$

with the electron Hamiltonian:

$$\hat{H}^e(r, R) = -\frac{\hbar^2}{2m_e} \sum_i \nabla_i^2 + \sum_{j>i=1} \frac{1}{4\pi\epsilon_0} \frac{e^2}{|r_i - r_j|} - \sum_{i,k} \frac{1}{4\pi\epsilon_0} \frac{Z_e e^2}{|r_i - R_k|} \quad (2.6.)$$

and the nuclear part
$$\hat{H}^N(R) f_n(R) = E_n^N f_n(R) \quad (2.7.)$$

with the nuclear Hamiltonian:

$$\hat{H}^J(R) = -\sum_k \frac{\hbar^2}{2M_k} \nabla_k^2 + E_n^e(R) + E_{ad}(R) \quad (2.8.)$$

where $E_{ad}(R) = \int \psi^* \hat{T}_J \psi d\tau_e$ is an average value of kinetic energy operator of nucleus motion [2]. When the nuclear kinetic energy is neglected one may subtract the kinetic energy operator \hat{T} from the Hamiltonian. In this way the last part of the Equation 2.8 is omitted. This procedure is called the Born-Oppenheimer's approximation.

2.1. Hartree-Fock methodology

The Hartree-Fock method is widely used in quantum chemistry, atomic physics, and condensed matter physics, where it allows an approximate solution of the Schrödinger equation for a multiple particle system. It is the basis of the *ab initio* computational method. The Hartree-Fock method is based on the variational principle which specifies that the grand state energy of the given system calculated as an expected value from proposed wave function is always greater than, or equal to, the energy that is the exact solution of the Schrödinger equation. The studied system of N electrons can be described by the wave function Ψ^{HF} composed by the N spinorbitals $\varphi_i(\tau_j)$ in the form of the Slater determinant:

$$\Psi^{HF} = \frac{1}{\sqrt{N!}} \begin{vmatrix} \varphi_1(\tau_1) & \varphi_2(\tau_1) & \dots & \varphi_N(\tau_1) \\ \varphi_1(\tau_2) & \varphi_2(\tau_2) & \dots & \varphi_N(\tau_2) \\ \vdots & \vdots & \ddots & \vdots \\ \varphi_1(\tau_N) & \varphi_2(\tau_N) & \dots & \varphi_N(\tau_N) \end{vmatrix} \quad (2.9.)$$

The spinorbitals dependent on coordinates of the individual electrons. It is constructed as the product of a spin function dependent on the spin variable of an electron and an orbital function dependent on the particle's spatial variations [3].

The Hartree-Fock method is an iterative minimization of the energy of the system calculated by changing of the form of spinorbitals. This procedure is reduced to the solution of the Hartree-Fock equation similar in character to the time-independent Schrödinger equation:

$$\hat{F} \varphi_i(\tau_i) = \varepsilon_i \varphi_i(\tau_i). \quad (2.10.)$$

The ε_i can be interpreted as an energy of electron described by spinorbital φ_i in the field of other electrons. The \hat{F} is called Fock operator and it has the form:

$$\hat{F} = -\frac{\hbar^2}{2m_e} \nabla_{r_i}^2 + \hat{V}_{eN}(r_i) + e^2 \sum_j \hat{J}_j - \hat{K}_j \equiv \hat{h}_i + e^2 \sum_j \hat{J}_j - \hat{K}_j. \quad (2.11.)$$

where $\frac{\hbar^2}{2m_e} \nabla_{r_i}^2$ is the operator of the kinetic energy of the electron i , $\hat{V}_{eN}(r_i)$ is the operator of an electrostatic interaction of the electron i with the nuclei. The \hat{h}_i is an one electron Hamiltonian. The \hat{J}_j is the Coulomb operator of an electrostatic interaction occurring between the electron i and the electron j . Its action on the wave function φ_i may be defined by integral:

$$\hat{J}_j \varphi_i(\tau_1) = \int \varphi_j^*(\tau_2) \frac{1}{|r_2 - r_1|} \varphi_j(\tau_2) d\tau_2 \cdot \varphi_i(\tau_1). \quad (2.12.)$$

The \hat{K}_j called exchange operator does not have classical counterpart. Its action on φ_i causes a “spinorbital exchange” from φ_i to φ_j .

$$\hat{K}_j \varphi_i(\tau_1) = \int \varphi_j^*(\tau_2) \frac{1}{|r_2 - r_1|} \varphi_i(\tau_2) d\tau_2 \cdot \varphi_j(\tau_1). \quad (2.13.)$$

Total electrons energy in the Hartree-Fock method is defined as:

$$E = \sum_{i=1}^n I_i + \sum_{i>j=1}^n (J_{ij} - K_{ij}). \quad (2.14.)$$

where the n is a number of electrons. The I_i is one-electron integral, which can be written as:

$$I_i = \int \varphi_i^*(k) \hat{h}(k) \varphi_i(k) d\tau_k . \quad (2.15.)$$

The J_{ij} and the K_{ij} are two-electron integrals, coulomb and exchange, respectively defined as:

$$J_{ij} = \int \varphi_i^*(i) \varphi_j^*(j) \frac{e^2}{r_{ij}} \varphi_i(i) \varphi_j(j) d\tau_i d\tau_j . \quad (2.16.)$$

and

$$K_{ij} = \int \varphi_i^*(i) \varphi_j^*(j) \frac{e^2}{r_{ij}} \varphi_i(j) \varphi_j(i) d\tau_i d\tau_j . \quad (2.17.)$$

The exchange integral K_{ij} is different from zero only for parallel spin-directed electrons. As a consequence, the triplet state always has less energy than the singlet state with the same electron configuration.

2.2. Density functional theory (DFT)

Density functional theory (DFT) is one of the quantum chemical modelling methods used in physics and chemistry to study the electronic structure of molecules and periodic systems. It is one of the most popular and versatile methods available in condensed matter physics. It uses the fact that the properties of the system can be described by the density function, i.e. the function dependent on the spatial density of the electrons. Compared to the Hartree-Fock method, it is less computationally demanding and more affordable to use because it is not based on calculations related to many complex wave functions of electrons. Despite all the positive aspects of the DFT method, one still encounter computational difficulties, inter alia: intermolecular interactions, in particular van der Waals forces, transient states or bands gap in semiconductors. The key of the method is to introduce instead of the wave function of the electron state their density description:

$$\rho(r) = N \sum |\psi(r_1, r_2, \dots, r_N)|^2 dr_2 dr_3 \dots dr_N . \quad (2.18.)$$

where $\rho(r)$ is electron density of the ground state and N is the number of electrons. Another important element is the introduction of the concept of the functional, which determines the average value of the ground state energy described by the formula:

$$E[\rho] = F[\rho] + \int V_{ext}(r)\rho(r)dr. \quad (2.19.)$$

where $F[\rho] = \langle \psi | \hat{T} + \hat{W} | \psi \rangle$ functional depends on the kinetic energy \hat{T} and the Coulomb interaction \hat{W} . The $\int V_{ext}(r)\rho(r)dr$ describes interaction of electrons with the outer potential of atomic nuclei. Characters of the functional cannot be fully characterized.

The method to find the functional $F[\rho]$ was proposed by Kohn and Sham. It involves the projection of a real electron system into an auxiliary, hypothetical system of non-interacting electrons, moving in an effective potential describing the electrostatic effects of the nuclei and other electrons as well as the correlation-exchange potential. The prerequisite for this simplification is the constant density of electrons in both, the original and the newly generated system. The functional takes the form:

$$F[\rho] = T_0[\rho] + W_0[\rho] + E_{xc}[\rho]. \quad (2.20.)$$

where the $E_{xc}[\rho]$ is the correlation-exchange energy. The mentioned energy is a consequence of the disruption of the electron density distribution. This phenomena may arise from the interactions of external or intermolecular fields.

The equivalent of the Hartree-Fock equation in the DFT theory is the Kohn-Sham equation (KS):

$$\left(-\frac{\hbar^2}{2m} \frac{\partial^2}{\partial r^2} + V_{KS}(r) \right) \Psi_n(r) \equiv \hat{H}_{KS} \Psi_n(r) = \varepsilon_n \Psi_n(r). \quad (2.21.)$$

The effective potential in the KS theory describing the non-interacting electron system takes the form:

$$V_{KS}(r) = V_{ext}(r) + e^2 \int \frac{\rho(r_2)}{|r_1 - r_2|} dr_2 + v_{xc}(r). \quad (2.22.)$$

The correlation-exchange potential $v_{xc}(r)$ is defined as an correlation-exchange energy derivative by electron density and is described by the formula:

$$v_{xc}(r) \equiv \frac{\partial E_{xc}(\rho)}{\partial \rho(r)}. \quad (2.23.)$$

Knowledge of the correlation-exchange potential allows to determine the value of the total energy of a given system. The mentioned energy may be defined by an equation [4]:

$$E[\rho] = 2 \sum_{N=1}^{N/2} \epsilon_N - \frac{e^2}{2} \int \frac{\rho(r_1)\rho(r_2)}{|r_1 - r_2|} dr_1 dr_2 + E_{xc}[\rho] - \int \rho(r) v_{xc}(r) dr. \quad (2.24.)$$

2.2.1. Generalized gradient approximation (GGA)

DFT reduces the quantum mechanical ground state many-electron problem to self-consistent one-electron form, through the Kohn-Sham equation. However, in practical calculations, the exchange-correlation energy as a functional of the density must be approximated. The simplest approximation is the local density approximation (LDA). It says that the E_{XC} depends only on the (local) density at a given point. It defined the exchange and correlation energy of homogeneous electron gas. In this approximation, the exchange-correlation energy at each point of the real space is assumed to be equal to that energy of a uniform electron gas with the same electronic density.

$$E_{xc}^{LDA}[\rho] = \int \rho(r) \epsilon_{xc}^{hg}(\rho(r)) d^3r. \quad (2.25.)$$

where $\epsilon_{xc}^{hg}(\rho(r))$ is the exchange-correlation energy per electron in a homogeneous electron gas with a density $\rho(r)$.

An improvement in the accuracy provided by the LDA can be obtained by generalised gradient approximation (GGA) functional. In the GGA approximation the functional depends on local density and its gradient. The basic idea of the GGAs is to express the exchange correlation energy in the following form:

$$E_{xc}^{GGA} = E_{xc}^{LDA} + \int F_{xc}(\rho[r], \nabla \rho[r]) dr. \quad (2.26.)$$

where the exchange part can be written as

$$E_X^{GGA} = E_X^{LDA} - \sum_{\sigma} \int F(s_{\sigma}) \rho_{\sigma}^{4/3}(\mathbf{r}) d\mathbf{r}. \quad (2.27.)$$

The function F is a reduced density gradient for spin σ and s_{σ} is a local inhomogeneity parameter:

$$s_{\sigma}(\mathbf{r}) = \frac{|\nabla \rho_{\sigma}(\mathbf{r})|}{\rho_{\sigma}^{4/3}(\mathbf{r})}. \quad (2.28.)$$

Function F based on GGA exchange functional was developed for example by Becke (B88) and Perdew (P), by Lacks and Gordon (LG) or by Perdew, Burke and Ernzerhof (PBE). These functionals base on exact properties without using empirical parameters. The most popular correlation functional was implemented by Lee, Yang and Parr (LYP).

The exchange-correlation functional is usually written as the sum of an “exchange” part and a “correlation” part, where the first one contains only same-spin interactions, while the second one contains both same-spin and opposite-spin interactions.

2.2.2. Perdew-Burke-Ernzerhof (PBE) functional

The GGA functionals one may divide into two groups for example, the functionals that contain empirical parameters whose values have been fitted to reproduce experiment or more accurate calculations and the functionals with no empirically determined parameters. Different functionals might give different results for any particular configuration of atoms, it is important to select the functional that best suits the characteristics of the system. An example of a non-empirical GGA functional is the Perdew-Burke-Ernzerhof (PBE) functional.

The enhancement factor of the exchange functional mentioned in (2.27.) applied into PBE methodology takes the form:

$$F_x^{PBE}(s) = 1 + \kappa - \frac{\kappa}{\left(1 + \frac{\mu}{\kappa} s^2\right)}. \quad (2.29.)$$

where $\kappa = 0.804$ is set to the maximum value allowed by the local Lieb-Oxford bound on E_{XC} and $\mu = 0.21951$ represents the set to recover the linear response of the uniform gas that the effective gradient coefficient for exchange cancels that for correlation [5].

2.3. Plane-wave method

In previous chapter (2.2) the theory of the density functional was discussed. There the multi-element systems of interacting electrons and ions were reduced to the problem of individual particles moving in the effective potential. Despite the above described simplification, problematic becomes the analysis of the bulk, infinite systems. The crystal is described by a cell with a finite number of atoms repeating in all three directions in space. The cell can be described as either a primitive cell or a supercell which consists of a group of atoms forming the studied crystal by a repetition.

In a crystal, regular arrangement, the potential in the Kohn-Sham equation is a periodic function of lattice vectors. In this way a wave function should satisfied the Bloch theorem:

$$\psi_{n,\vec{k}}(\vec{r}) = \sum_{\vec{G}} c_{\vec{G}}^{n,\vec{k}} e^{i(\vec{k}+\vec{G})\vec{r}} \quad (2.30.)$$

where n is energy band index, \vec{k} is wave vector, \vec{G} is reciprocal space vector. The summation takes place after vectors \vec{G} for which $\hbar^2 \left| \frac{\vec{k}+\vec{G}}{2m} \right|^2 < E_{cut-off}$. The $E_{cut-off}$ describes the maximum of the kinetic energy of the plane-wave. The Kohna Sham equation in the Bloch function notation can be presented as follows:

$$\left[\frac{p^2}{2m} + \vec{v}_{ef}(\vec{r}) \right] \psi_{n,\vec{k}}(\vec{r}) = E_{n,\vec{k}} \psi_{n,\vec{k}}(\vec{r}). \quad (2.31.)$$

where \vec{v}_{ef} is the effective potential.

In the representation of plane-waves, Kohn-Sham equations take on a very simple form. Substituting the trench (2.30) to equ. (2.29), and then multiplying by $e^{i(\vec{k}+\vec{G})\vec{r}}$ and by integrating after r we obtain the equation for our own values

$$\sum_{\vec{G}'} \left[\frac{\hbar^2}{2m} |\vec{k} + \vec{G}| \delta_{\vec{G}\vec{G}'} + \vec{v}_{ef}(\vec{G} - \vec{G}') \right] c_{\vec{G}}^{n,\vec{k}} = E_{n,\vec{k}} c_{\vec{G}'}^{n,\vec{k}}. \quad (2.32.)$$

Where $\vec{v}_0(\vec{G} - \vec{G}') = \vec{v}_H(\vec{G} - \vec{G}') + \vec{v}_{XC}(\vec{G} - \vec{G}') + \vec{v}_{ext}(\vec{G} - \vec{G}')$.

A solution of the above equation is obtained by diagonalizing the Hamiltonian matrix with matrix elements $H_{\vec{k}+\vec{G},\vec{k}+\vec{G}'}$. The size of the matrix depends on the choice of cut-off energy and it becomes very large for systems containing both valence electrons and core electrons. This is a significant problem, but it can be solved after applying the approximation of pseudopotentials [6].

Most physical and chemical properties of crystals depend to a very good approximation only on the distribution of the valence electrons. The core electrons do not participate in the chemical bond. They are strongly localized around the nucleus, and their wave functions overlap only very little with the core electron wave functions from neighboring atoms. Therefore, the distribution of the core electrons basically does not change when the atoms are placed in a different chemical environment. It is thus justified to assume the core electrons to be “frozen” and to keep the core electron distribution of the isolated atom in the crystal environment.

2.3.1. Born-von Karman boundary conditions

The periodic boundary conditions or Born-von Karman boundary conditions impose restrictions that the wave function must be periodic in the certain Bravais lattice. It is used to describe the physical properties of the systems based on the model of ideal crystal in solid state physics. The condition can be stated as:

$$\psi(r) = \psi(r + N_i a_i) . \quad (2.33.)$$

where i runs over the dimensions of the Bravais lattice, the a_i are the primitive vectors of the lattice, and the N_i are integers assuming the lattice has N cells where $N=N_1 \times N_2 \times N_3$ [7].

The Born–von Karman boundary conditions provide a mathematical device to get around the physical effects of boundaries. In one dimension, the device forms the lattice into a circle of cells. To insure that there is no discontinuity of the wave function, it is required that:

$$\psi(x) = \psi(x + N_x a_x) . \quad (2.34.)$$

Because the $k_x = 2\pi m/N_x a_x$, where m is an integer, in the reduced zone must be $-\pi/a_x < k_x < \pi/a_x$. In this way the integer m goes from $-(1/2)N_x$ to $+(1/2)N_x$. The number of allowed wave vectors in the Brillouin zone equals the number of unit cells in the crystal.

2.4. Semi-empirical methods in quantum chemistry

The semi-empirical methods of quantum chemistry are based on Hartree-Fock formalism (**Chapter 2.1.**) with its simplification and approximation of certain parameters obtained from experiments. They are widely used in quantum chemistry for large particle systems because of considerably less computational cost than the *ab initio* method. In addition, the use of empirical parameters allows for some effects of electron correlation to be taken into account. The development of semi-empirical methods assumes that the Hartree-Fock formalism can be approximated or completely neglected at the level of the two-electron integrals J_{ij} and K_{ij} (**Equation 2.16. and 2.17.**). Instead of calculating these integrals, the parameters best describing an experimental data or *ab initio* calculations are introduced. The obtained results may be wrong when the calculated molecule differs from the system for which the parameterization was done. Also the chosen properties can be calculated only by the semi-empirical methods developed to calculate the given properties. The semi-empirical methods are most commonly used for organic chemistry, where the molecules are composed of several types of atoms, resulting in relatively easy parameterization.

The oldest semi-empirical method completely neglecting the two-electron integrals is called Hückel method and the extended Hückel method. The Hückel method treats quantum mechanically only π electrons and is intended for calculations of aromatic conjugated molecules. Extended Hückel method takes into account all the valence electrons. Among the other semi-empirical methods we can distinguish two basic groups:

- Methods in which only π electrons are quantum mechanically treated. The most important of these ones is the PPP (Pariser-Parr-Pople) method, which mainly serves to calculate excited states of the π -electrons [8,9].
- Methods in which all valence electrons are quantum mechanically treated. They include: CNDO, INDO, NDDO methods introduced by John Pople. Parameters are not based on experimental results, but on *ab initio* calculations with minimal basis set. They are currently rarely used, but they make a significant contribution to the development of methodology [10].

- Methods as MINDO, MNDO, AM1, PM3, PM6, RM1 and SAM1 are parameterized using experimental enthalpy of formation, dipole moments, ionization potential and geometric parameters [11]. There are also methods developed for the calculation of excited states (thus predicting electron spectra), such as ZINDO and ZINDO/S [12].

PM6 parameterization method

Over the past 40 years, the NDDO and MNDO-type methods been refined [13,14]. Numerous changes were made in the MNDO methodology. The most important of them was an addition of *d* orbitals to the main group elements and an introduction of diatomic parameters. In consequence the PM3 method was created [15]. By its improving the next step was a development of the PM6 parametrized method. It includes a correction in the core-core interactions defined as follows:

$$E_n(A, B) = Z_A Z_B \langle s_A s_A | s_B s_B \rangle \left(1 + x_{AB} e^{-\alpha_{AB}(R_{AB} + 0.0003 R_{AB}^6)} \right). \quad (2.35.)$$

and resulting in a convergence increasing by the addition of small perturbation. The PM6 method contains atomic and diatomic parameters for 70 elements, including transition metal groups, not previously introduced in any semi-empirical computational methods [16].

2.5. References

- [1] W. Koch, M. C. Holthausen, A Chemist's Guide to Density Functional Theory, Second Edition, Wiley-VCH., 2000, 3-5
- [2] W. Kolos, Chemia kwantowa, PWN, Warszawa 1978, p115-116
- [3] Martin J. Field, A Practical Introduction To The Simulation Of Molecular Systems, Second Edition, Institut de Biologie Structurale – Jean-Pierre Ebel, Grenoble, France, p.55,56
- [4] M. Makowska-Janusik, Wpływ matryc polimerowych na wybrane własności nieliniowo-optyczne materiałów kompozytowych, 132-146
- [5] J.P. Perdew, K. Burke, M. Ernzerhof, Generalized gradient approximation made simple, *Physical Review Letters* 1996, 77, 18, 3865-3868

- [6] L. O. Jay, H. Kim, Y. Saad, and J. R. Chelikowsky, Electronic structure calculations using plane wave codes without diagonalization, *Comput. Phys. Comm.* 1999, 118, 21–30.
- [7] E. Kaxiras, Atomic and electronic structure of solid, *Cambridge*, p87
- [8] Jan Linderberg, Yngve öhrn, Derivation and Analysis of the Pariser–Parr–Pople Model, *The Journal of Chemical Physics* 1968, 49, 716
- [9] J. A. Pople, Electron Interaction In Unsaturated Hydrocarbons, *Cambridge* 1953, p.1375-1385
- [10] John A. Pople, David L. Beveridge, *Approximate Molecular Orbital Theory*, McGRAW-Hill Book Company, 1970
- [11] K. I. Ramachandran · G. Deepa · K. Namboori, *Computational Chemistry and Molecular Modeling Principles and Applications*, 2008 Springer-Verlag Berlin Heidelberg, p.141
- [12] Kenny B. Lipkowitz, Donald B. Boyd, Reviews in Computational Chemistry vol.17, *John Wiley & Sons*, Inc. 2001
- [13] J. A. Pople, Approximate Self-Consistent Molecular-Orbital Theory. V. Intermediate Neglect of Differential Overlap, *J. Chem. Phys.* 1961, 47, 6
- [14] M. J.S. Dewar, W. Thiel, Ground States of Molecules. The MNDO Method. Approximations and Parameters, *J Am Chem Soc* 1977, 99, 4907–4917
- [15] J.J.P. Stewart, Optimization of Parameters for Semiempirical Methods I. Method, *J Comp Chem* 1989, 10, 209–220
- [16] J.J.P. Stewart, Optimization of parameters for semiempirical methods V: Modification of NDDO approximations and application to 70 elements, *J Mol Model* 2007, 13, 1173–1213

Chapter 3

Characterization techniques

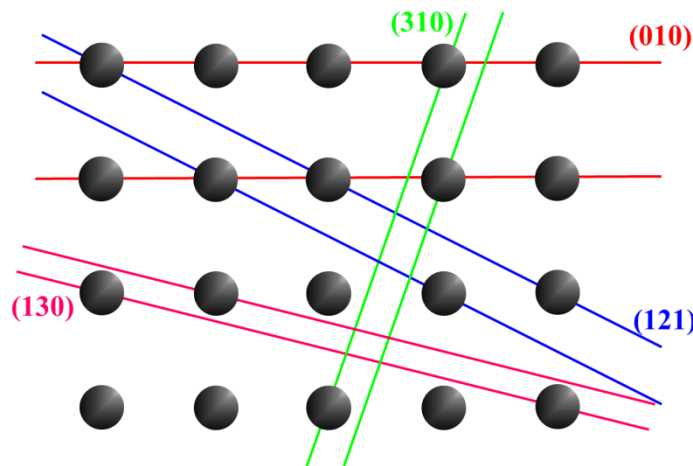
3.1. X-ray diffraction (XRD)

X-ray based technique such as diffraction is well-known and widely used research tool in the field of solid state physics, crystallography and material sciences. For many years, it was a technique used mainly for scientific research related to determine the structure of crystallographic networks of various substances, the determination of their unite cells and lattice parameters. The X-ray based techniques has shown also an evolution to cover innovative areas such as tomography or non-destructive testing. Such applications include, for example, the determination of a phase composition of materials, the measurement of stresses and the determination of a material texture. An important factor in increasing the use of X-ray based techniques in material laboratories was the progress in the construction of X-ray diffractometers (construction of portable devices) and the creation of specialized databases and computer programs to facilitate the relatively complex analysis of diffraction data.

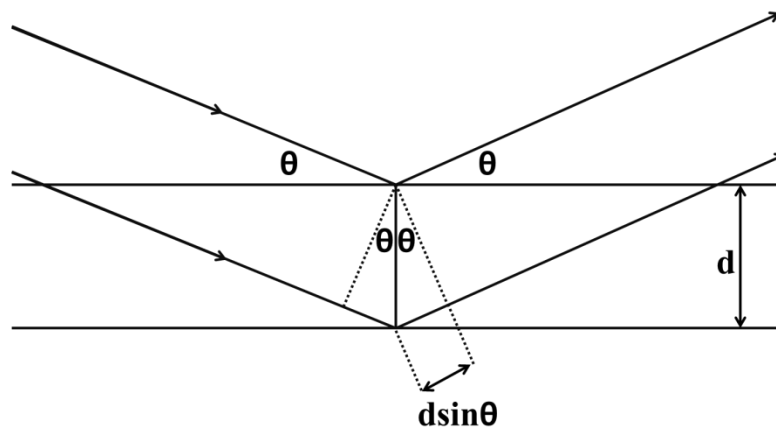
Based on the diffraction method one may address the wide number of the compounds encountered in nature exhibiting a crystalline structure that is composed of atoms arranged in a regular and strictly structured manner determined by the crystallographic phase. The size of individual crystals or the crystalline domains within a given network can be very different. Thus, single monocrystals or polycrystalline materials can be in the size of centimetres as well as is micrometres. These features can be characteristic of materials as metals or ceramics which show polycrystalline compositions consisting of a large number of crystallites randomly arranged in the volume of material.

The techniques used in X-ray diffraction are dependent on whether the object under examination is a single monocrystalline or a polycrystalline sample, but the main idea of the diffraction phenomena remains unchanged regardless of the organization of matter. The **Schema 3.1.1.** shows a diagram of the atoms arrangement in a simple crystallographic network with a highlight on the reticular crystallographic planes.

Atoms of the network can be joined by different parallel groups of crystallographic planes. Some groups of planes as the (010) are densely arranged with atoms and others, such as (310), contain less atoms. It can be addressed that a family of plane plays the role of a grid which diffracts the X-ray beam according to defined conditions depending on the X-ray wavelength, an incidence angles and the lattice orientation (**Schema 3.1.2**).



Schema 3.1.1. An exemplary arrangement of atoms in a crystalline lattice with the designed different groups (families) of mutually parallel crystallographic planes



Schema 3.1.2. Diagram of X-ray reflection from two parallel atomic planes

The condition that must be fulfilled to obtain constructive X-ray diffraction was reported by Bragg in 1913 and is called Bragg's Law [1]:

$$2d\sin(\theta) = n\lambda, \quad (3.1.1.)$$

where n is a positive integer and λ is the wavelength of the incident radiation. One of the important conclusions of this equation is the general requirement for the wavelength of X-rays that can be used in diffractometric studies. As $\sin(\theta)$ is always ≤ 1 and $n \geq 1$, any diffraction lines from the crystal must lead to the condition:

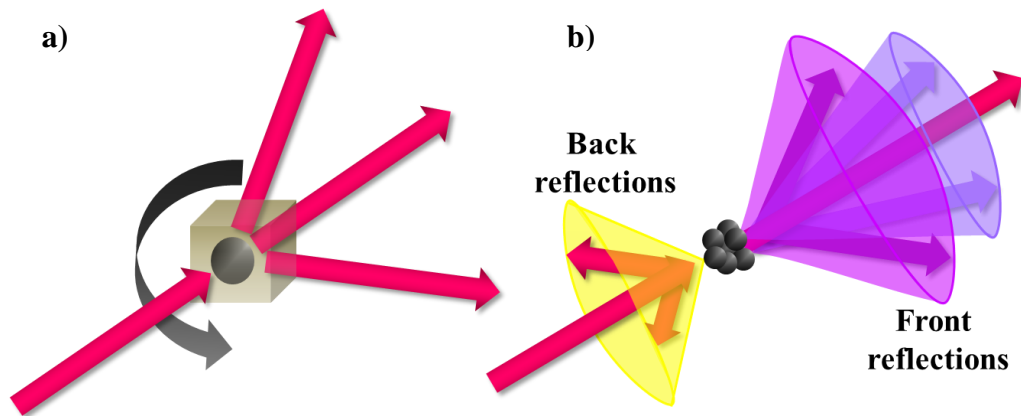
$$\lambda \leq 2d_{max}, \quad (3.1.2.)$$

with d_{max} the largest inter-reticular distance involved in the crystalline structure. Since the dimensions of the crystal cell are in order of several angstroms ($1 \text{ \AA} = 10^{-10} \text{ m}$) the X-ray wavelengths of the same order must be used. The relationship between the wavelength of the X-ray and its energy expressed in keV is given by the formula:

$$E(\text{keV}) = \frac{12,4}{\lambda(\text{\AA})}. \quad (3.1.3.)$$

Typical X-ray energies used in XRD studies are between 10 and 50 keV and are therefore significantly lower than those used in classical industrial radiography.

The Bragg condition leads to the strong diffraction lines which are observed only for certain strictly defined monocrystalline orientations. In order to observe the characteristic XRD lines of a defined crystalline structure, the crystal should be rotated while simultaneously recording the overall XRD pattern. This technique is known as the rotating crystal which is used in solid state physics to determine the crystallographic structure of monocrystals. In technical applications one may deal with polycrystalline materials consisting of a large number of small, accidentally oriented crystals for which a powder method is applied as outlined in **Schema 3.1.3**.



Schema 3.1.3. a) X-ray Diffraction from a single crystal, **b)** Diffraction reflections from a polycrystalline (powder) sample consisting of a large number of fine, randomly oriented crystallites

Among the large number of randomly oriented crystallites, there will always be those whose the orientation permits to fulfil the condition for certain groups of inter-reticular planes. Thus diffraction lines from different crystallites must always lie on one cone defined by X-rays diffracted at 2θ relative to the incident X-ray beam (**Schema 3.1.3.b**). Diffraction lines from different families of inter-reticular planes differing by their distances d , will form separate cones of different 2θ angles (**Schema 3.1.3.b**). In usual X-ray diffraction studies, angular positions of the different inter-reticular planes compose the diffraction pattern [2,3].

For the investigations carried out in present work the Empryan diffractometer from PANalytical with Cu $K\alpha$ radiation ($\lambda = 0.15418$ nm) under an accelerating voltage of 45 kV and an emission current of 30 mA was used. The scale of 2θ angle was fixed between 15 - 60°.

3.2. Scanning electron microscopy (SEM)

An electron microscope uses an electron beam which can be deflected and focused by electromagnetic lenses. It gives a higher resolution than the optical microscope due to the de Broglie wavelength corresponding to electrons, shorter by several orders of magnitude than the wavelength of light. Electron microscope resolution is however limited by diffraction effects.

The characteristics and quality of the scanning electron microscope (SEM) depends on the structure of the microscope and on the type of signal used to produce the image. The resolution capacity for optical systems depends on the wavelength of light λ and the

optical efficiency of the aperture-conditioned optical system which is defined by the Abbe equation:

$$d = \frac{1,22 \cdot \lambda}{n \cdot \sin \theta} . \quad (3.2.1.)$$

The theoretical resolution of the electron microscope depends on the voltage that accelerates the electrons. The electron beam is subject to optical laws by showing not only the corpuscular characteristics, but also the wave nature. The wavelength associated with the moving particle of matter according to de Broglie equation is:

$$\lambda = \frac{h}{m \cdot v} = \frac{h}{p} . \quad (3.2.2.)$$

The kinetic energy of electrons depends on the potential difference between the cathode and the anode, called the accelerating voltage. Taking into account in the pattern (3.2.2) the momentum dependence on the accelerating voltage U one may obtain:

$$p = \sqrt{2meU} , \quad (3.2.3.)$$

and in consequence:

$$\lambda = \frac{h}{\sqrt{2meU}} . \quad (3.2.4.)$$

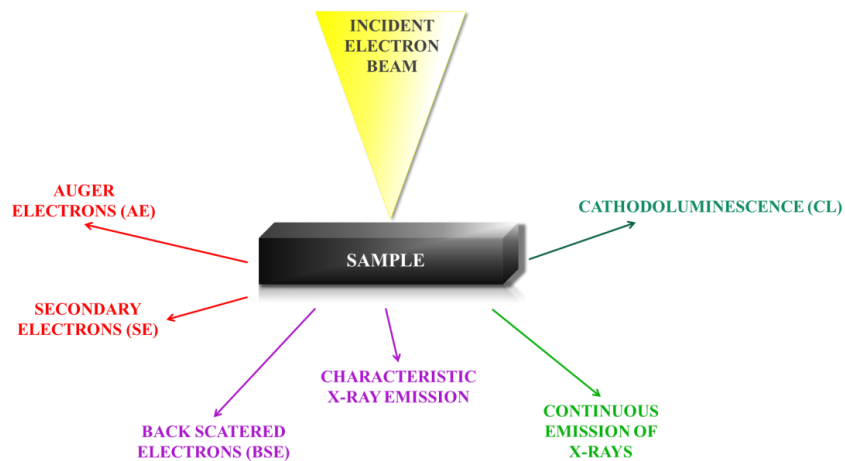
After introducing a relativistic correlation at high velocity one may get:

$$\lambda = \frac{h}{\sqrt{2m_0 eU \left(1 + \frac{eU}{2m_0 c^2} \right)}} . \quad (3.2.5.)$$

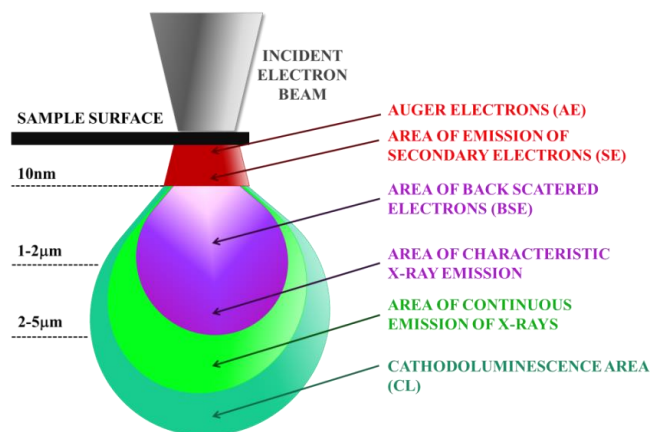
For example, for acceleration voltages of 100 and 300 kV the wavelengths equal to 3.7 and 1.97 pm, respectively are obtained. The wavelength of the electrons is 100,000 times smaller than the wavelength of light, and therefore it is possible to achieve 0.2 nm resolution in the SEM microscope. To obtain an image, electron beam formation is required. The electron beam, directed on the sample, produces various effects. Electrons colliding with atoms, loose kinetic energies and can be completely absorbed leading to radiation emissions or become "reflected" or penetrate through the material. The ratio of the numbers of "reflected", absorbed and transmitted electrons depends on the chemical composition and the thickness of the prepared sample.

Electrons incident on the sample interact with electrons of the sample and cause several emissions as secondary electrons, back scattered electrons, Auger electrons, x-rays, cathodeluminescence (**Schema 3.2.1.**).

Each type of radiation is emitted from different depth and volume of the sample. With increasing acceleration voltage the depth and volume of the emission area is increasing (**Schema 3.2.2.**). The diameter of this area is also growing with applied voltage and can reach at least several times the diameter of the beam. Additionally, the depth of electron penetration affects the atomic number of the sample components. In the SEM with tungsten thermo-emitter cathode, the electron beam diameter is approximately 2 - 5 nm and the limit of 4 -10 nm (at secondary electrons). Much better results are achieved with a field emission beam because in this case the scanning electron microscope resolution can reach 1 nm. Microscopes of this type are very expensive technologies, due to the high vacuum requirements to operate with field emission ($p < 10^{-7}$ Pa).



Schema 3.2.1. Effect of an electron beam on a sample surface



Schema 3.2.2. Range and spatial distribution of emission of different types of electrons in a sample [4,5]

The essence of SEM scanning microscopy is to scan the sample surface with an electron beam in nanometre scale. Samples are scanned by an electron beam deflected by scanning coils. The deviation of the beam forming the image on the monitor is synchronized with the deviation of the sample scanning beam. Signal from the surface of the sample, usually in the form of secondary or retrograde electrons, reaches the detector. The output from the detector controls the brightness of the image displayed on the monitor. Scanning microscope magnification is due to the ratio of the size of the scanned area of the sample. Some of the primary electrons that are scattered backwards (changing the direction of motion by more than 90 degrees due to the elastic scattering through the sample atoms) creates also backscattered electrons. The amount of emitted electrons retrograde is dependent on the atomic number Z which is the source of information on the chemical diversity of the sample. The remainder of the primary electrons, absorbed by the sample, is dispersed unevenly by the surface layers of the atoms and gradually loses energy. As a result of this interaction, the secondary electrons signal is most important in SEM. Each electron emitted by the sample possessing energy less than 50 eV is called a secondary electron. Due to low energy, only secondary electrons emitted near the surface have the chance to leave the sample and reach the detector. The amount of emitted secondary electrons gives information about the topography of the sample surface. Many of the secondary electrons leave the protuberance of the sample, while few recesses produce a topography.

The SEM is used in material and metallurgical engineering, including fractal studies, tribological wear, corrosion damage diagnosis, surface analysis of materials, chemical composition analysis and crystallographic orientation. In biology and medicine it is used for determining intracellular structures and processes, finding and recognizing chemicals, zoological research, quality control of medical procedures or defect characteristics [5,6].

In present work the JEOL, JSM 6510 LV scanning electron microscopy was used. In order to proper focus on the samples, the accelerating voltage and the variable slit size were adapted. Astigmatism and beam shape has been manually adjusted.

3.3. Atomic force microscopy (AFM)

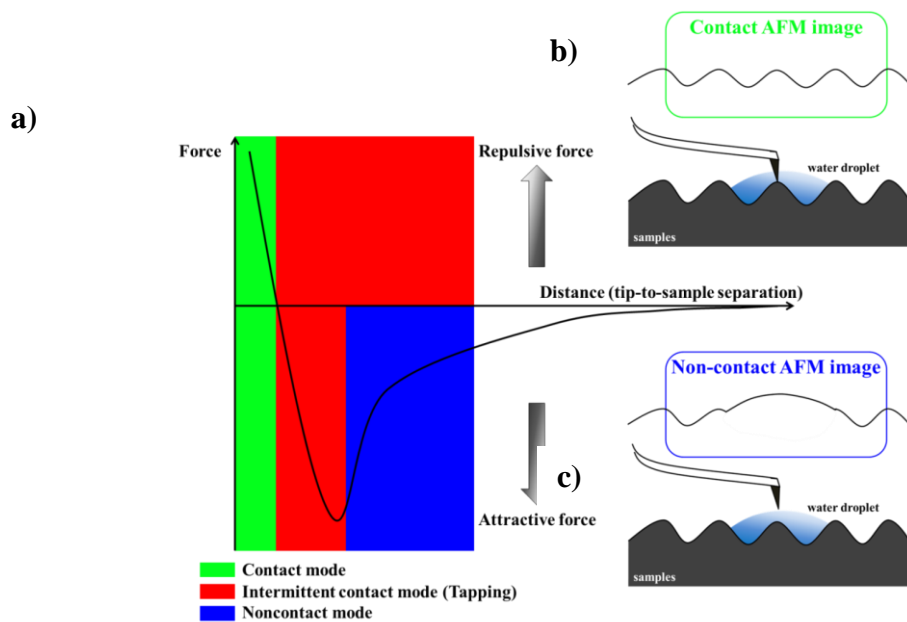
Atomic force microscope (AFM) was constructed in 1986 at IBM Lab [7] and represents today an important microscopic technique with a particular interest in nanoscience. Beyond the material morphology scanning, an environmental AFM can measure electrical or magnetic properties at the nanoscale.

Among the relevant interactions that are a source of the force acting on the AFM cantilevers, the dominant are the van der Waals attractive traction and electrostatic repulsion. The interaction between the atoms of the tip and the sample is expressed by the so-called Lennard-Jones potential:

$$V(r) = 4\varepsilon \left[\left(\frac{\sigma}{r} \right)^{12} - \left(\frac{\sigma}{r} \right)^6 \right], \quad (3.3.1.)$$

with the two parts related to the repulsion ($\sim \sigma^{12}$) and the attraction ($\sim \sigma^6$). The ε describes the depth of the potential well and σ represents the finite distance at which the intermolecular potential is zero while r is the distance between the atoms of the tip and the sample. The dependence of the Lennard-Jones potential versus the distance from the sample surface is illustrated in **Schema 3.3.1**.

The AFM probes the cantilever deflection of the lever (tipped beam) with the impact forces between the tip and the atoms forming the test surface. The bending beam is converted by a detector (photodiode) into a current signal, which then serves to generate a sample image.



Schema 3.3.1. (a) Force curve versus interatomic distance in AFM (b) contact mode (c) non-contact mode.

Therefore, unlike scanning tunnelling microscope (STM) the AFM method can be used both in conductive and non-conductive surfaces. In addition, tests can be conducted in vacuum, in air, in gases and in liquids. The theoretical resolution in z-axis is up to 0.01 nm and in x-y axis up to 0.1 nm. In fact, the resolution is generally smaller and depends on the shape of the blade, the type of material, its roughness, and the measurement conditions. Depending on the AFM mode, the attractive or repulsive forces between the measuring blade and the sample are investigated (**Schema 3.3.1.a**). The attractive forces are long-range ones which can be measured in non-contact mode (**Schema 3.3.1.b**) in contrast to repulsive forces being measured in contact mode (**Schema 3.3.1.c**).

Contact operation mode

In contact mode, the blade is in direct contact with the sample surface and the distance between the atoms of the blade and the sample is less than 1 Å. In this mode, due to the presence of repulsive forces, the beam arm is bent in the opposite direction to the sample (**Schema 3.3.1.b**). The source of repulsive forces is the interaction between electron orbital atoms on the test surface and on the surface of the blade.

In this layout, it is possible to obtain very accurate surface images, but in the case of soft materials such as polymers, the impact force should be limited to prevent the destruction of the sample. Additional pressure on the sample is caused by capillary forces (water molecules adsorbed on the surface of the sample) or electrostatic forces occurring between the charges located on the surface of the sample and the measuring edge. Therefore, in some cases, to eliminate capillary and electrostatic forces the testing is carried out in liquids. AFM microscope in contact mode can simultaneously record:

- 1) Topographic images (constant height) when constant blade pressure is maintained on the sample while the feedback loop is on. From the images you can determine the height of the surface elements, the roughness (in nm or μm units).
- 2) Image of the variable force (deflection, internal sensor) from the current measurement (beam swing) when the feedback loop is off. Images are characterized by a great resolution (detail, contrast) but cannot be measured, for example, roughness.

Non-contact operation mode

In the non-contact mode, the AFM operates in the long-range attraction and the distance of the measuring blade is equal to 1 - 10 nm. Due to the presence of gravity, the beam arm is bent towards the sample. The attractive forces are those of van der Waals between atoms at the test surface and on the surface of the blade. This method is designed to test very delicate and deformable materials, but the contaminant layer on the surface of the sample (e.g. adsorbed water) can introduce artifacts (**Schema 3.3.1.c**). This method is not suitable for fluid testing. In the non-contact method, the beam with a blade oscillates at a frequency close to the resonant frequency (100 - 400 kHz) with a few tens of nanometres. As the blade moves closer to the sample, the frequency and period of oscillation of the probe change. It serves to control the feedback loop and to produce a topographic image of the surface.

Tapping mode

In the tapping mode, the microscope operates within the distance range shown in **Schema 3.3.1.a**. During a short-term contact, the kinetic energy of the probe is dissipated and it reduces the amplitude of the vibration. These changes are recorded in the feedback system where the vibration frequency is automatically selected so that the impact force between the measuring blade and the sample is kept as low as possible. Tapping tests help to avoid damage of the sample surface by eliminating friction and adhesion forces and are especially recommended for testing easily deformable and delicate materials, both in fluids and in the air [8-10].

3.4. Kelvin probe force microscopy (KFM)

The Kelvin probe force microscopy (KFM), also called surface potential microscopy proposed by Nonnermacher in the 1991, is nanometric and atomic resolution technique. KFM represents a variant of atomic force microscopy where a metalized cantilever is capable to measure the potential difference between the nozzle contained therein and the sample surface. Through this measurement, one can obtain the characteristic work function of the sample surface which gives the exact composition at the atomic level. Through the knowledge of the work function of the sample surface, various applications are possible.

They can be correlated with the surface reconstruction, defects, or corrosion due to the working function of the atoms resulting from such phenomenon. Semiconductor, dielectrics, biological systems are able to be investigated with a molecular resolution when the topography and the surface potential can be observed.

Every atom in a solids possesses the Fermi energy defined as the energy of the electrons of the outermost atom layer, i.e. it refers to the electrons of the last occupied level. Another important concept is the work function which consists of the energy required to remove an electron from the last energetic layer of an atom leading it to the "vacuum" where it will be free of any attraction to the atom of origin. In vacuum the electron acquires an energy different from that in the material, given the absence of interactions with the solid material.

The operation of KFM is similar to atomic force microscopy where a conductive probe (cantilever) with known work function is used. The formula that will allow to obtain the work function of the sample is defined as:

$$V_{CPD} = \frac{\phi_{point} - \phi_{sample}}{-e}, \quad (3.4.1.)$$

where V_{CPD} is the contact potential difference, ϕ_{point} is the work function of the characteristic material of the tip, ϕ_{sample} is the characteristic work function of the sample and the term $(-e)$ is the charge of the electron.

Only the work function of the tip characteristic material is known, and it remains V_{CPD} and sample variables to be defined according to the procedure presented below. Initially the tip and the sample are without contact and differ by their different work functions and Fermi energies. The procedure consists of placing them very close one to the other to provoke the quantum tunnelling phenomenon consequently leading to Fermi energies. In this process, both the tip (probe) and the surface become charged because of depletion region at the interface [11]. Since the Fermi energy of the tip is smaller than that of the sample, the latter will decrease in the Fermi energy of the surface. The crucial point is to know that the working function of the electrons belonging to the sample surface does not change, since it is an inherent characteristic of the atom and thus the interval ϕ shows the difference between the energy of the electron at Fermi level and the energy of the electron in the vacuum. With equal Fermi levels, the difference in the potential between the tip and the sample will be due to the gap between the electrons in the vacuum. This is what was determined by the V_{CPD} .

The next step is to measure the V_{CPD} , where the continuous voltage source V_{DC} is applied between the nozzle and the sample. This leads to the return of the negative charges to the sample increasing its Fermi level at its initial value. The applied voltage measured and computed by the apparatus will be exactly equal to the voltage of V_{CPD} . Thus, considering the formula (3.4.1) one can obtain the work function of the atom analysed in the sample as follows:

$$V_{DC} = V_{CPD} = \frac{\phi_{point} - \phi_{sample}}{-e}, \quad (3.4.2.)$$

By rearranging the formula (3.4.2), one can get the work function of a specific point in the sample:

$$\phi_{sample} = \phi_{point} - [V_{DC} \cdot (-e)]. \quad (3.4.3.)$$

However, the previously mentioned methodology using a *DC* current is able to determine the work function of the sample only when that of the nozzle is known previously.

A more sophisticated method involves the application of simultaneous continuous and alternating voltages in order to obtain not only the work function of the sample but also the topography of the sample.

The applications of the KFM method allowed a great evolution in the study of nanostructures and sub-nanostructures as well as surfaces of semiconductors and ionic crystals investigations [11,12].

In the presented work measurements were carried out by Atomic force microscopy (AFM) and Kelvin force microscopy (KFM) with a Multimode Nanoscope 3 from Veeco.

3.5. UV-visible Spectrophotometry

Spectrophotometry in the ultraviolet (UV) and visible (Vis) range is one of the oldest instrumental methods in chemical analysis. The phenomenon of electromagnetic radiation absorption by matter has found a wide application both in particle structure studies as well as in qualitative and quantitative chemical analysis. Absorption of visible light and ultraviolet radiation depends on the structure of the molecule and that of the compound. The absorption of defined radiation causes the transition of electrons from ground states to higher energy levels - excited states.

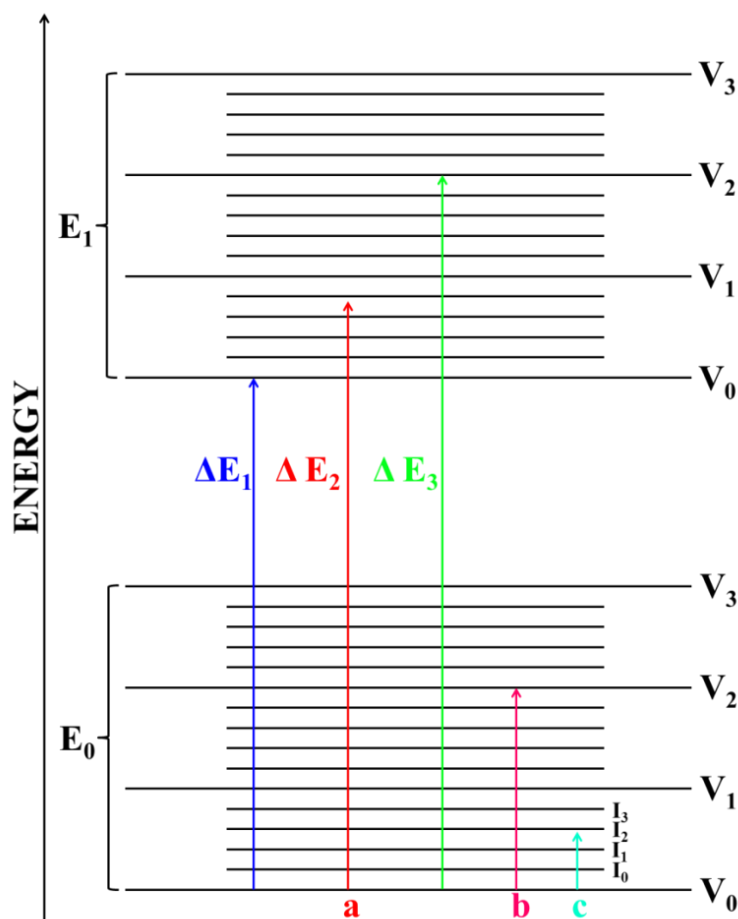
At molecular scale, the total energy E in this process can be represented as the sum of the three components related to electronic clouds, vibration and rotation motions:

$$E = E_e + E_{os} + E_{rot} . \quad (3.5.1.)$$

The electron energy in a molecule is several times greater than the vibration energy, which is greater than the rotational term. The ratios between the different energy contributions are approximately:

$$E_e : E_{os} : E_{rot} = 1000 : 10 : 1 . \quad (3.5.2.)$$

Significant differences in the values of particular types of energy cause that the spectra appear in different spectral ranges. The absorption of far-infrared and microwave concerns the rotation levels. Near-infrared radiation causes transition between vibration levels. Changes in electron energy can only cause absorption of visible and ultraviolet radiation (Schema 3.5.1.).



Schema 3.5.1. Diagram of electron, vibration and rotation transitions in a diatomic molecule. E_n are electron levels, V_n are vibration levels, I_n are rotational levels, a - illustrates electronic, b - vibration, c - rotational transitions.

The rotation, vibration, and electron energies are quantized and the required energies for transitions are formulated as follows:

- For the absorption of radiation there must be such two quantum states of molecules ψ_m and ψ_n with energy difference corresponding to the energy of incident radiation $h\nu$:

$$E_n - E_m = h\nu_{n,m} = \Delta E . \quad (3.5.3.)$$

For 1 mole of substance, ΔE will assume the value:

$$\Delta E = h\nu N_A = \frac{hcN_A}{\lambda} = \frac{1.2 \cdot 10^8}{\lambda} \text{ J/mol} . \quad (3.5.4.)$$

- The radiation absorption must be related to the change in the dipole moment μ of the molecule. In quantitative terms, this condition describes the so-called moment of transition between electron states, determining probability of incident photon absorption.

The transition moment corresponding to the electron excitation determines the probability of absorption of matched photon according to the condition:

$$R_{n,m} = \int \Psi_n \cdot \mu \cdot \Psi_m d\tau . \quad (3.5.5.)$$

The measure of the intensity of the absorption band is the molar absorption coefficient ε_{max} , at the wavelength of the absorption maximum λ_{max} . The value of ε_{max} is a measure of the transition probability which in turns is more higher for allowed than for forbidden transitions.

In a practical application, when electromagnetic radiation crosses a matter, it can be absorbed, reflected or dispersed. The intensity of the incident beam is given by:

$$I_0 = I_a + I_t + I_r , \quad (3.5.6.)$$

where I_a is intensity of radiation absorbed by the material, the I_t and I_r are related respectively to the transmitted and reflected as well as diffused light.

Since radiation absorption measurements are usually made in relation to the reference solution which composition should be similar to that of the sample and they should be in identical cuvettes, the reflected and diffused radiation I_r in both cases is identical and may be omitted. One may assume that the reference solution under the measurement conditions does not absorb radiation and the intensity of the radiation beam passing through the reference solution is equal to the intensity of the incident beam on the sample.

The ratio of the intensity of the radiation passing through the sample I_t to the intensity of radiation incident on the sample I_0 (equal to the intensity of the radiation passing through the reference), is called transmittance or permeability and is denoted as:

$$T = \frac{I_t}{I_0}. \quad (3.5.7.)$$

Transmittance is most often expressed in percentages as:

$$T = \frac{I_t}{I_0} \cdot 100\% . \quad (3.5.8.)$$

The transmittance can range from 0% to 100%.

The intensity of absorbed radiation depends on the concentration of the solution c and on the thickness of the absorbing layer l (see equation **3.5.9**) and is described by the Lambert-Beer law, which takes the logarithmic form:

$$A = \log \frac{I_0}{I_t} = kcl , \quad (3.5.9.)$$

where k is a proportionality constant (radiation absorption coefficient, often called the absorption coefficient). The decimal logarithm of the intensity ratio of the radiation beam incident on the sample I_0 to the intensity of the radiation beam passing through the sample I_t is called absorbance. It takes values from 0 to infinity.

When the concentration of the solution c is expressed in mol/dm³ and the thickness of the layer l is expressed in cm, the proportionality coefficient k is called the molar absorption coefficient ε . In consequence the **Formula 3.5.9.** takes the form:

$$A = \varepsilon lc . \quad (3.5.10.)$$

This is the basic law of absorption spectrophotometry. The relationship between absorbance and transmittance is expressed by the relation:

$$A = \log \frac{1}{T} , \quad (3.5.11.)$$

or when the transmittance is expressed in percentages:

$$A = \log \frac{100\%}{T} . \quad (3.5.12.)$$

The inverse relationship, i.e. the transmittance from absorbance is expressed by the formula:

$$T = \frac{1}{10^A}, \quad (3.5.13.)$$

and in percentage
$$T = \frac{100\%}{10^A}. \quad (3.5.14)$$

If there are several components in the test solution the spectrophotometric assay can be performed correctly when the absorbance additivity law is fulfilled, that is where the absorbance of the mixture is equal to the sum of the absorbance of the individual components. Mathematically, it is specified by the following formulas:

$$A = A_1 + A_2 + \dots + A_n = \sum_{i=1}^n A_i, \quad (3.5.16.)$$

$$A = \varepsilon_1 c_1 l + \varepsilon_2 c_2 l + \dots + \varepsilon_n c_n l = \sum_{i=1}^n \varepsilon_i c_i l, \quad (3.5.17.)$$

and for mass concentration:

$$A = a_1 \rho_1 l + a_2 \rho_2 l + \dots + a_n \rho_n l = \sum_{i=1}^n a_i \rho_i l \quad (3.5.18.)$$

The method can be used to determine the trace content and to purify the main ingredient [13-16].

In present work the thin film of monoclinic BiVO_4 and hybrids systems were investigated by using Varian Cary 500 UV-Vis- NIR spectrometer in a wavelength range from 250 nm to 1000 nm.

3.6. Raman spectroscopy

Raman spectroscopy is based on the measures of radiation scattered from vibrational modes of the explored matter. The symmetry of the molecules or that of crystalline structure determines which vibrations are active in the Raman spectrum. This criterion is expressed by the selection rules that determine the probability of observing intensity of a given band. According to the selection rules of Raman spectroscopy only the vibrations are seen in which the molecule polarization is changed:

$$\left(\frac{\partial \alpha}{\partial Q}\right)_{Q=0} \neq 0. \quad (3.6.1.)$$

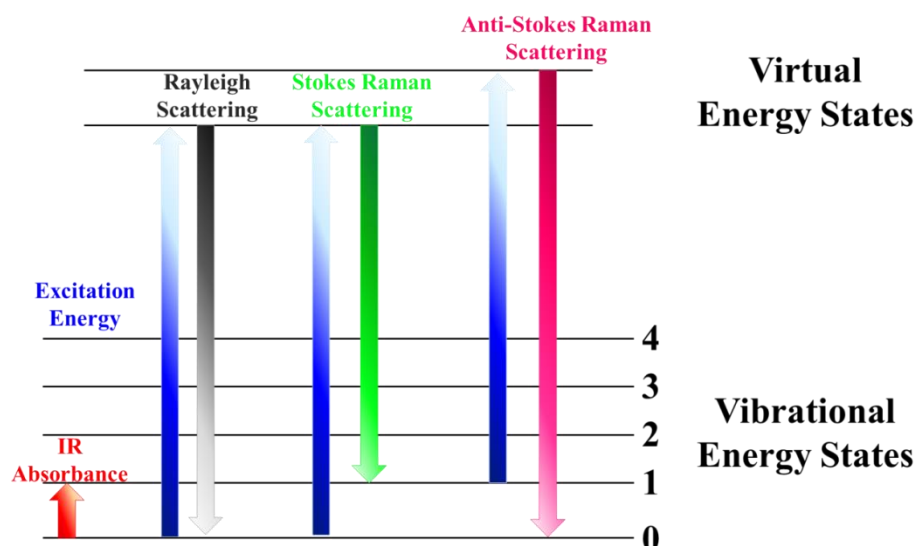
The polarization possesses a tensor representation and can be presented as an ellipsoid of polarization. When the electrical field interaction is uniform in all directions of the sample its polarization is isotropic. When the polarizability α is represented by an ellipsoid depending on the space orientation the polarization is anisotropic.

An intensity of the Raman spectra are related to the polarization of the network and can be described by the function:

$$I = f(\nu^4) \quad (3.6.2.)$$

where I (intensity of diffused radiation) is proportional to the fourth power of a radiation frequency ν . In the Raman spectra, the intensity of the radiation I exiting the sample is a linear function of the molar concentration and thickness of the layer, whereas in the IR spectrum this relation is exponential. Types of bands observed in the Raman spectra are presented in **Schema 3.6.1.** and they are as follows:

- *Rayleigh bands*: generated by the incident radiation at frequencies ν_0 , which does not match the energy levels of the molecule.
As the molecule after radiation exposure returns to the same energy level, this phenomenon is reduced to the classical Rayleigh diffusion.
- *Stokes bands*: when the molecule after exposure to radiation undergoes a transition to a higher vibration level and then to relax a photon is emitted losing its energy. When the emitted photon has less energy than the absorbed photon, this energy difference is the Stokes shift.
- *Anti-Stroke bands* - before being exposed to radiation the molecule was at a higher vibration level, the return to fundamental vibration level is accompanied by energy release. The energy of the diffused photon is greater than the incident beam. The anti-Stokes band appears in the Raman spectra at the opposite side compared to the Stokes band.



Schema 3.6.1. Diagram of energy presenting different types of scattering

In order to obtain appropriate Raman spectra, the test substance should be optically homogeneous, opaque, colourless, non-fluorinated. Quantities of substances needed for testing are of the order of one milligram [17-19]. In present work the vibrational properties are investigated by using a confocal micro-Raman spectrometer. The excitation was realized with a 514.5 nm laser radiation with 150 mW power. With regard to the large spectral range on which the spectra are recorded an appropriate calibration of the CCD detection system was realized.

3.7. Photocatalytic test

Photocatalytic reactions based on the radiation inducing decomposition of organic dyes are model systems to evaluate the photocatalytic properties of semiconducting oxides. In heterogeneous photocatalysis, the semiconductor is surrounded by an environment such as solution with dyes. The best mechanism for describing this phenomenon is the Langmuir-Hinshelwood model. Its mechanism assumes that the absorption of radiation by the photocatalyst leads to the generation of free electrons and holes, known under the common name of the excitons. The life time of the excitons is extremely short (about 30 ns in TiO₂ [20]) and can lead easily to recombination phenomena which cancel the electron-hole pairs. With suitable lifetime, electrons and holes may have enough time to migrate to the surface of the photocatalyst where they may generate radicals at the interface with the surrounding media.

The active radicals (superoxide and hydroxyl) are able to decompose organic molecules into a products with small and inactive molecules (CO₂, H₂O).

The **Equations 3.7.1.-3.7.6.** demonstrate the mechanism of the active radicals creations and degradation of organic pollutants.

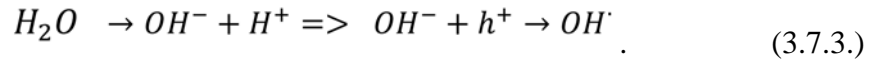
Under the influence of the incident radiation on the semiconducting photocatalyst (PC), a hole-electron pairs ($h^+ + e^-$) are created:



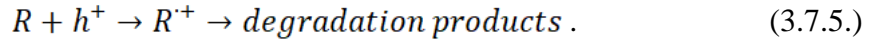
Then a production of the superoxide radicals from oxygen molecules adsorbed on the surface of photocatalyst occurs:



As a result of the interaction between water molecules adsorbed on the PC surface and holes from the valence band the active hydroxyl radicals are formed [21]:



Created hydroxyl radicals and the holes from valence band interact with organic molecules (R) causing their excitation and in consequence their decomposition into simple inorganic compounds:



The carbonyl group react with the holes from PC decomposing organic molecules into volatile, inorganic CO₂ as follows [22]:



The expression describing the rate of organic compounds degradation is as follows:

$$v = k\theta = \frac{kKc}{1+Kc} , \quad (3.7.7.)$$

where k is reaction rate constant, θ shows degree of coverage and K is adsorption constant, c is concentration of the organic substance in solution.

In the case that substrate level is small, e.g. when reacted in dilute solutions or gas phase containing small amounts of substrate, Kc value $\ll 1$. Therefore **Equation 3.7.7.** can be written as:

$$v = -\frac{dc}{dt} = k_r c, \quad (3.7.8.)$$

where, k_r is the apparent rate of pseudo first order velocity.

By integrating **Equation 3.7.8.** in terms of the change of concentrations from c_0 to c and $t_0=0$ one can obtain the following relation [23]:

$$\ln \frac{c_0}{c} = k_r t, \quad (3.7.9.)$$

where in general, the value of k_r refers to the weight of the catalyst and this parameter is used to express the activity of the photocatalyst [24,25].

Wu reports [26] that the concentration of the organic dye in the solution may have a significant effect on the efficiency of the photoactive process. It has been proven that an increase in the concentration of the organic compound can cause radiation shielding effect and in consequence less photons may reach the surface of the photocatalyst [26].

One of the most commonly used organic dyes in photocatalysis is methylene blue. Houas and co-workers have been confirmed that methylene blue on the surface of TiO_2 decomposed to the NH_4^+ , CO_2 , SO_4^{2-} or NO_3^- [22]. The OH radicals involved in the reaction are likely to attack the $C - S^+ = C$ groups present in one of the resonant structures of the methylene blue molecule that interact with the cobalt forces with the TiO_2 surface. The next step is cleavage of $C - S^+ = C$ groups that initiates the opening of the central aromatic ring with the heteroatoms S and N.

The next two attacks of the hydroxyl radical lead to the cleavage of the two benzene rings and the formation of the sulfonic acid ($R - C_6H_4 - SO_3H$). The subsequent attack of the radical results in SO_4^{2-} and the radical $R - C_6H_4$, which may react with another hydroxyl radical to give the phenolic product. Similarly, $N = C$ bonds occur in the methylene blue structure, and NH_4^+ and NO_3^- [22,27].

Studies on the effect of the addition of oxidants in the dye degradation process confirm that H_2O_2 and $S_2O_8^{2-}$ ions also act as electron acceptors in this case, slowing the electron-hole recombination process. In addition, to prevent electron-hole recombination by electron capture from the conductivity band, these substances participate in the formation of additional hydroxyl radicals and other reactive chemical species such as SO_4^{2-} sulfate radicals [28,29].

In present work the photocatalytic properties of the BiVO₄ thin films were investigated through the degradation of organic dye molecules under irradiation coming from 60 W Xe lamp. The container consist in a glass beaker of 100 ml cylindrical reactor. The aqueous solution was charged with dyes (10⁻⁵ M) and containing BiVO₄ film set at 30 cm from the radiation source was located. This leads to a radiation power density on the photoactive film about 4 W/cm². The process of methylene blue degradation was conducted at the room temperature. The kinetics was recorded each 30 min through the optical absorbance C_t of the solution charged with dyes. The photocatalytic efficiency of the thin film of monoclinic bismuth vanadate was calculated from the change of the C_t/C_0 ratio in time.

3.8. References

- [1] Z. Bojarski, M. Gigla, K. Stróż, M. Surowiec, *Krystalografia, Wydawnictwo Naukowe PWN, Warszawa, 3, 2007*
- [2] C. Kittel, *Wstęp do fizyki ciała stałego, Wydawnictwo Naukowe PWN, Warszawa 1976*
- [3] A. Guinier, *X-Ray Diffraction in Crystals, imperfect crystals and amorphous Bodies, W. H. Freeman and company, San Francisco and London, 1963*
- [4] P.J. Goodhew, J. Humphreys, R. Beanland, *Electron Microscopy and Analysis, Taylor & Francis, 2001*
- [5] A. Barbacki, *Mikroskopia elektronowa, Wydawnictwo Politechniki Poznańskiej, Poznań 2007*
- [6] A. Łasińska: *Skaningowa mikroskopia elektronowa w badaniach kryminalistycznych, Materiały szkoleniowe, Prokuratura i Prawo, 2013*
- [7] G. Binnig, C.F. Quate, C. Gerber, *Phys. Rev. Lett.* 1986, 56, 930-933
- [8] T. Kruk, *Mikroskopia Sił Atomowych (AFM), Nanonauka* 2014, 18, 1, 46-50
- [9] E. Meyer, *Atomic Force Microscopy, Progress in Surface Science, Pergamon Press Ltd.* 1992, 41, 3-49,
- [10] K. S. Birdi, *Scanning Probe Microscopes: Applications in Science and Technology, CRC Press* 2003
- [11] W. Melitz, J. Shena, A.C. Kummel, S. Lee, *Kelvin probe force microscopy and its application, Surface Science Reports* 2011, 66, 1–27

- [12] T. Wagner, High-resolution Kelvin probe force microscopy of active nanoelectronic devices, *ETH Zurich Research Collection* 2016, 23290
- [13] T. Owen, Fundamentals of modern UV-visible spectroscopy, *Agilent Technologies* 2000
- [14] B. M. Tissue, Ultraviolet And Visible Absorption Spectroscopy, *John Wiley & Sons Inc.* 2012, 1-13
- [15] I. Żak, Chemia medyczna/Analiza instrumentalna, *Śląska Akademia Medyczna*, Katowice 2001
- [16] G. Gauglitz, T. Vo-Dinh, Handbook of Spectroscopy, *WILEY-VCH Verlag GmbH & Co. KGaA*, Weinheim 2003
- [17] J.R. Ferraro, K. Nakamoto, C.W. Brown, Introductory Raman Spectroscopy, *Elsevier* 2003
- [18] E. Smith, G. Dent, Modern Raman Spectroscopy – A Practical Approach, *Wiley & Sons Ltd*, England 2005
- [19] R.L. McCreery, Raman Spectroscopy for Chemical Analysis, *John Wiley & Sons Inc.*, Canada 2000
- [20] G. Rothenberger, J. Moser, M. Gratzel, N. Serpone, D. K. Sharma, Charge Carrier Trapping and Recombination Dynamics in Small Semiconductor Particles, *J. Am. Chem. Soc.* 1985, 107, 26, 8054–8059.
- [21] P. Pichat, Y. Nosaka, A. Y. Nosaka, Photocatalysis and Water Purification From Fundamentals to Recent Applications, *Wiley-VCH Verlag GmbH & Co. KgaA*, Germany, 2013
- [22] A. Houas, H. Lachheb, M. Ksibi, E. Elaloui, C. Guillard, J.-M. Herrmann, Photocatalytic degradation pathway of methylene blue in water, *Applied Catalysis B: Environmental* 2001, 31, 145–157
- [23] N. Barka, S. Qourzal, A. Assabane, A. Nounah, Y. Ait-Ichou, Photocatalytic degradation of an azo reactive dye, Reactive Yellow 84, in water using an industrial titanium dioxide coated media, *Arabian Journal of Chemistry* 2010, 3, 279–283

- [24] A. Fernhdez, G. Lassaletta, V.M. Jimknez, A. Justo, A.R. GonzSlez-Elipe, J.-M. Herrmann, H. Tahiri, Y. Ait-Ichou, Preparation and characterization of TiO₂ photocatalysts supported on various rigid supports (glass, quartz and stainless steel). Comparative studies of photocatalytic activity in water purification, *Applied Catalysis B: Environmental* 1995, 7, 49-63
- [25] M.A. Rauf, M.A. Meetani, S. Hisaindee, An overview on the photocatalytic degradation of azo dye in the presence of TiO₂ doped with selective transition metals, *Desalination* 2011, 276, 1-3, 13-27
- [26] C.H. Wu, Effects of operational parameters on the decolorization of C.I. Reactive Red 198 in UV/TiO₂-based systems, *Dyes and Pigments* 2008, 77, 31-38
- [27] H. Lachheb, E. Puzenat, A. Houas, M. Ksibi, E. Elaloui, Chantal Guillard, Jean-Marie Herrmann, Photocatalytic degradation of various types of dyes (Alizarin S, Crocein Orange G, Methyl Red, Congo Red, Methylene Blue) in water by UV-irradiated titania, *Applied Catalysis B: Environmental* 2002, 39, 1, 75-90
- [28] C.-H. Yua, C.-H. Wub, T.-H. Ho, P.K. A. Hong, Decolorization of C.I. Reactive Black 5 in UV/TiO₂, UV/oxidant and UV/TiO₂/oxidant systems: A comparative study, *The Chemical Engineering Journal* 2010, 158, 3, 578-583
- [29] M. Muruganandham, M. Swaminathan, Photocatalytic decolourisation and degradation of Reactive Orange 4 by TiO₂-UV process, *Dyes and Pigments* 2006, 68 , 133-142

Thesis and Hypothesis

The main goal of the Thesis is a synthesis and physic-chemical analysis of the sensitized mesoporous materials based on bismuth vanadate (BiVO_4) as well as confirmation of their photocatalytic properties. In this case have been specified hypothesis as following:

1. Mesoporous structure of the BiVO_4 increases its photocatalytic efficiency.
2. The organic dyes attached to the surface of the thin film of mesoporous BiVO_4 increase the photocatalytic properties of bismuth vanadate based hybrid systems.

Chapter 4

Physico-chemistry of BiVO₄

Bismuth vanadate can be synthesised using different methods such as sol-gel, hydrothermal method, RF-sputtering, ball milling, etc. Depending on the considered method, the morphology and structural properties of the obtained material can be modulated in large extent. The objective of the present chapter is to highlight the main features of the synthesis methods to obtain BiVO₄ with defined microstructure organization. It will focus on an experimental approaches developed to obtain pristine BiVO₄ with mesoporous morphology as well as to synthesize the hybrid BiVO₄ sensitized by selected organic dyes. The samples which production is described in the present chapter were used to perform all experimental investigations presented and analysed in Chapter 5.

4.1. Synthesis of the mesoporous BiVO₄

The goal of the present work is a synthesis of the mesoporous material based on BiVO₄ exhibiting large available contact surfaces with external environment. In this case two *Solutions A* and *B* were prepared and mixed together under the stirring. To prepare the *Solution A*, first of all, the 0,5 mmol (0.058 g) of the NH₄VO₃ with 9 ml of 1-propanol were used. Under continuous stirring, the 0,5 ml of HNO₃ (65%) drop by drop during 3 minutes was added. As a result, the solution turned to a yellow color. Then, the mixture was kept during 30 min at room temperature under continuous stirring. Next, ultrasonic bath was used during 5 minutes followed by adding 0,5 mmol (0.096g) of citric acid with stirring until dissolution. To prepare *Solution B* the 0.5 mmol (0.2425g) of Bi(NO₃)₃·5H₂O was dissolved with 0.5 ml of acetic acid.

In a final stage, *Solution A* was mixed with *Solution B*, stirred 30 minutes and then the surfactant was added. Depending on the surfactant nature, two solutions were prepared. One called the *solution I* containing 0.09 mmol (0.55 g) of the P123 and the second labeled *solution II* made by using 0.024 mmol (0.3 g) of the F127.

Preparation of substrate

Borofloat glasses were cut in pieces with size $20 \times 20 \text{ mm}^2$ and cleaned by using ethanol under ultrasonification during 10 min. Subsequently, additional surface treatment was carried out by immersing borofloat substrates in 0.01 mol/dm^3 solution of the HCl for 3 minutes to remove eventual impurities being unaltered by ethanol. The next step was the immersion of the substrates in 0.01 mol/dm^3 solution of the NaOH for 3 min in order to realize HCl neutralization. Finally, the substrates were removed from the NaOH solution and washed vigorously with distilled water. Thus, all residues and impurities were correctly removed from the substrates. All substrates were dried using clean compressed air and were used immediately, or up to 3h after being cleaned.

Preparation of thin films

A single layer of the synthesized *solution I* or *solution II*, respectively was deposited on the borofloat substrate using dip coating method. The deposition parameters were selected in preliminary test measurements. The speed of substrate displacement was chosen to be equal to $0,05 \text{ cm/s}$ and room temperature was kept for all realized films. The samples were first dried in the furnace at 80°C during 12 hours. In the last stage, the films were annealed from room temperature (RT) up to 300°C with rate 2°C/min . Then the film was annealed with higher rate equal to 5°C/min up to 450°C . After that the sample was kept 2h at the temperature 450°C and then cooled up to 40°C with rate 5°C/min . The procedure is illustrated in the schema **Fig. 4.1.1**.

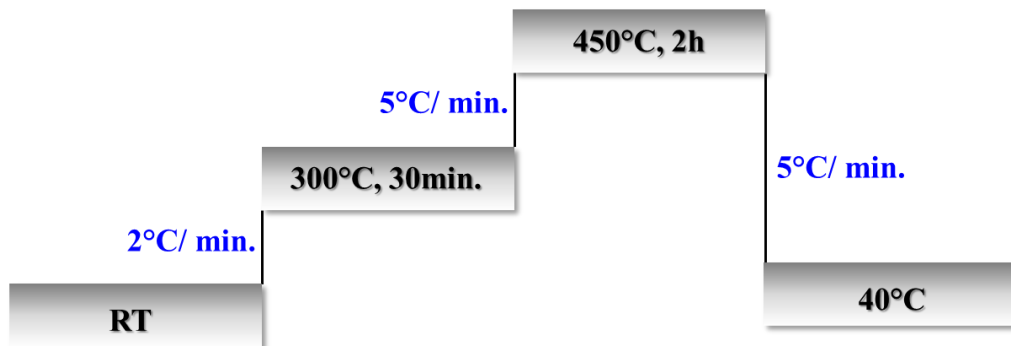


Figure 4.1.1. Annealing process applied during the thin film preparation of the BiVO_4

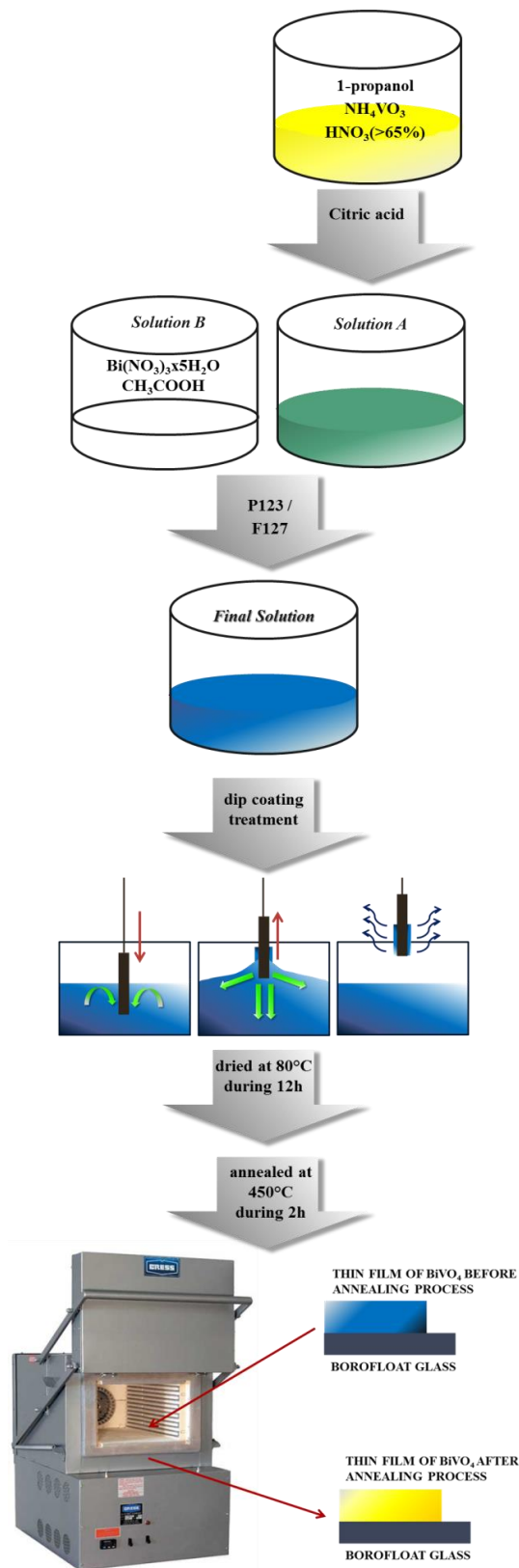


Figure 4.1.2. Diagram of production of thin layers of BiVO_4 deposited by dip coating on borofloat substrate

The complete process of the mesoporous BiVO₄ thin film production is presented schematically in **Fig. 4.1.2**. The prepared films were investigated by different physico-chemical methods to characterize deeply their physical features. By the methodologies described in Chapter 3 their structure, composition, morphologies as well as the electronic optical and photocatalytic properties were investigated and the obtained results are described in Chapter 5.

4.2. Hybrid composites based on mesoporous BiVO₄ with anchored dyes

The 5-[[4-[4-(2,2-Diphenylethenyl)phenyl]-1,2,3-3a,4,8b-hexahydrocyclopent[b]indol-7-yl]methylene]-2-(3-ethyl-4-oxo-2-thioxo-5-thiazolidinylidene)-4-oxo-3-thiazolidineacetic acid (D149) was purchased from Sigma-Aldrich and used as received to sensitize the BiVO₄ mesoporous structures. The other two molecules as the N, N-dimethyl-4-((E)-(pyridin-2ylmethylene) amino)phenyl diazenyl) aniline (LIGAND) and the N,N-dimethyl-4-((E)-(pyridin-2ylmethylene) amino)phenyl diazenyl) aniline Zinc Chloride (COMPLEX) [1] synthesized in the Laboratoire MOLTECH-Anjou, University in Angers (France) where used as a dyes anchored at a surface of the BiVO₄. All other chemicals as the tert-butanol or acetonitrile used with BiVO₄ samples were purchased from commercial company (Merck, Sigma-Aldrich) and used without further purification.

Preparation of organic dye solution:

A 3.34 mg of the D149, 4.8 mg of the LIGAND or 1mg of the COMPLEX were placed in a dark container. Next, the dyes were added to 7.5 ml of the acetonitrile and 7.5 ml of the tert-butanol. The solution was submitted to ultrasonification in water for 10 sec. and was heated at 66°C for 30 min to completely dissolve the organic dye powders. After completing the dissolution process, the solutions were cooled to RT. To prevent the problem of solution aging, all solutions were used directly, or up to 3h after being prepared.

Preparation of hybrid photoactive systems based on the BiVO₄ thin film sensitized by organic dye:

The annealed thin films (as is presented in **Fig. 4.1.1.**) were immersed in 0.3 mmol/dm³ ($4.5 \cdot 10^{-3}$ mmol of organic dye) dye solutions. This immersion is made at room temperature during 4h. Its aim is to allow efficient adsorption of dyes on the available inorganic surface of the BiVO₄. In consequence the dyes coated the BiVO₄ media creating the hybrid system used for the physico-chemical analysis described in Chapter 5. Finally, the hybrid composite films were dried at RT for 12h on air.

Exhaustive characterizations were carried out on hybrid systems in order to analyze their photocatalytic properties and in consequence to define their electronic charge transfer properties and the optical features of the inorganic/organic films.

4.3. Reference

- [1] I. Guezguez, A. Ayadi, K. Ordon, K. Iliopoulos, D.G. Branzea, A. Migalska-Zalas, M. Makowska-Janusik, A. ElGhayoury, B. Sahraoui, Zinc Induced a Dramatic Enhancement of the Non Linear Optical Properties of an Azo-based Iminopyridine Ligand, *J. Phys. Chem. C* 2014, 118, 14, 7545–7553

Chapter 5

Results and discussion

5.1. Quantum-chemical calculations and experimental investigations of the BiVO₄ in bulk and nanosized form

5.1.1. Electronic and structural properties

Theoretical investigations

Using the Materials Studio program package [1], the monoclinic scheelite BiVO₄ single crystal structure was built. The mentioned structure was constructed according to the data given by Zhao [2]. The base centered monoclinic crystal architecture belongs to space group C2/C and point group C_{2h}^6 . The unit cell parameters are as follow $a = 7.247 \text{ \AA}$, $b = 11.697 \text{ \AA}$, $c = 5.090 \text{ \AA}$ and $\gamma = 134.226^\circ$ with fractional atomic coordinates of Bi (0.000, 0.134, 0.750), V (0.000, 0.370, 0.250), O1 (0.261, 0.051, 0.380) and O2 (0.354, 0.208, 0.861).

The electronic properties of the monoclinic scheelite BiVO₄ single crystal were calculated using the CASTEP program [3,4] with implemented total energy plane-wave pseudopotential method. The electronic exchange-correlation energy was treated within the framework of the generalized gradient approximation (GGA) using Perdew-Burke-Ernzerhof (PBE) potential [5]. The Monkhorst-Pack k -points grid sampling was set at $5 \times 5 \times 7$ points for the Brillouin zone [6]. The plane-wave basis set cut-off was chosen to be equal to 350 eV. The total energy was considered to be converged when the self-consistent field (SCF) tolerance was equal to 10^{-6} eV/atom. The ultra-soft pseudopotential was used to perform calculations for Bi $6s^2 6p^3$, V $3s^2 3p^6 3d^3 4s^2$ and O $2s^2 2p^4$ electrons [7].

The standard procedure before electron properties calculations is the geometry optimization of the molecular structure. In the presented work the mentioned standard geometry optimization procedure was performed as well as the electronic properties of the BiVO₄ were calculated for the frozen structure with parameters obtained from the X-ray diffraction experiments. In this case, the work presents two approaches. One is taking into essential calculations the BiVO₄ single crystal with geometry optimized structure (relaxed structure) and the second one without optimization (frozen structure). During geometry optimization procedure the lattice parameters of the BiVO₄ structure and its atomic coordinates were relaxed by minimizing the total energy using the DFT/PBE potential. The Broyden–Fletcher–Goldfarb–Shanno (BFGS) schema was used for the minimization algorithm [8]. The convergence parameters were chosen for the energy as low as 2×10^{-5} eV per atom, force on the atom was less than $0.01 \text{ eV}\text{\AA}^{-1}$, stress on the atom was less than 0.02 GPa and atomic displacement was below $5 \times 10^{-4} \text{ \AA}$. **Table 5.1.1.1.** reports the parameters of the unit cell and the length of the bonds for the relaxed and frozen structure.

Table 5.1.1.1. Lengths of the Bi-O and V-O bonds as well as lattice parameters for the frozen and relaxed structure of BiVO₄ single crystal

Parameters	Frozen structure	Optimised structure
Bi-O bond length [\AA]	2.352 \AA 2.372 \AA 2.518 \AA	2.495 \AA 2.455 \AA 2.437 \AA
V-O bond length [\AA]	1.762 \AA 1.688 \AA	1.740 \AA 1.744 \AA
Lattice parameters	$a = 7.247 \text{ \AA}$ $b = 11.697 \text{ \AA}$ $c = 5.090 \text{ \AA}$ $\gamma = 134.226^\circ$	$a = 7.330 \text{ \AA}$ $b = 11.649 \text{ \AA}$ $c = 5.1932 \text{ \AA}$ $\gamma = 135.446^\circ$

After the geometry optimization procedure, the shortest lattice parameters (a and c) of the BiVO₄ single crystal increase and the longest one (b) decreases. Also the interatomic distances were modified. The geometry optimization procedure revealed that the Bi–O bond lengths have a tendency to be symmetrical. The same situation is observed for V–O bonds. The possible reason for such isotropic bond lengths arrangement in the case of Bi–O connection is due to the strong correlation between the Bi 6s and the O 2p orbitals [9].

As a consequence of the structure relaxation, the local environments around Bi and V atoms undergo a more symmetrical organization.

The changes in the interatomic distances obtained by the geometry optimization, affect the electronic properties of the BiVO₄ structure. In order to prove this hypothesis, the electron energy dispersion diagram in the Brillouin zone was calculated. The energy dispersion curves of occupied and unoccupied states exhibit a similar behavior for the optimized and frozen structures (**Fig. 5.1.1.1**). It means that shape of the energy levels evaluation is similar for the both optimized and for frozen structure as well. Nevertheless, the energy gap for the optimized structure is less by 0.24 eV compared to that of the frozen structure. The obtained results for the optimized structure are consistent with the data published by Zhao et al. [10], where the band gap of the BiVO₄ was evaluated theoretically using the GGA/PBE functional and was obtained to be equal to 2.17 eV. For the frozen structure, its energy gap was evaluated to 2.41 eV and is in agreement with the experimental reports [10,11]. As it was mentioned before the shapes of the energy dispersion curves in both structures are similar. In this case, the optimized and frozen structures possess an indirect band gap (**Fig.5.1.1.1**, see red arrow). It was confirmed by the experimental results reported by Venkatesan et al. and Cooper et al. [12,13].

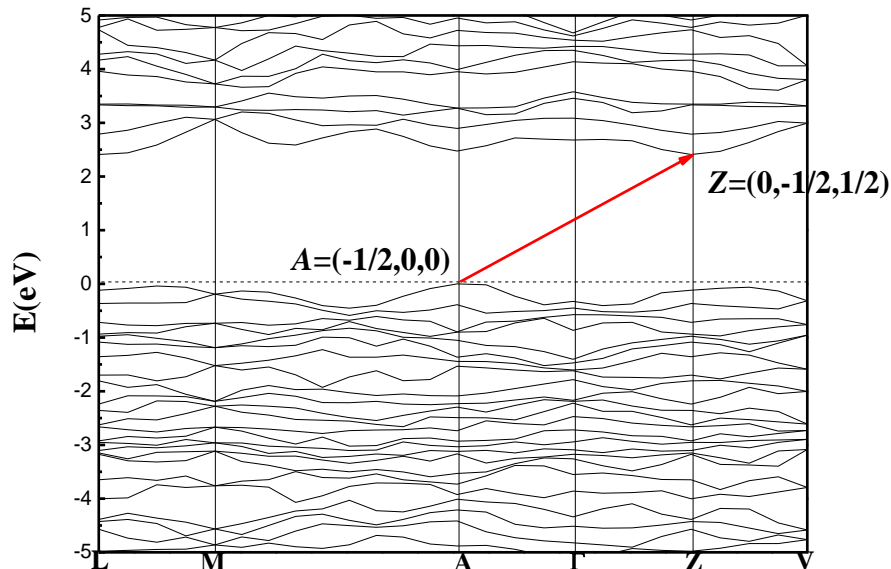


Figure 5.1.1.1. Electron energy structure calculated by DFT/PBE methodology of monoclinic frozen BiVO₄ structure

Consequently, it was decided to focus attention on a structure closer to the real one, i.e. without optimized geometry. The simulated energy band structure for the frozen BiVO₄ single crystal leads to the effective masses of the charge carriers calculations.

The effective mass of an electrons m_e^* can be evaluated from the curvature (energy derivatives) of the bottom of conduction band in the k space. The diagonal elements of the effective mass tensor for electrons is calculated around the Z (0,-0.5,0.5) point of the BZ and the effective mass tensor for holes is calculated around A (-0.5, 0, 0) point of the BZ following the equation:

$$\frac{1}{m_{e_{ij}}^*} = \frac{1}{\hbar^2} \frac{\partial^2 E(k)}{\partial k_i \partial k_j} . \quad (5.1.1.1)$$

The effective mass of electrons is determined by fitting the conducting band structure to a parabolic function. The energy dispersion curves of valence band maximum (VBM) and conducting band minimum (CBM) are symmetrical around the A and Z points of the BZ, respectively (**Fig. 5.1.1.1**). In this case the calculated electron and hole effective masses are equal to $m_e^* = 0.5050m_e$ and $m_h^* = 0.4525m_e$, respectively. These data are in good agreement with the experimental results presented by Hung and coauthors [14] and Zhao and coauthors [10,15]. In semiconducting oxides, the valence band formed by localized oxygen p orbitals leads to an increase in the effective mass of the holes. As the valence band of the BiVO₄ is hybridized by the O 2p and Bi 6s electrons, a strong correlation between them causes a decrease in the effective mass of the holes and an increase in their mobility. Such a light mass of holes is expected to facilitate efficient photoinduced charge separation and mobility, suggesting a possibility of high quantum efficiency in photocatalysis. This allows to conclude that the charge carriers as electrons and holes in the same time can migrate to the surface of the photocatalyst and then participate in redox formation of radicals. This means that more active forms of superoxide and hydroxyl radicals are formed and contribute to efficient photocatalytic reactions.

In **Fig. 5.1.1.2**. a partial electron density of states (PDOS) is presented. The significant differences between frozen and relaxed structure are mainly visible in the valence bands. The top of the valence band calculated for relaxed structure is built by hybridization of the O 2p and V 3p electron states giving the impact in the reduction of the electronic band gap.

The minimum of the conduction band obtained for this structure is dominated by V 3d states with small contributions from the Bi 6p and O 2p orbitals. In contrast to the above mentioned data the main contributions to the valence band states of the frozen BiVO₄ crystal structure comes from the O 2p orbitals slightly hybridized with Bi 6s states.

The bottom of the conduction band calculated for the BiVO₄ crystal structure is formed by the V 3d states. Usually, the valence band in metal oxides is derived from the O 2p orbitals and the conduction band is built by metal s or d orbitals. However, in monoclinic BiVO₄, the valence band contains hybrid O 2p and Bi 6s orbitals, which causes an upward dispersion of the electronic structure at the Brillouin zone boundary [16]. This indicates that the frozen structure allows sound analysis of the electronic features of the BiVO₄ crystal. The distortions of Bi–O and V–O bond lengths during geometry optimization enhance the impact of the V 3p electronic states in the valence band and lower the contribution of the V 3d states in the conduction band. It contributes to a more significant dispersion in the valence band of the BiVO₄ crystal. These results are in agreement with the data measured by using the XPS method [17]. The obtained results suggest that, from a computational point of view, both structures – optimized and frozen – lead to coherent outcomes. The obtained data make it possible to infer that modeled nanosized clusters should be constructed with protection of the crystal internal structure (interior) and with optimized external atomic shells (exterior), according to the surface effects and environmental interactions.

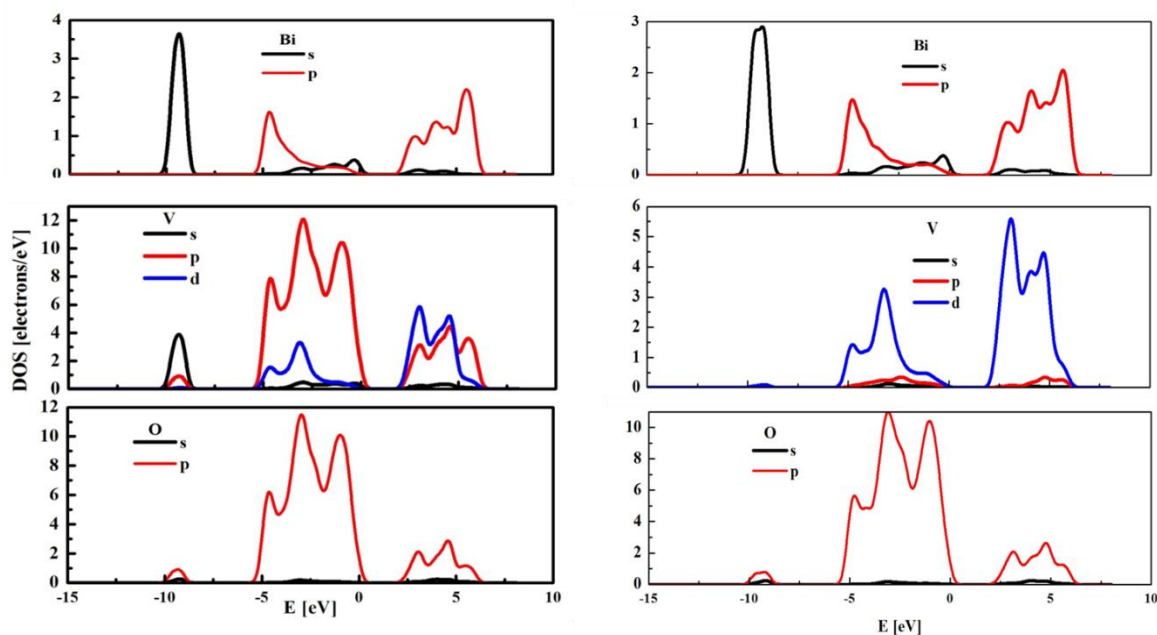


Figure 5.1.1.2. The PDOS calculated by DFT/PBE method for relaxed (left panel) and frozen BiVO₄ structure

Analyzing the PDOS one may conclude that the transmission of the photogenerated electrons occurs between the hybridized O 2p and Bi 6s orbitals and the V 3d orbitals for the frozen structure whereas for the relaxed structure the electron excitation is between hybridized O 2p and V 3p electronic states and the V 3d electronic state. The transition between the different orbitals of the same atom is not a typical phenomenon for semiconductors. In this case the frozen structure makes it possible to more accurately reflect the actual electronic relationships in BiVO₄. Therefore, later in the work, the frozen structure will serve as a benchmark for analyzing the properties of nanocrystals.

According to the literature data, the size of the BiVO₄ crystallites affects the photocatalytic activity. It has been shown that nanostructures exhibit better photocatalytic properties than the bulk materials [18] however this phenomenon is not fully explained. Quantum chemical calculations may be helpful in this case. Consequently, theoretical studies on the electronic, optical and vibrational properties of bismuth vanadate nanocrystals have been carried out. The general advantage of nanostructured systems is related to their high surface areas, which increase the efficiency of photocatalytic reactions.

Nanoclusters with a spherical shape composed by n units of the (BiVO₄) and referred below as the (BiVO₄) _{n} were built using Materials Studio software. **Fig. 5.1.1.3** reports an example of the constructed (BiVO₄) _{n} nanocrystal. The clusters were built with the monoclinic BiVO₄ crystal structure reducing the external atoms to obtain spherical cluster with defined size and total number of the (BiVO₄) _{n} units. The number n of the structural units was changed from $n = 1$ up to $n = 56$, leading to a cluster diameter up to 2.0 nm.

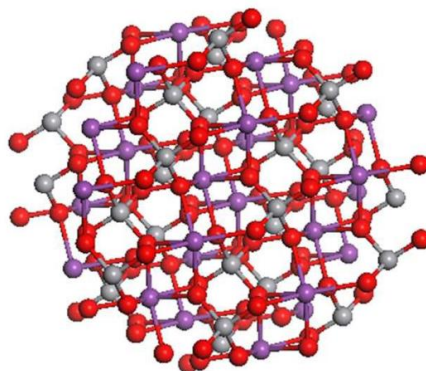


Figure 5.1.1.3 Structure of the (BiVO₄)₂₆ nanocrystal with size 1.3 nm projected along [010] crystallographic direction

The calculations of electronic properties performed for nanocrystals, require the use of two methodologies based on a semi-empirical approach and DFT methodology. The two mentioned methods were used, because it is necessary to ensure the stability of the performed simulations. The semi-empirical approach with the parameterized PM6 method [19] allows a pertinent evaluation of the physical features of clusters with large sizes and with the involvement of heavy atoms. Within such a framework, the numerical simulations were performed using the Gaussian quantum-chemical program package [20]. All the calculations were made using restricted Hartree–Fock (RHF) regime with the SCF convergence criterion set at 10^{-5} hartree. The second approach was based on DFT calculations with Gaussian and DMol3 [21,22] programs. The calculations were performed using the PBE [23] and B3LYP [24] functionals with applying the DND and CEP-4G basis sets. No symmetry rules were imposed during the electronic structure analysis. The SCF density convergence criterion was equal to 10^{-8} hartree. In order to reduce the required computational time, all the core electrons were represented by the effective core pseudopotential [25]. With regard to the size of the investigated clusters, the single point calculations were performed applying the RHF method.

The electronic properties of the generated nanocrystals were calculated applying the cluster approach without any saturation at their surface [26]. According to the work of Makowska-Janusik et al. [26], performed for other classes of nanocrystalline oxide systems, dangling bonds were not considered. The physical properties of the investigated $(\text{BiVO}_4)_n$ nanoparticles were calculated for three different clusters families. The first one deals with $(\text{BiVO}_4)_n$ clusters possessing a monoclinic arrangement cut out of the crystal structure without any reconstruction. The second family of clusters considered the same input structures as specified previously but their geometries were fully optimized according to the total energy minimization. This means that the distances between atoms change with taking into account the influence of surface limitation. The performed procedure simulates the amorphization effect of the crystal structure. The geometry optimization was performed in Cartesian atomic coordinates with symmetry defined as C1. The gradient convergence tolerance was equal to 10^{-6} hartree/Bohr using the quadratic approximation (QA) method [27] updating the Hessian matrix during the optimization.

The Hessian evaluation was performed to exclude those structures giving rise to negative modes. The third family of the investigated clusters included structures with partial reconstruction occurring on the cluster surface.

In this case, the geometry optimization procedure was performed applying the PCM solvent model, where the environment was modeled as BiVO_4 nanoclusters with dielectric parameters measured at room temperature [28].

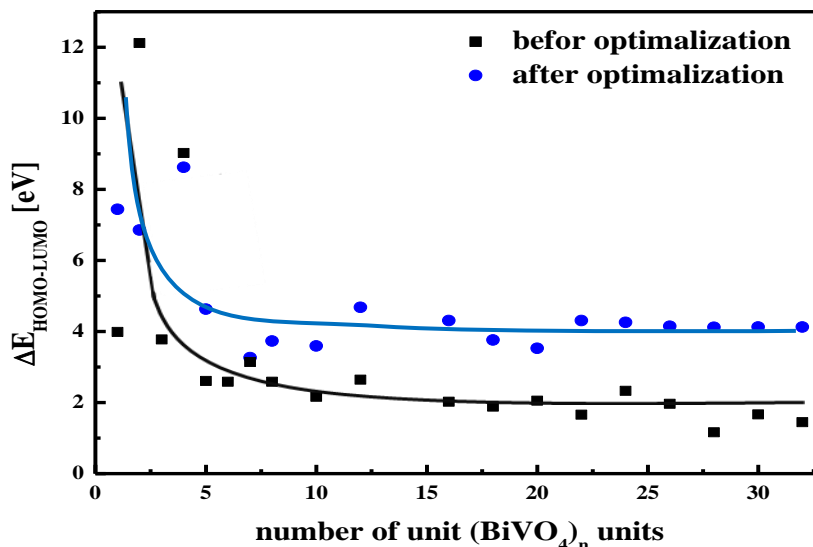


Figure 5.1.1.4. The $\Delta E_{\text{HOMO-LUMO}}$ energy gap splitting vs size calculated by PM6 semi-empirical method for frozen and optimised BiVO_4 cluster represented by the number of $(\text{BiVO}_4)_n$ units

Physical properties for both frozen and relaxed structures were calculated according to the procedure described earlier. The DFT/PBE and DFT/B3LYP functionals implemented in the D3MOL program were used to calculate an electronic property of the clusters. Unfortunately, the applied methodologies proved to be satisfactory only for small nanocrystals exhibiting size quantum confinement effect. In case of large systems where the value of the energy gap is going to be saturated, the DFT method becomes insufficient. The use of correct DFT functionals evaluate the changes in the energy band gap value versus the cluster size exhibiting the size inducing quantum confinement effect. Because the obtained results are underestimated comparing to the experimental data, it was decided to use the semi-empirical PM6 parameterized method implemented in Gaussian program [29] for future calculations. The energy difference between the highest occupied molecular orbital (HOMO) and lowest unoccupied molecular orbital (LUMO) defined as the $\Delta E_{\text{HOMO-LUMO}}$ energy gap splitting calculated for the frozen and

optimized structures versus their size is presented in **Fig. 5.1.1.4**. One may see that in both cases i.e. for crystalline and amorphous nanoparticles with increasing the size of nanoclusters, their energy gap decreases in agreement with the size induced quantum confinement effect.

The changes of the $\Delta E_{HOMO-LUMO}$ calculated for the investigated nanoparticles are consistent with the data presented by Chattopadhyay et al. [30,31]. The authors showed experimentally that the BiVO_4 nanocrystals possess an indirect band gap in the range of 3.51–3.67 eV or 2.75–2.82 eV, depending on the sample preparation and the particle size. The reported results for crystalline clusters are lower than those for amorphous structures. These results suggest that the measured clusters must have an amorphous fraction at their surface and a better crystalline order in their core part (interior).

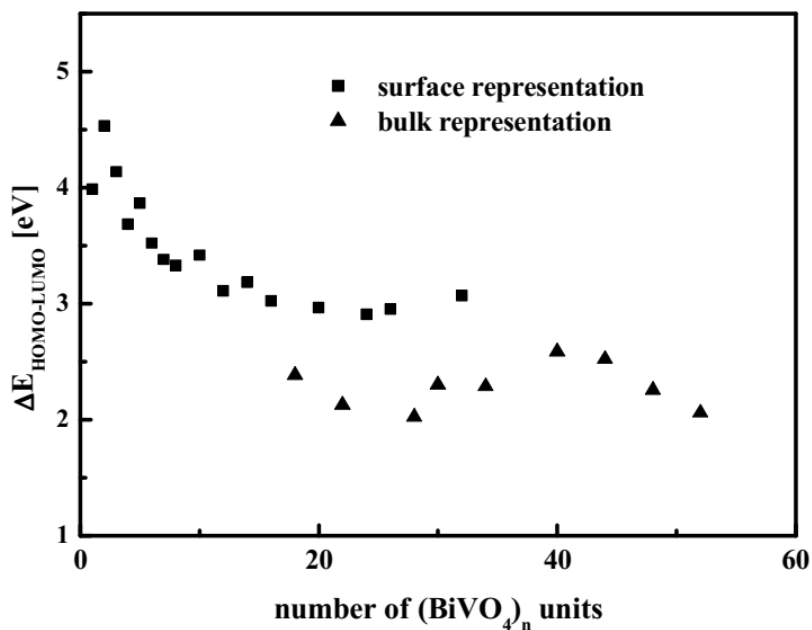


Figure 5.1.1.5. The energy gap splitting ($\Delta E_{HOMO-LUMO}$) versus size of the system calculated by PM6 method for $(\text{BiVO}_4)_n$ for surface and bulk representations

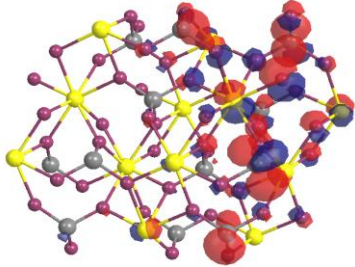
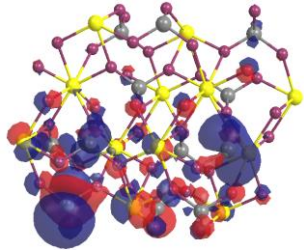
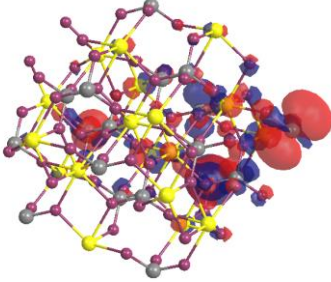
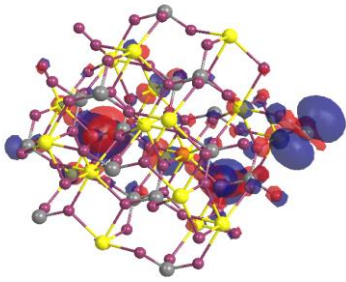
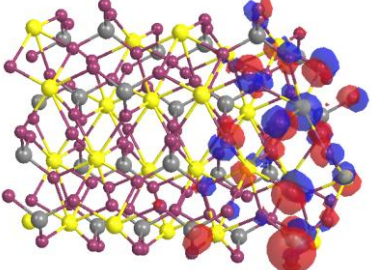
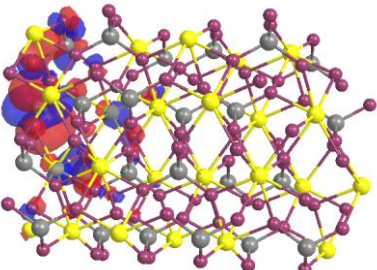
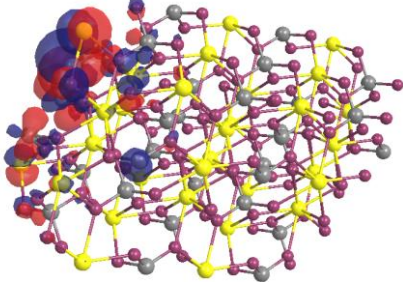
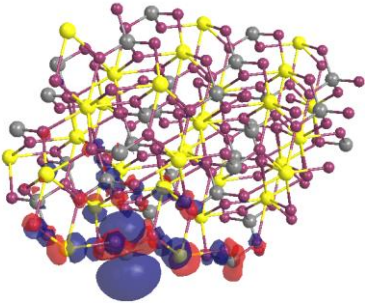
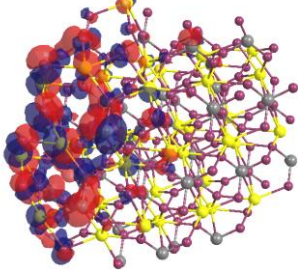
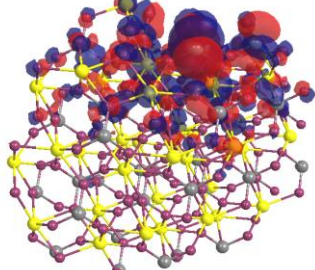
According to the above mentioned idea the electronic properties of the BiVO_4 nanoparticles were calculated by the PM6 method for partially optimized clusters. The surfaces of these clusters were reconstructed according to the environmental interaction acting on BiVO_4 nanoparticles. The cluster optimization was performed shell by shell starting from the surface and progressing to the core of the nanoparticle, taking the RMS difference for two successive optimizations as less as 1%. The obtained results, presented in **Fig. 5.1.1.5**, show that the $\Delta E_{HOMO-LUMO}$ can be divided into two parts, as

marked by rectangles and triangles. The data represented by rectangles traduces qualitatively the expected size inducing quantum confinement effect, as illustrated for BiVO₄ optimized nanoparticles (see **Fig. 5.1.1.4**). The second set of data, represented by triangles, reflects the behavior of the frozen BiVO₄ structure.

The computed data, represented by triangles, fluctuate with increasing the cluster size, but they have a tendency to be aligned to an asymptotic value close to 2.4 eV. The same value of energy gap was obtained for the bulk frozen crystal structure of the BiVO₄ as well as for non-optimized nanocrystals with a size greater than 1.0 nm (nanocrystals with $n > 10$). The obtained results are in good agreement with the data presented by Sun et al. [32]. Calculations performed for partially reconstructed clusters show that for nanoparticles smaller than 1.1 nm ($n < 20$), the physical peculiarities are generally dominated by surface effects. For larger particles (sizes above 1.8 nm, $n > 40$), the surface influence is less pronounced compared to core atoms keeping the same coordinates as involved in the bulk monoclinic crystal structure.

The HOMO and the LUMO orbitals distribution for the nanocrystals of different sizes is demonstrated in the **Table 5.1.1.2**. In the mentioned figures, the bismuth atoms are shown in yellow, oxygen in violet, while vanadium is grey. The reported data underline that the HOMO and LUMO orbitals are located in the reconstructed surface part of the cluster. Analysis of the presented orbital distribution one may observe significant similarities to the PDOS calculated for the bulk BiVO₄ material. The HOMO orbitals can be compared to a valence band from which photogenerated electrons flow, while LUMO can be approximated to the conduction band. The obtained results confirm that the HOMO orbital is built by the O 2p states and the LUMO is created by the V 3d orbitals. Compared to the bulk material, where the VBM occurs from O 2p orbitals hybridised by V 3p and Bi 6s for the optimized and frozen structure, respectively, one could conclude that the size reduction of the investigated cluster does not drastically change its electronic nature. Analysing the data collected in the **Table 5.1.1.2** one may see that the HOMO orbitals are located at the opposite side of cluster compared to the LUMO ones. It allows to conclude that in the photoactivated processes of electron transitions from HOMO to LUMO orbital, the surface area plays a key role. Increasing the active surface of nanoparticles by synthesis of the meso- or nanoporous material, will also increase photocatalytic capacity as it was confirmed experimentally by Zhang and coauthors [33].

Table 5.1.1.2. The HOMO and LUMO orbitals representation of $(\text{BiVO}_4)_n$ frozen clusters with $n = 12, 18, 24, 30, 36$ calculated by the PM6 semi-empirical parametrised method

HOMO Orbitals	LUMO Orbitals
 <p data-bbox="608 573 743 607">$(\text{BiVO}_4)_{12}$</p>	 <p data-bbox="810 573 1062 607">diameter = 0.75 nm</p>
 <p data-bbox="624 898 759 931">$(\text{BiVO}_4)_{18}$</p>	 <p data-bbox="818 898 1046 931">diameter = 1.2 nm</p>
 <p data-bbox="632 1223 767 1256">$(\text{BiVO}_4)_{24}$</p>	 <p data-bbox="807 1223 1035 1256">diameter = 1.3 nm</p>
 <p data-bbox="616 1570 751 1603">$(\text{BiVO}_4)_{30}$</p>	 <p data-bbox="815 1570 1043 1603">diameter = 1.4 nm</p>
 <p data-bbox="592 1895 727 1928">$(\text{BiVO}_4)_{36}$</p>	 <p data-bbox="839 1895 1067 1928">diameter = 1.5 nm</p>

The PDOS computed for the partially reconstructed $(\text{BiVO}_4)_{18}$ cluster indicates that the highest occupied energy levels are associated mainly with the O 2p states hybridized with the Bi 6p orbitals (**Fig. 5.1.1.6**). Similar properties were demonstrated for the bulk monoclinic BiVO_4 with frozen atomic coordinates. The main difference between the DOS of the bulk system and the nanocluster seems to be related to the contribution from Bi 6s and Bi 6p states, respectively. Moreover, it is worth noting that for nanocrystalline $(\text{BiVO}_4)_{18}$ a strong correlation is involved between Bi and O orbitals. This confirms that the electronic properties of the simulated cluster are mainly driven by the core (internal) atoms. The unoccupied orbitals with the lowest energy are composed mainly by V 3d states, with small contributions from Bi 6p and O 2p states, as was also observed for the bulk system.

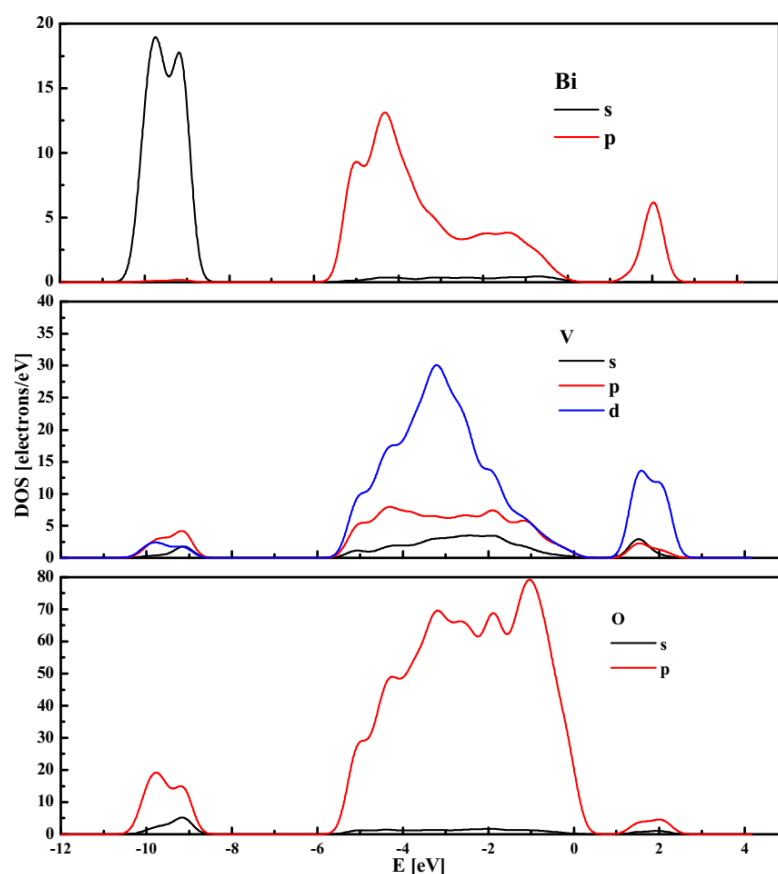


Figure 5.1.1.6. The partial density of states calculated by PM6 semi-empirical method for the partially reconstructed cluster with size 1.2 nm

Experimental Investigations

The performed experimental work focused on the synthesis of mesoporous thin films deposited on borofloat substrate. The synthesis procedure was described in **Chapter 4**. The mesoporous BiVO_4 was synthesized using two different surfactants such as P123 and F127. The resulting samples were annealed at 450°C in order to ensure the crystalline structure. XRD measurement were then performed to verify the crystalline order in the mesoporous films. The XRD analysis showed that the films synthesized by using the F127 route do not correspond to pure monoclinic phase.

Additional diffraction peaks are involved in XRD pattern between 26° and 28° irrelevant to BiVO_4 polymorphs. Therefore, the synthesis with the surfactant P123 was performed in the aim to compare its effect on the crystalline BiVO_4 form. This synthesis method gives satisfactory crystalline form for the synthesized samples as mesoporous powder (**Fig. 5.1.1.7**).

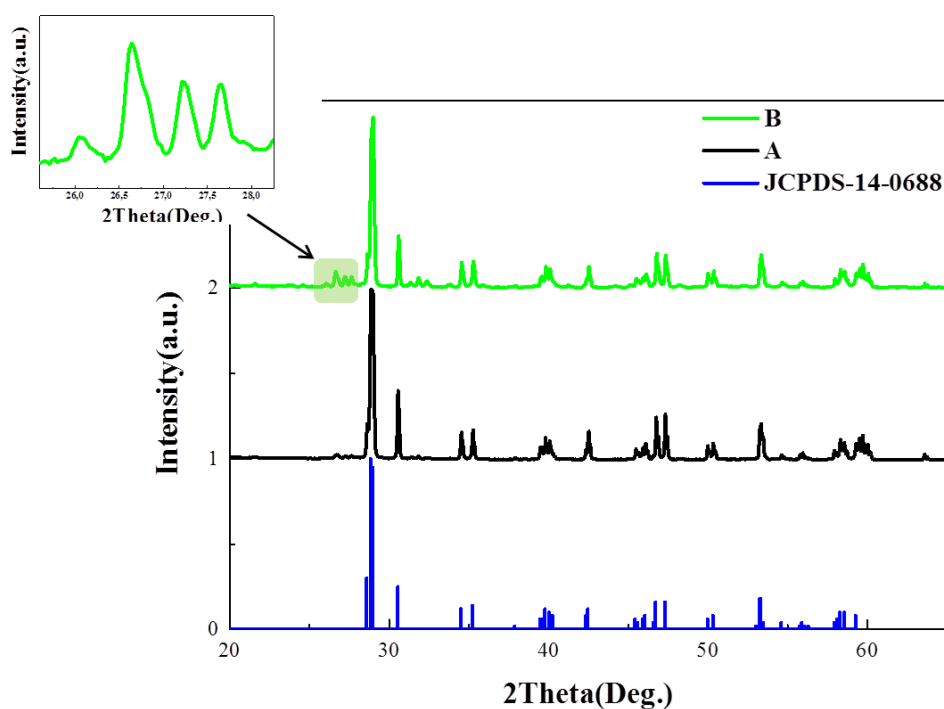


Figure 5.1.1.7. XRD analysis of the BiVO_4 powder synthesized by using the P123 (A) and the F127 (B) surfactant

Irrespective to the used surfactant, a XRD line possesses a full width at half maximum (FWHM) equal to 0.27° for both samples synthesized with the P123 and the F127 surfactant (see **Fig. 5.1.1.7**).

Based on FWHM method and following the Scherrer relation:

$$D_{hkl} = \frac{K \cdot \lambda}{FWHM \cdot \cos\theta}, \quad (5.1.1.1.)$$

the size of the BiVO₄ crystalline domains was estimated to 92,5 nm for powders samples synthesized with the P123 and the F127 surfactant.

The XRD pattern of a mesoporous thin film of the BiVO₄ synthesized with the surfactant P123 and deposited on a borofloat substrate shows good crystalline features. As shown in (Fig. 5.1.1.8), the most intense peak located at 2θ about 28.80° is consistent with the reticular plane (-121) involved for monoclinic bismuth vanadate in agreement with the standard pattern JCPDS-14-0688. The same phase account also for diffraction lines located at 2θ about 18.83, 30.56, 35.12, 39.78, 42.44, 47.17, 50.08 and 53.24°. These characteristic peaks are assigned to the crystalline planes of the monoclinic BiVO₄ respectively as (110), (040), (002), (211), (051), (042), (202) and (161).

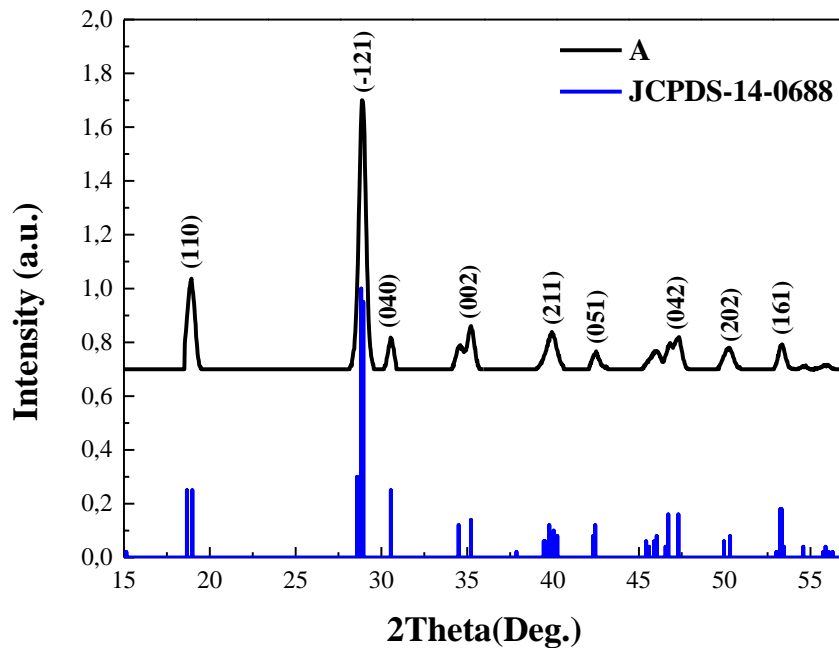


Figure 5.1.1.8. XRD pattern of mesoporous BiVO₄ thin film prepared by using P123 surfactant (A) and the standard JCPDS-14-0688 pattern assigning the BiVO₄ crystalline structure to monoclinic scheelite phase

It was also decided to investigate how the used substrates affect the crystalline structure of the deposit BiVO₄ thin films. For this purpose, silicon and borofloat substrates were used to deposit the thin films by dip coating method. As discussed in **Chapter 4**, the silicon and borofloat substrates were initially cleaned before deposition of the films. After deposition, the films were annealed and their structures analyzed by SEM.

Fig. 5.1.1.9 reports the SEM images of the BiVO_4 thin films deposited on silicon and borofloat substrates. It seems that the substrate play a key role on the morphology of the films as revealed from the shape and sizes of the deposited BiVO_4 particles. The average size of the BiVO_4 particles on the silicon substrate is about 130 nm compared to 46 nm for borofloat deposited film. The morphology of the obtained surfaces shows drastic differences between the two used substrates and SEM images reveal nanoisland features. Such surface shapes induce high contact area which improves the efficiency of heterogeneous photocatalysis as planned for the application of the considered mesoporous films. The realization for nanostructured morphologies constitutes a real advance compared to already reported synthesis of the BiVO_4 such as powders [34,35] but the specific surfaces remains quite low compared to the surface contact of our textured films. The used synthesis method combined with the substrate effect gives better film organization compared to deposition with the CVD method leading to particle size as high as 300 nm [36].

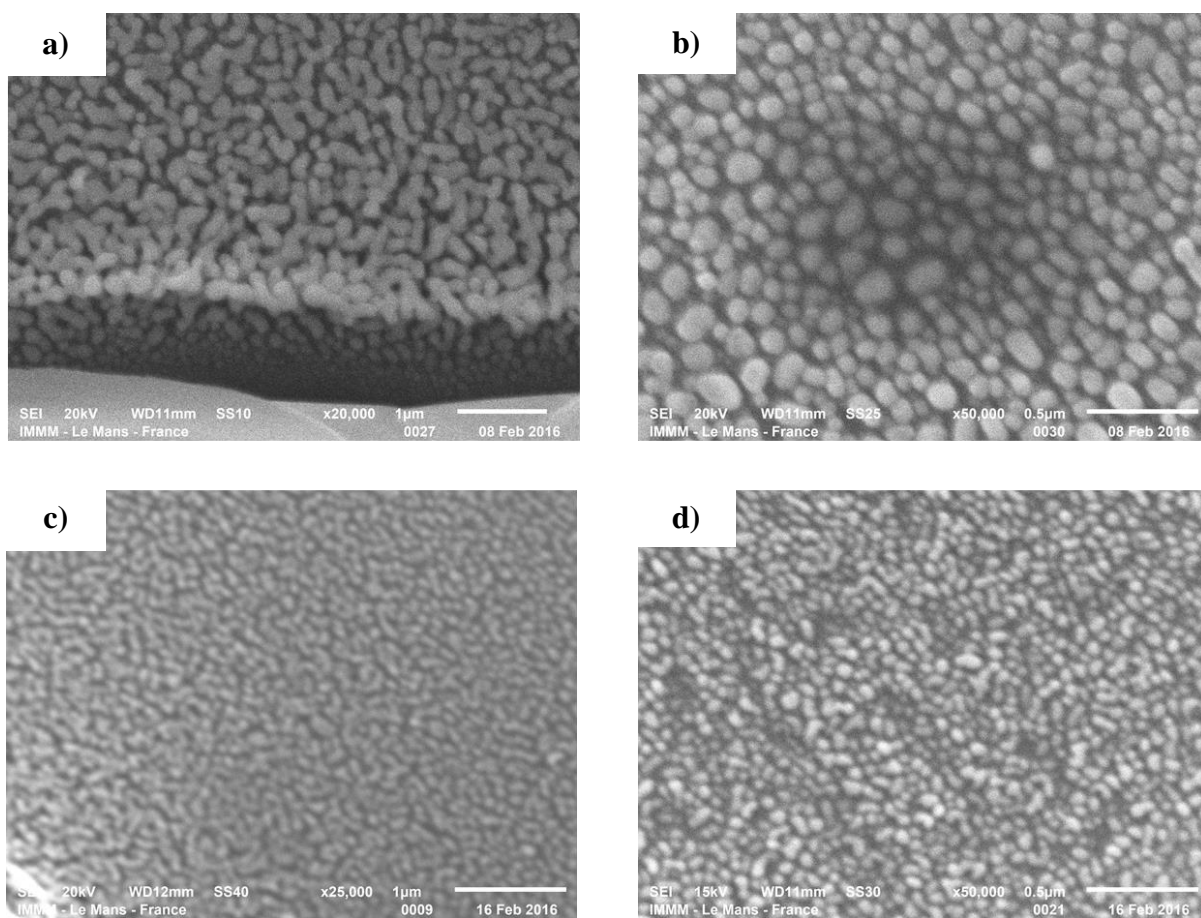


Figure 5.1.1.9. SEM images of the thin films of monoclinic BiVO_4 deposited on the silicon (a and b) and on borofloat substrates (c and d) using the dip coating method

Figure 5.1.1.10 reports the AFM images of the BiVO₄ surface with a size area equal to 1 μm². It allows a better understanding of the topology of the synthesized films and the effects of the substrate nature. Beyond the topography analysis, dimensional features of the nanostructured thin film surfaces can be also evaluated such as the film thickness and surface roughness.

Thus, on borofloat substrates, the nanoislands are tightly packed on the sample surface and hold between 50 nm and 80 nm in agreement with SEM analysis.

The AFM results give a better estimation of the nanocrystalline sizes compared to the approximate values calculated from the Scherrer's relation. On a basis of the AFM analysis (see **Fig. 5.1.1.10**), the existence of the highest islands on the surface with high material density was confirmed. The porosity, occurrence of roughness and increased surface area make the tested sample promising for photocatalytic applications.

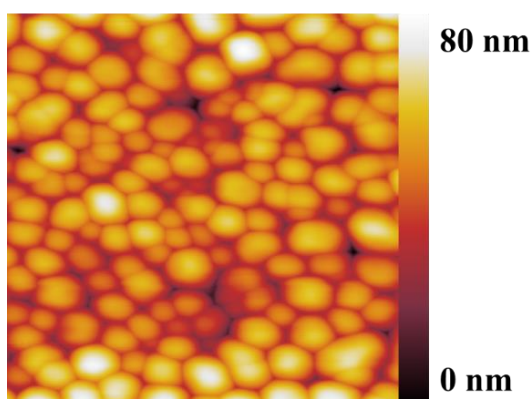


Figure 5.1.1.10. AFM image of the thin film of BiVO₄ deposited on a borofloat substrate. The size of the analyzed samples is about 1 μm x 1 μm

5.1.2. UV-vis absorption spectra of mesoporous BiVO₄ films

The UV-vis absorption spectra of the mesoporous BiVO₄ films were experimentally measured and compared to theoretical predictions performed on nanocrystalline clusters. Based on the work of Sun and coauthors [37] it has been shown that the first absorption peak is shifted to lower wavelength with the increase of nanocrystalline size as also confirmed by other experimental reports [38,39]. By controlling the size, shape and porosity of the films it is possible to fine-tune the optical properties with a particular emphasis on the visible light absorption. The effect is a key requirement for the efficiency of visible light driven photocatalytic processes. The UV-vis absorption spectra obtained for films deposited on borofloat substrate are located in the range 350 - 470 nm, i.e. a fraction of visible spectral range (**Fig. 5.1.2.1**).

Compared to the well-known photocatalyst as the TiO_2 in a non-doped form with a spectral absorption in UV range [40,41], mesoporous thin films of the BiVO_4 are more promising to harvest the visible range of the solar radiation.

The band gap of the BiVO_4 thin films was calculated according to the Kubelka-Munk formula [42]. The obtained value of the E_g is equal to 2.55 eV (**Fig. 5.1.2.2**, bottom panel) and is in agreement with theoretical predictions (2.60 eV) performed for partially reconstructed $(\text{BiVO}_4)_{18}$ cluster having a size of 1.2 nm, using semi-empirical PM6 parameterized calculations. The UV-vis absorption spectrum of the frozen monoclinic BiVO_4 single crystal was also calculated. These spectra related to both configurations are shown in **Fig. 5.1.2.2** (top panel). The absorption edge calculated for the nano-sized cluster is shifted to higher energy compared to that of the bulk crystal.

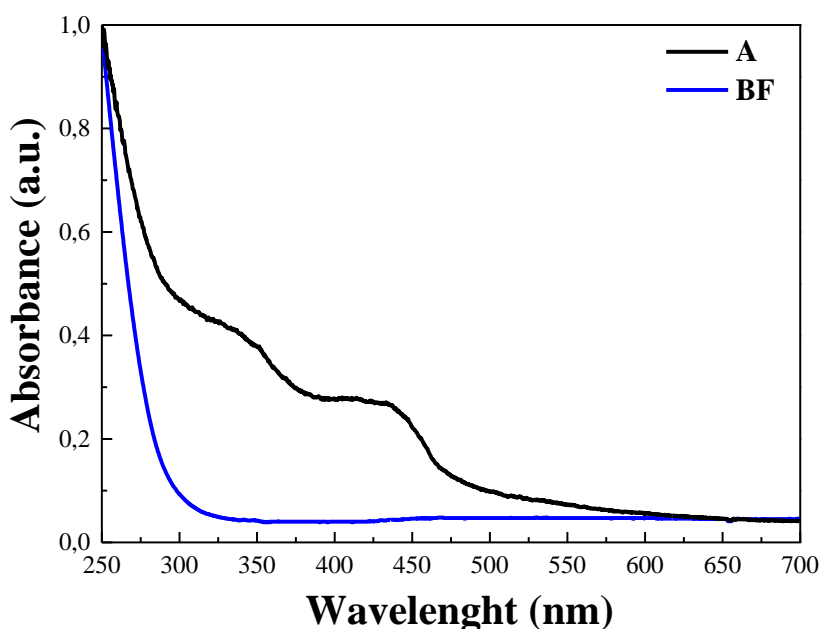


Figure 5.1.2.1. The UV-vis absorption spectra measured for the borofloat (BF) and the thin film of the monoclinic BiVO_4 deposited on the borofloat substrate

Such a difference is characteristic of the size inducing quantum confinement effect and is in agreement with the work of Karunakaran et al. [43]. Moreover, for the bulk infinite structure, the optical spectrum is more extended with two main features reflecting the indirect band gap system. The UV absorption observed in monoclinic BiVO_4 is associated with a band transition from O 2p to V 3d, whereas visible light absorption is due to the transition from a valence band formed by Bi 6s or a hybrid orbital of Bi 6s and O 2p to a conduction band of V 3d. This is in agreement with the data presented in the work of Ng et al. [44].

The presented results confirm the existence of a quantum confinement size effect for both the simulated and the experimental system. As the crystallite size increases, the influence of the surface on the interaction with the environment became dominant [45,46]. It is worth noting also that at the nanoscale, the decrease in confining dimension makes the energy level discrete and widens the band gap leading the blue shift of the absorption spectra. Additionally, the surface of the partially reconstructed nanoparticles was modified according to the environmental effect of the interacting bismuth vanadate. In this case, the implemented cluster model of partially modified structures is a good model for a mesoporous material to predict its electronic properties so crucial for photocatalytic applications.

To sum up, the experimental optical features obtained on a mesoporous material are consistent with the theoretical calculations carried out for partially reconstructed nanostructures. This close correlation makes us confident in the developed numerical approach to analyze the electronic and optical effects of this class of semiconducting oxides. The size quantum confinement effect was well demonstrated theoretically on the optical spectrum of a nano-sized cluster. The photoinduced charge transfer mechanism under visible light radiation is of primary importance for the photocatalytic responses of semiconductors. In the same context, nanostructured systems composed of nanoparticles possess high specific surfaces area, which plays a crucial role in heterogeneous photocatalysis. This was also confirmed by the fact that the active HOMO and LUMO orbitals were located at the nanoparticle surface. However, as was shown from calculations, the spectral range of absorbed sunlight observed for nanoparticles was shifted to higher energies, which limits the absorption quantum efficiency. Thus, a balance must be achieved between the size reduction and the induced widening of the band gap. This is a hot topic in major photoinduced phenomena since the modulation of the electronic structure and density of states may be ensured by the size and shape design.

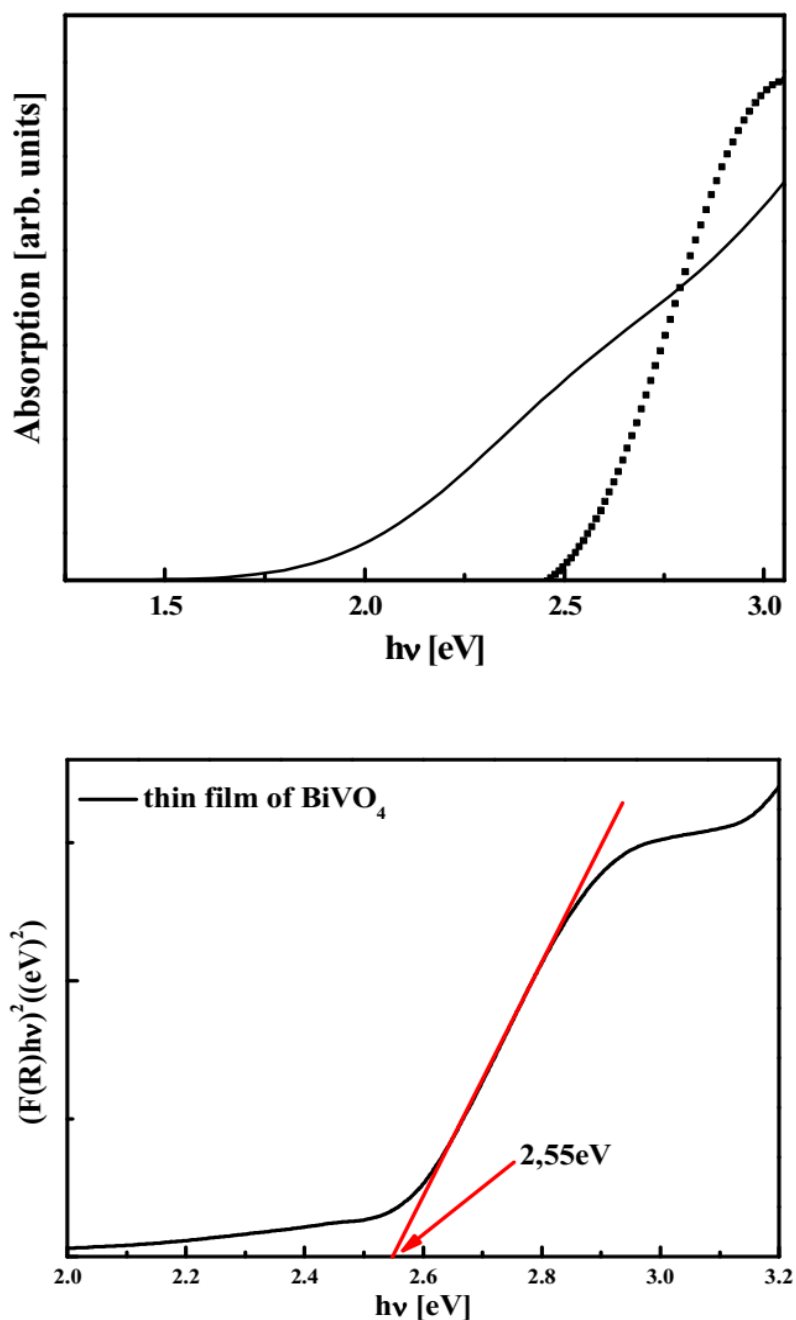


Figure 5.1.2.2. (Top panel) Theoretical UV-vis absorption spectra calculated for bulk (solid line) and nanosized (dashed line) BiVO₄ structures by using DFT/PBE and semi-empirical PM6 parameterized method, respectively. (Bottom panel) Tauc plot of $[F(R)hv]^2$ versus hv for the of BiVO₄ monoclinic thin film deposited on the borofloat substrate

5.1.3. Analysis of the active vibrations using IR and Raman spectroscopy

The vibrational properties of the investigated materials were characterized by Raman spectrometry. These data were obtained for the synthesized BiVO₄ thin films as well as on theoretically simulated clusters using quantum chemical calculations.

The vibrational properties were analyzed theoretically for $(\text{BiVO}_4)_n$ clusters with frozen and optimized atomic coordinates. The frozen clusters possess the same atomic arrangement as involved in monoclinic bismuth vanadate. The optimized structures have a tendency to create the amorphous configurations according to the requirement of the total energy minimum.

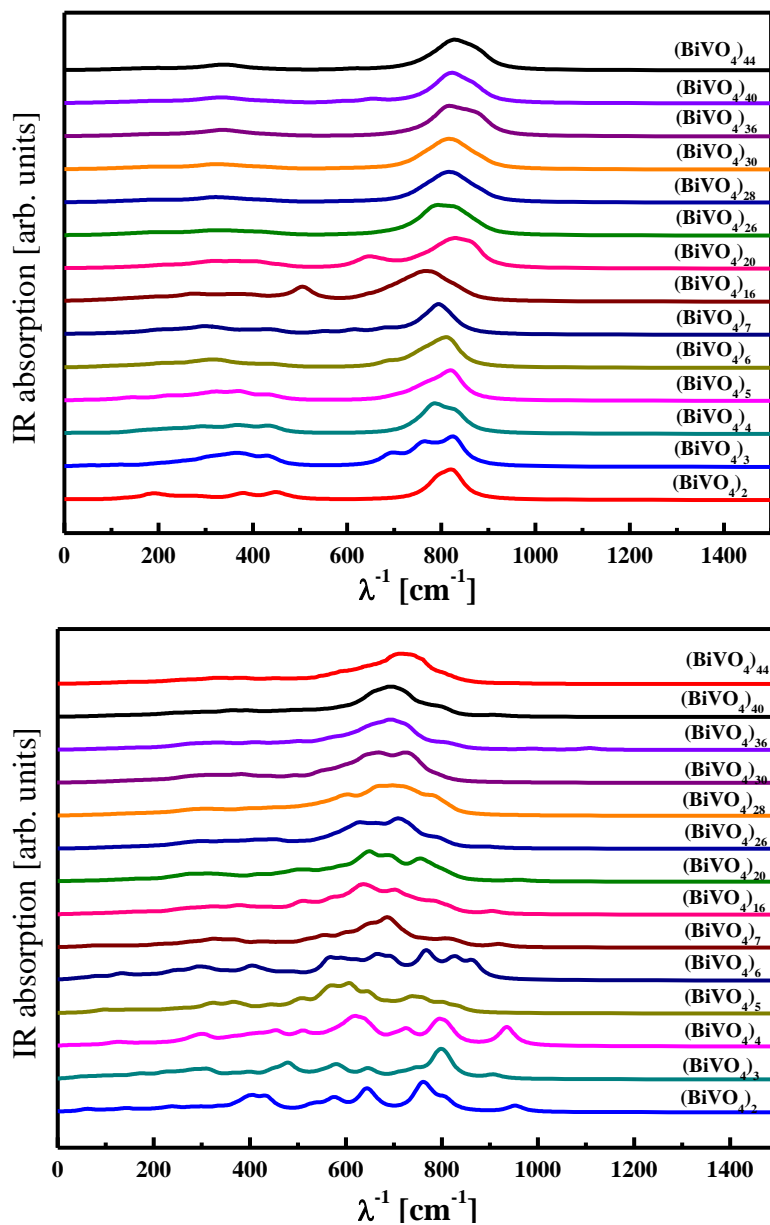


Figure 5.1.3.1. IR spectra calculated by PM6 methodology for frozen (top panel) and optimised (bottom panel) $(\text{BiVO}_4)_n$ clusters of different sizes.

First of all the IR absorption spectra were calculated using the PM6 methodology for both frozen and optimized clusters with different size. The calculated IR spectra for the frozen structure of nanoparticles show a broad band around 800 cm^{-1} , which develops

for large-sized clusters (see **Fig. 5.1.3.1.** top panel). Experimental data obtained by Zhang et al. [39] showed that the BiVO₄ nanoparticles are characterised by a broad and strong IR band near 728 cm⁻¹ with shoulders at 892, 822, 684 and 632 cm⁻¹. Compared the theoretically obtained data to the ones of Zhang et al. one may conclude that the significant influence of core atoms of the nanoparticle properties is noticed, particularly when the cluster size increases.

For small clusters, more important influence on the vibrational properties occurs from surface atoms. This is illustrated in the case of clusters with small sizes, where the IR signature is quite different for the optimised and frozen configurations (see **Fig. 5.1.3.1.**). This contrasts with large-sized clusters, such as (BiVO₄)₄₄, where the same shape of the IR spectra was qualitatively obtained irrespective of the atomic arrangement being optimised or frozen. The main reason for such a behaviour lies in the optimisation procedure inducing reconstruction and relaxation at the outermost cluster surfaces while preserving the core atoms. As the small clusters are highly sensitive to surface atoms, in contrast to large-sized clusters, drastic changes occur on their IR spectra, as demonstrated from the performed calculations.

Taking into account the effect of electron–phonon interaction, evaluation of the Raman spectra related to the selected clusters was performed by using the parametrized PM6 semi-empirical method. These spectra were calculated using a standard procedure implemented in the Gaussian program package. **Fig. 5.1.3.2.** illustrates the impact of the size on the Raman spectra of the BiVO₄ clusters. Therefore, similar conclusions can be defined for Raman spectra as it was stated for calculated IR spectra. In particular, the main contribution occurs from core atoms of the clusters. For small clusters, where the ratio of the surface atoms to the internal ones is high, the main band located at 800 cm⁻¹ is shifted and the spectrum part in the low wavenumber range is less detailed. The Raman spectrum performed for the nanosized BiVO₄ is dominated by an intense Raman band at 827 cm⁻¹, assigned to $\nu_s(\text{V-O})$, and with a weak shoulder at about 709 cm⁻¹, assigned to $\nu_{as}(\text{V-O})$ [39]. In the Raman spectrum calculated for (BiVO₄)₄₀ one may notice the non-symmetric band at a position of 800 cm⁻¹ with the same shoulder depicted in the low wavenumber part.

The highest intensity peak seen in the **Fig. 5.1.3.2.** corresponds to the symmetrical stretching V-O mode. Its positions for frozen and relaxed structures are presented in **Table 5.1.3.1.**

The results show that the values for both smaller and larger clusters are close to the experimental values. The biggest discrepancies are for nanocrystals with 24 and 30 units of the BiVO_4 , especially for structures after geometry optimization. The maximum Raman intensity for the optimized structures is shifted to longer wavelengths compared to the frozen clusters. Positions of the Raman shift for individual frozen clusters are reduced and vary up to 50 cm^{-1} from the experimental value and reaches 140 cm^{-1} for geometry optimized clusters.

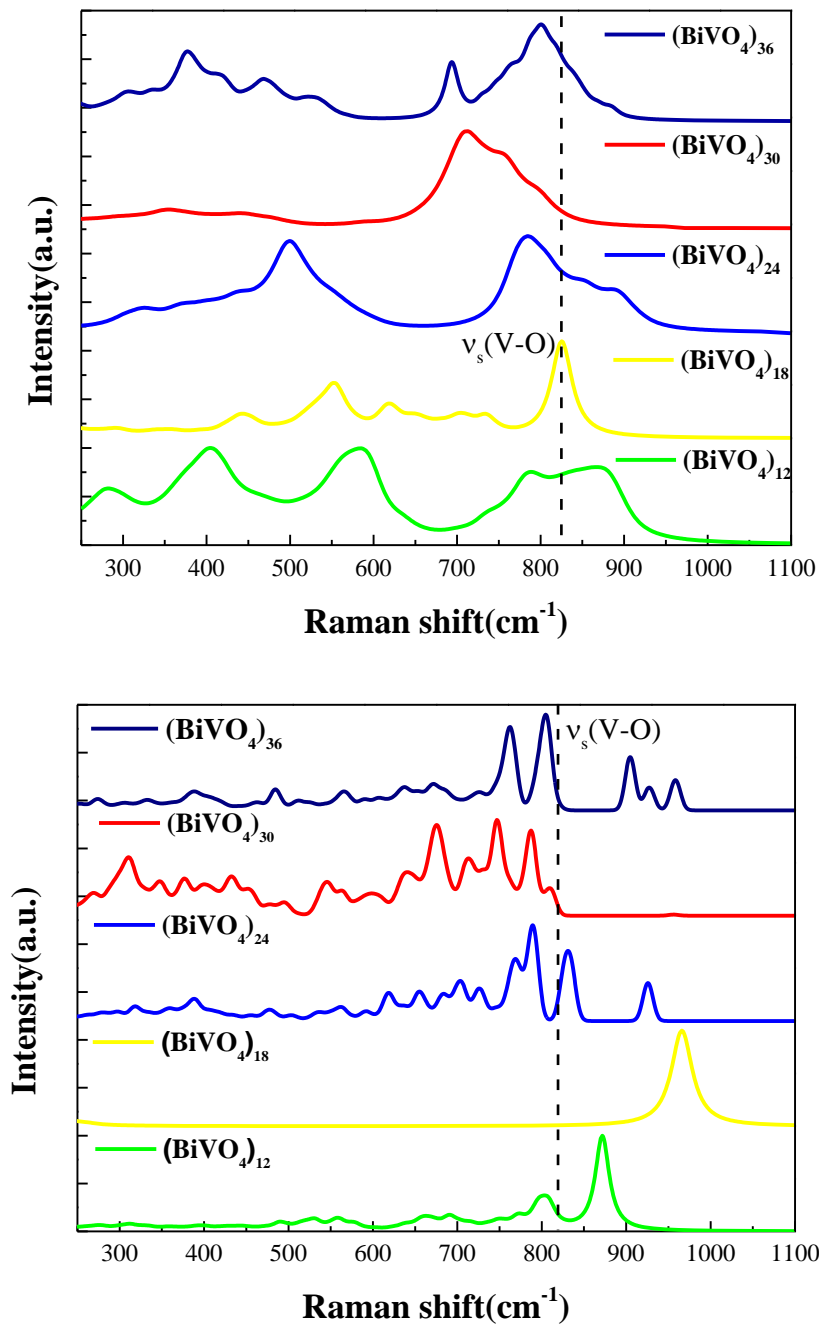


Figure 5.1.3.2. Raman spectra calculated by PM6 methodology for frozen (top panel) and optimized (bottom panel) $(\text{BiVO}_4)_n$ clusters

Table 5.1.3.1. Maximum of Raman intensity - location of symmetrical stretching of V-O mode for the structure after and without optimization process

Cluster	Raman shift (cm ⁻¹)	
	Optimized	Frozen
(BiVO ₄) ₁₂	872.65	870.00
(BiVO ₄) ₁₈	964.30	824.54
(BiVO ₄) ₂₄	790.17	782.24
(BiVO ₄) ₃₀	748.23	708.75
(BiVO ₄) ₃₆	871.70	802.67

Comparative results between theoretical and experimental investigations are carried out as illustrated in **Fig. 5.1.3.3**. The comparison is made between the Raman spectra calculated by PM6 methodology for frozen and optimized (BiVO₄)₁₈ clusters and the experimental spectrum performed with the laser radiation at 568 nm on the mesoporous BiVO₄ thin film deposited on the borofloat substrate. For bismuth vanadate films deposited on the borofloat substrate, the highest peak intensity located at the 822 cm⁻¹ corresponds to the symmetrical stretching of the V-O mode (**Fig. 5.1.3.3**, band A). Frozen (BiVO₄)₁₈ cluster containing the symmetrical stretching of the V-O is consistent with the experimental spectrum. The same statement is relevant for the vibrations corresponding to the asymmetric stretching V-O are at 631 cm⁻¹ and 716 cm⁻¹. Asymmetric $\delta_{as}(\text{VO}_4^{3-})$ and symmetric $\delta_s(\text{VO}_4^{3-})$ deformation of the VO_4^{3-} group occur at 323 cm⁻¹ and 361 cm⁻¹, respectively [39]. In the case of mesoporous thin film structure both of these Raman bands are resolved with high intensity but the second peak is more pronounced (**Fig. 5.1.3.3**, band B'). From computational results on the frozen (BiVO₄)₁₈ cluster, similar behaviour is observed (**Fig. 5.1.3.3**, band B). The small discrepancy on the band positions may be explained by the fact that anharmonic vibration terms were not considered in the calculation model. The bands labelled as C are seen for the geometry optimized (BiVO₄)₄₀ cluster and occurs probably from the same vibrational features as those leading to the bands at 366 and 324 cm⁻¹. The relaxed structure do not exhibits peak corresponding to the V-O distances. The V-O bonds length relaxed according to the total energy minimization procedure modify the Raman band positions and the amorphization of the cluster create wavenumber distribution which broaden the bands leading to vibrational density of states features [47]. It gives the broad peak with the centre localized at more than 900 cm⁻¹.

Very similar behaviour was observed in Ruiz Preciado and co-authors work illustrating vibration properties of the NiTiO₃ nanoparticles [48].

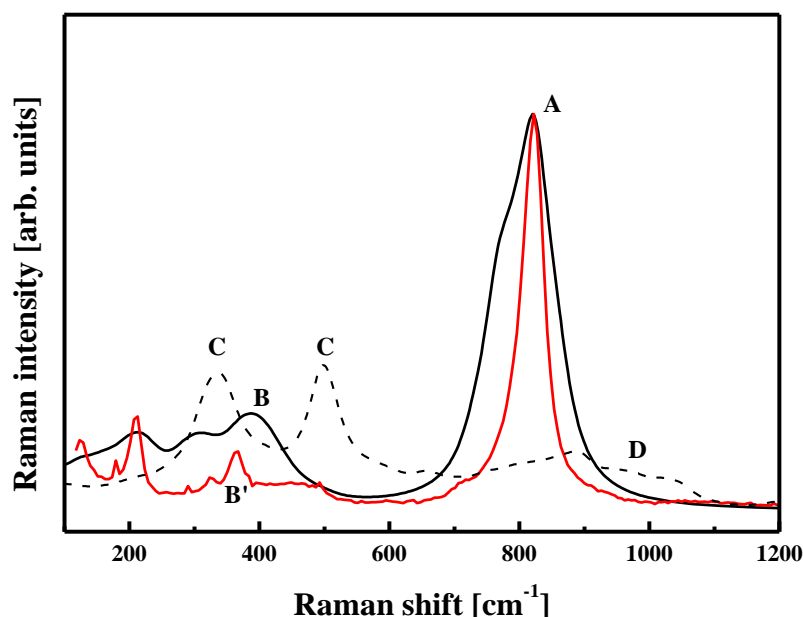


Figure 5.1.3.3. Raman spectra calculated by PM6 methodology for frozen (black solid line) and optimised (black dashed line) (BiVO₄)_n clusters and the experimental one (red line)

5.1.4. Study of the photocatalytic properties

The study of the photocatalytic properties of bismuth vanadate thin films deposited on a borofloat substrate was performed by analyzing changes of the concentration of organic dye in aqueous solution of the photocatalytic material. For this purpose, methylene blue (MB) has been diluted up to $10^{-5} \frac{\text{mol}}{\text{dm}^3}$. In the **Fig. 5.1.4.1.** is shown the change of MB absorption over time during the photocatalytic reactions with BiVO₄ films. The absorption band show a monotonuous decrease in their intensity without any change on the band position located at 670 nm for the maximum intensity. It seems important that the difference for the highest absorbance between 3 and 5 hours under irradiation seems to be negligible. This could have been caused by excessive amount of MB blocking the active centers on the surface of the photocatalyst and thus inhibiting the whole process. Based on the UV-vis absorption spectra investigations described above, the representation of $\ln(C_0/C)$ versus time was calculated and presented in **Fig. 5.1.4.2.** Mentioned dependence leads to degradation rate of the MB dyes about 75 % by using the thin film of bismuth vanadate. It means that at the active surface of the BiVO₄ organic dyes could be adsorbed and then efficiently decomposed into simple non-toxic

inorganic compounds. The obtained value for the degradation rate confirms previous considerations and highlights the use of BiVO_4 in the morphology of mesoporous organization for efficient photocatalytic processes.

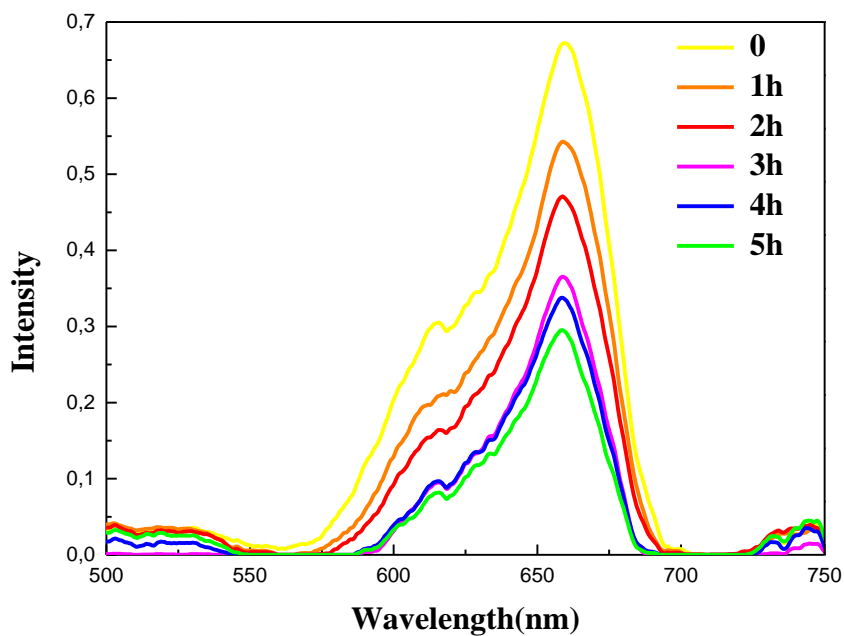


Figure 5.1.4.1. UV-vis spectra of degradation methylene blue dyes in solution by thin film of monoclinic BiVO_4 under irradiation

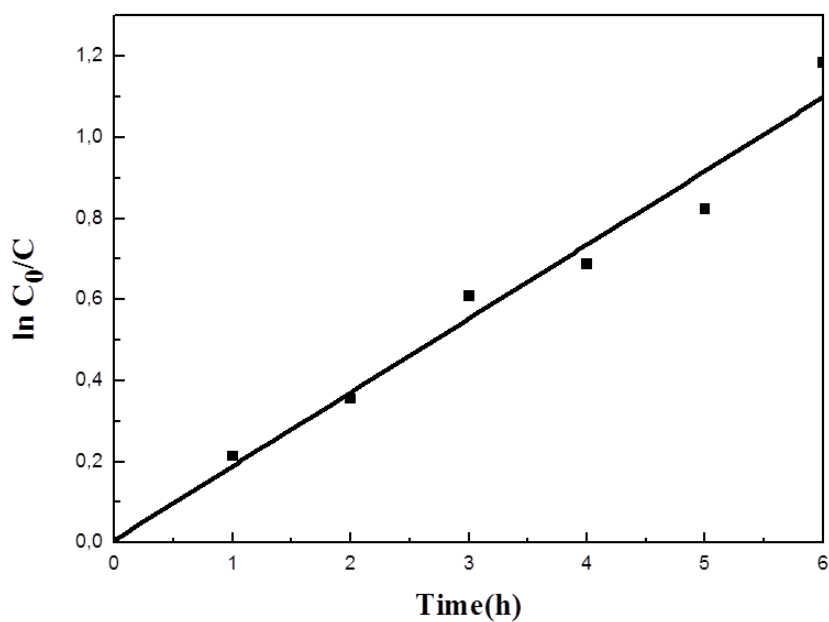


Figure 5.1.4.2. Kinetics of the degradation of the MB dyes obtained from the time evolution of the intensity of the absorption band related to MB dyes content in a solution

5.1.5. Conclusion

The results of quantum-chemical calculations and experimental studies allowed a detailed analysis of the nature of the monoclinic bismuth vanadate. The established model for numerical simulations are consistent with the experimental results.

A new method of bismuth vanadium synthesis has been developed. Thin layers of bismuth vanadate deposited on a borofloat substrate exhibit nanostructured surfaces with particle size of about 50 nm, resembling islands of irregular structure, as confirmed by SEM and AFM measurements. At the same time, the pure monoclinic phase in the sample synthesized using P123 surfactant was confirmed by XRD analysis. On the other hand, theoretical studies of the electronic properties of bulk material with frozen and relaxed crystal structure illustrated the contribution of particular orbitals to the formation of the valence and conduction bands. It has been established that the top of the valence band for the frozen structure is formed primarily by the hybridized O 2p and Bi 6s orbitals. Both the frozen and optimized material had a downstream CB composed by the V 3d orbitals. The frozen structure leads to E_g equal to 2.4 eV, which coincides with the experimental results for the crystal monoclinic BiVO_4 structure. The quantum confinement size effect was confirmed for a series of nanocrystals, whether modeling was done with or without optimization of geometry. On the other hand, $\Delta E_{\text{HOMO-LUMO}}$ was significantly different from the relaxed and frozen (unrelaxed) clusters leading to 4 eV and 2 eV, respectively. The HOMO and LUMO orbitals located at the surface of clusters were determined. They illustrate the electron cloud features associated with these two states and compare them to the valence and conduction band in the bulk material, respectively. The calculations performed for partially optimized clusters suggest that the studied clusters must have an amorphous fraction at their surface and a better crystalline order in their core part.

Optical properties were determined for bismuth vanadate in the form of thin films lead to an absorption band in the range 350-470 nm. This means that the material can absorb radiation in the visible light range and thus apply as visible light driven photocatalyst. Additionally, the experimental band gap was estimated to be 2.55 eV. The obtained data were compared with the results of quantum-chemical calculations (2.60 eV) for nanosized clusters of the BiVO_4 . The result for a cluster with 1.2 nm as diameter agrees with the calculated data following the Kubelka-Munk methodology.

The Raman spectra calculated for different nanocrystals with and without geometry optimization do not coincide fully with experimental spectra. It should be noted, that frozen structures show an agreement with experiments related to the V-O symmetrical torsional vibrations at 822 cm^{-1} . Unfortunately, in the case of symmetrical and asymmetric deformations of the VO_4^{3-} group a shift towards longer wavelengths can be observed. Analyzing the IR and Raman spectra one may say that the small clusters are highly sensitive to vibrations of the surface atoms, in contrast to large-sized clusters where the core atoms are important.

Photoactivity of the obtained mesoporous thin film was confirmed in heterogeneous photocatalysis with MB dyes in solution. The effect of photocatalyst is clearly shown on the reduction of the dye concentration in solution. Obtaining the MB photodecomposition results in a photocatalytic yield equal to 75 %, suggesting that the material has a promising photocatalytic potential.

5.2. Quantum-chemical calculations and experimental investigations of semiconducting-organic hybrid systems based on the BiVO₄

5.2.1. Analysis of the structure and electronic properties

Theoretical calculations

The performances of a photocatalyst depend on a several parameters related to the structure as well as to the photoinduced charges mobility and their lifetime. The intrinsic properties of a given photocatalysts are not the most optimal to ensure the highest photocatalysis efficiency. Therefore, several strategies were developed to optimize the parameters behind the charge transfer such as enhancement of the photogenerated charges density and elongating their lifetime. In this aim, doping the photoactive material by suitable elements (metallic or nonmetallic) was developed to reduce the band gap and enhance the efficiency of the charge transfer. The second strategy which was applied in the dye sensitized solar cells consists in anchoring of an organic dyes on the photoactive semiconducting system contributing to high density of photoinduced charge transfer.

The third methodology is related to the association of metallic clusters with the photocatalysts in defined architectures. Particularly, mesoporous photocatalysts with nanosized clusters offer large contact area between the photocatalyst and the metallic clusters. For this composition, important plasmonic effects occur at edge interfaces and contribute to enhanced the electromagnetic field around the photocatalyst. All the above approaches are devoted to improve an ability of the photoactalyst to harvest wide spectral range and ensure the highest photocatalytic efficiency.

The present work is devoted to the association of organic dyes with the photocatalyst to enhance their photocatalytic efficiency. Both theoretical calculations and experimental investigations were carried out and analyzed. In order to sensitize thin layers of the BiVO₄ by organic groups three molecules showing charge transfer phenomena under suitable light radiation were considered.

These molecules are as follows: the commercially available D149 molecule and the LIGAND as well as COMPLEX dyes [49]. Forms of their chemical representations are illustrated in **Fig. 5.2.1.1**. The LIGAND and COMPLEX dyes were tested for the first time in the photocatalytic process.

The calculations are devoted to predict the electronic peculiarities of these organic molecules in order to implement them in the photocatalytic applications.

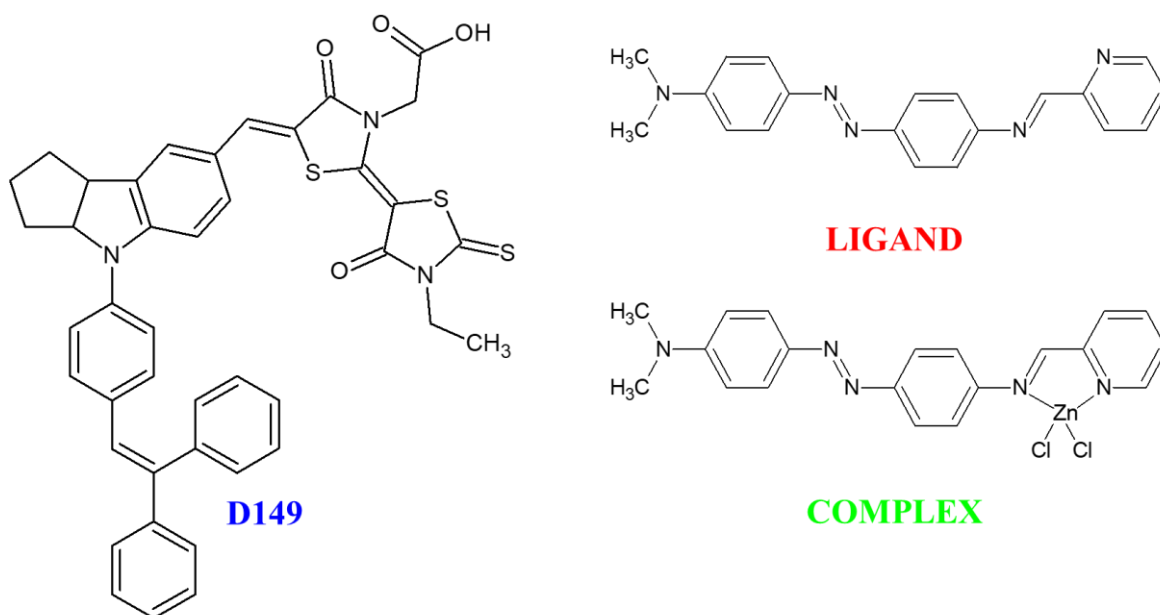


Figure 5.2.1.1. Structure of the organic dye molecules: D149, LIGAND and COMPLEX

The geometry structures of the organic dyes molecules were initially optimized using quantum chemical calculations according to the total energy minimization procedures. The calculations were performed applying semi-empirical PM6 parametrised method as it is implemented in Gaussian program [29,50]. The procedure was performed for isolated molecule in vacuum. The initial geometry was built up using the ACD/ChemSketch, an integrated software package from Advanced Chemistry Development, Inc. The minimum of the potential energy surface was calculated for neutral molecules using restricted Hartree–Fock (RHF) method with the SCF convergence criterion equal to 10^{-5} hartree. No symmetry rules were imposed during the electronic structure analysis. The geometry optimization was performed in Cartesian atomic coordinates. The gradient convergence tolerance was equal to 10^{-6} hartree/Bohr using the quadratic approximation (QA) method [51] updating the Hessian matrix during the optimization.

To predict electronic and vibrational properties of the investigated molecules the quantum chemical calculations were performed using their structures with optimized geometry. These properties were calculated for the isolated molecules at the RHF SCF level with energy convergence criterion chosen to be 10^{-12} hartree.

The **Fig. 5.2.1.2.** illustrates the distribution of the HOMO (left side) and LUMO (right) orbitals of the D149, LIGAND and COMPLEX calculated using the semi-empirical PM6 parameterized method. The HOMO orbital of the D149 molecule is delocalized over the π -electron system with the highest electron density located on the central nitrogen atom. It is noticed that the LUMO orbital have larger influence of the terminal carboxyl group compared to the HOMO orbital. Therefore, the HOMO–LUMO excitation induced by light irradiation could shift the electron distribution from the middle of the molecule to the anchoring moieties, thus favoring electron injection from dye to BiVO_4 . Whereas, for LIGAND and COMPLEX molecules was established that the HOMO orbitals are located on the dimethylamino group possessing donor character while the iminopyridine group play the role of acceptor and the LUMO orbitals are predominantly located on its atoms.

Analyzing of the contribution of atomic orbitals to the formation of the LUMO orbitals the $-\text{COOH}$ or $-\text{N}$ were chosen in the D149 and LIGAND/COMPLEX molecules, respectively, as the groups involved in the sensitizing process of the bismuth vanadate nanocrystals. It is due to the fact that these groups are located in position where is the greatest electron concentration forming the LUMO orbitals. Hybrid systems were built using the ACD/ChemSketch program by combining an organic molecules via selected linking groups with the $(\text{BiVO}_4)_{18}$ nanostructure. An anchoring of the D149 is realized by removing hydrogen atom from the carboxyl group and combining the oxygen atom with the vanadium atom located on the surface of the nanocluster. In the case of systems with LIGAND and COMPLEX molecules, the connection occurs through the nitrogen atom located in the aromatic ring on which the highest density of LUMO orbitals was located.

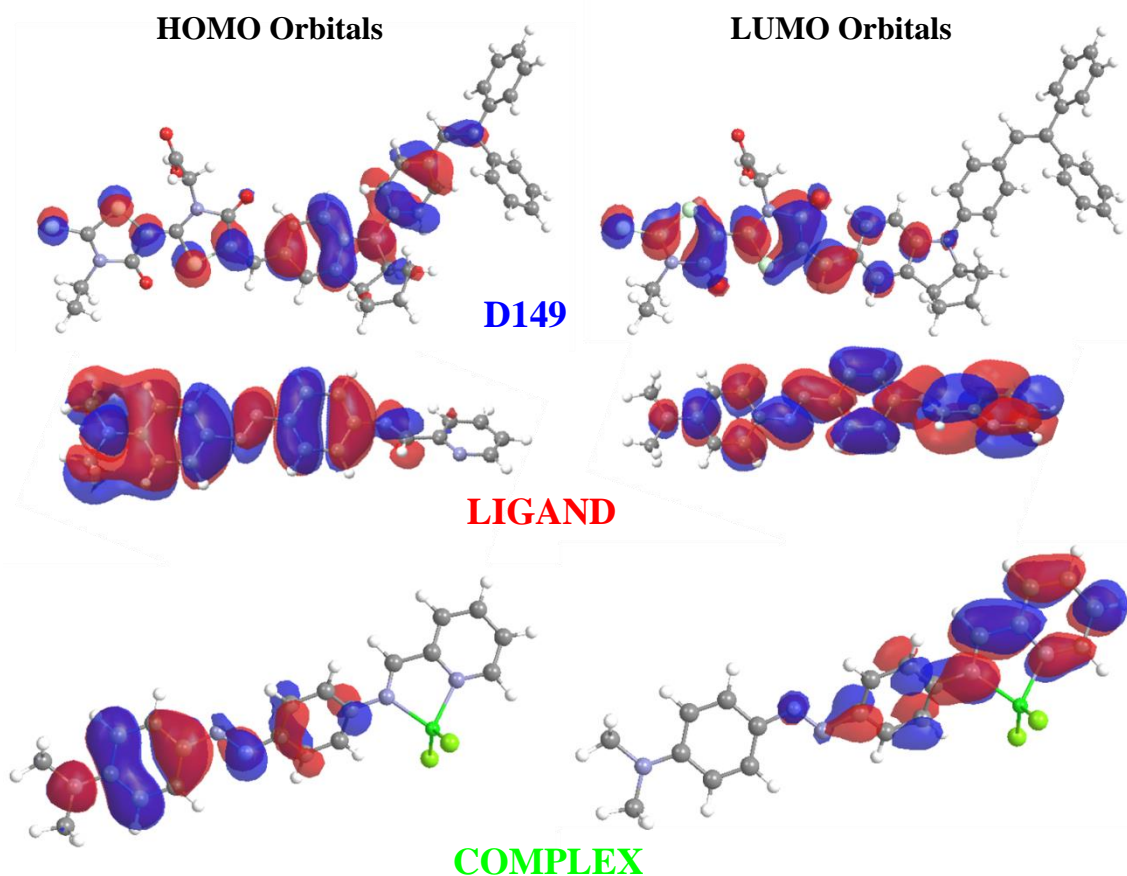


Figure 5.2.1.2. The HOMO and LUMO orbitals of the D149, LIGAND and COMPLEX organic dyes molecules calculated by the semi-empirical PM6 parameterized method

The geometries of the hybrid systems were optimized according to the total energy minimization using the methodology and parameters the same as it was described previously for the optimization procedure applied for the isolated dye molecules. In this case, linking vanadium atom and three neighbouring oxygen atoms located on the BiVO_4 cluster surface serving as grafting sites for the dye molecules, were relaxed. The remaining part of the BiVO_4 cluster was frozen. Also the atomic position of the dye molecules were allowed to be relaxed. Concluding, one may say that in the generated systems, the optimization of the atomic positions concerns the organic dye molecules and the part of nanostructure surface namely, connecting vanadium atom and the 3 oxygen atoms surrounding mentioned vanadium. The remaining part of the nanostructure, which had no direct relation to the organic dye has been frozen. The analogous procedure was performed for the COMPLEX and LIGAND molecule attached to the surface of the BiVO_4 nanostructure. In this case the $(\text{BiVO}_4)_{18}$ cluster, described in previous chapter was used.

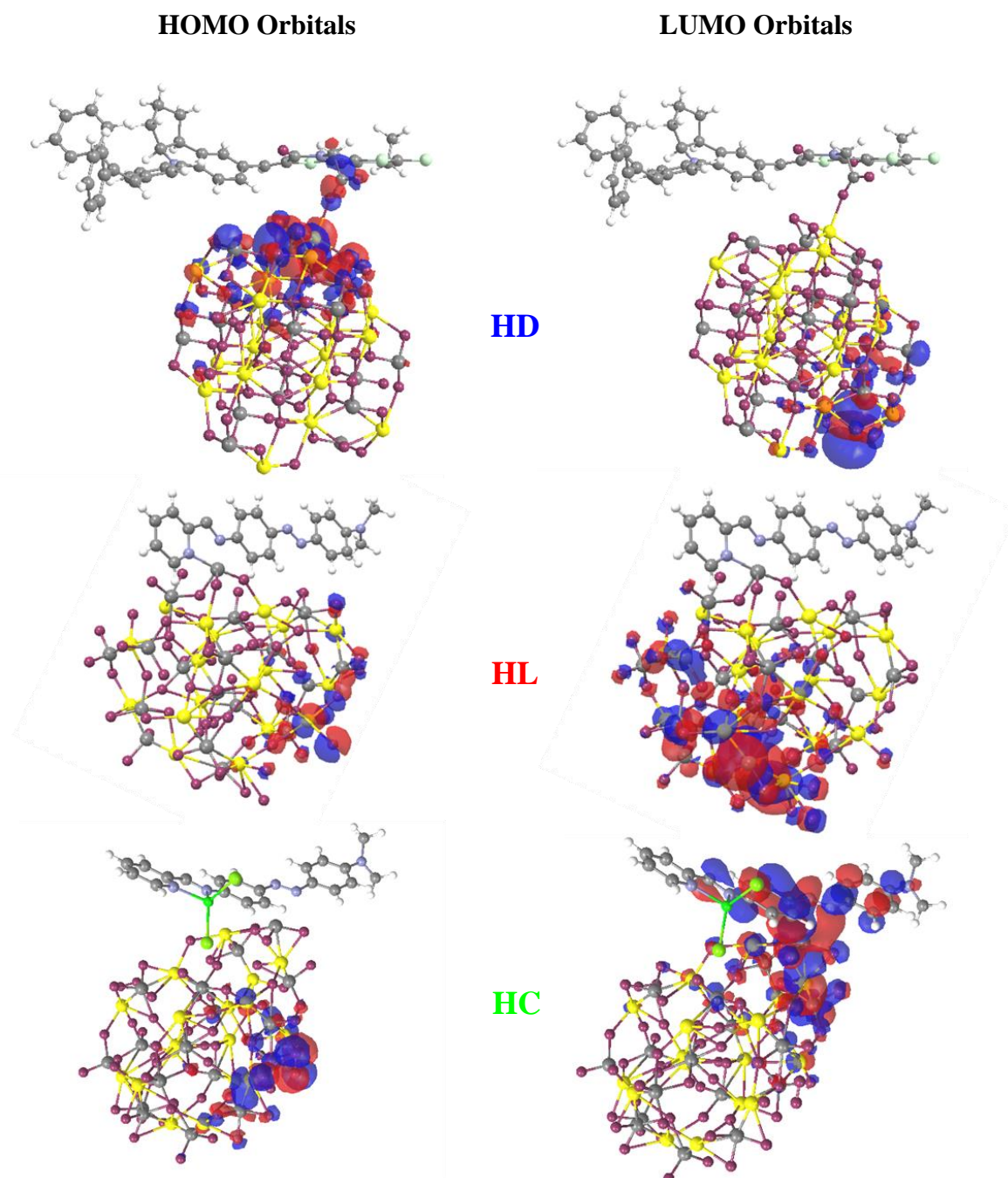


Figure 5.2.1.3. Representation of the HOMO and LUMO orbitals calculated for the $(\text{BiVO}_4)_{18}$ cluster sensitized by D149 (HD), LIGAND (HL) and COMPLEX (HC) molecules

The location of the HOMO and LUMO orbitals calculated for the optimized hybrid structures was also analyzed. In case of the $(\text{BiVO}_4)_{18}$ /D149 hybrid system (HD) the HOMO and LUMO orbitals are located at dye and nanocluster, respectively. The observed localization of the HOMO and LUMO orbitals leads to the photoactivation of the dye and in consequence to the photoinduced charge transfer from the D149 molecule to the BiVO_4 nanoparticle. In the case of $(\text{BiVO}_4)_{18}$ /LIGAND hybrid system (HL) the HOMO and LUMO orbitals are located at the BiVO_4 network.

This can possibly mean that the attached dye does not have significant effect on the charge transfer across the system. In this situation the dye molecule is not photoactive and the built system is not appropriate for the photocatalytic applications. Significant differences are also expressed in the $(\text{BiVO}_4)_{18}/\text{COMPLEX}$ system (HC), where the flow of charge occurs in the opposite direction than the appropriate one. In this case the HOMO orbital is located at the nanoparticle but the LUMO is distributed at the COMPLEX molecule. It gives the possibility to conclude that, a photoinduced electrons flow from the inorganic nanocrystal to the dye molecule can occur. In this way the photoactive charge current is blocked. Analyzing the data presented in **Fig. 5.2.1.3** it can be concluded that the most appropriate for the photocatalytic application is the $(\text{BiVO}_4)_{18}/\text{D149}$ hybrid system (HD).

Experimental Investigations

The AFM measurements were performed on both the morphology characterizations and the electrical activity KFM probed technique. Thus, tapping modesTM and KFM images of a square surface were recorded. They reveal both the topology and the electrical potential distributions on different BiVO_4 film surfaces. In consequence, experimental investigations of the BiVO_4 thin film surface morphology with anchored organic molecules showed that these nanoparticles are bigger in size than the pure bare samples. The drastic increase in particle size up to more than 70 nm illustrates significant importance of the binding agent in mesoporous thin film morphology. In addition, the analysis of the KFM measurements showed a net effect from the dye molecules on the surface potential distribution (**Fig. 5.2.1.4**). In all cases the analyzed area is $1\mu\text{m} \times 1\mu\text{m}$. The left panel of the **Fig. 5.2.1.4** presents the surface representation visualizing the shape and size of the nanoparticles with anchored dyes. The middle panel shows the KFM surface analysis without their illumination. The panel on the right side demonstrates the distribution of surface potential during sample exposure by irradiation. The highest potential value is equal to 60 mV. A characteristic phenomenon occurring here consists in blurring the surface potential, especially under visible radiation exposure. For the non-irradiated samples it is noted that the greatest potential is focused on the individual particles and corresponds closely to the surface repetition of the system (**Fig. 5.2.1.4**, middle panel). On the other hand, in the illuminated systems the potential is blurred and does not directly correlate with the surface morphology (**Fig. 5.2.1.4**, right panel – HD and HL).

The resulting differences could occur due to photoactivation of organic dyes anchored on the BiVO_4 surface. Electrons excited from the HOMO to LUMO levels of the organic molecules can be then transferred to the CB of the semiconductor. The increased amount of charge carriers on the surface could result in a free flow of surface charges. In the case of the $(\text{BiVO}_4)_{18}/\text{COMPLEX}$ hybrid (HC) the situation is different than it was observed for the HD and HL hybrids. The effect of the irradiation causes the reverse charge transfer reaction exhibiting the potential located at the individual BiVO_4 nanoparticles. These experimental data are in good agreement with the expected behavior from theoretical considerations. This may also illustrate the weak photoactive compatibility between the BiVO_4 thin film and the COMPLEX molecule.

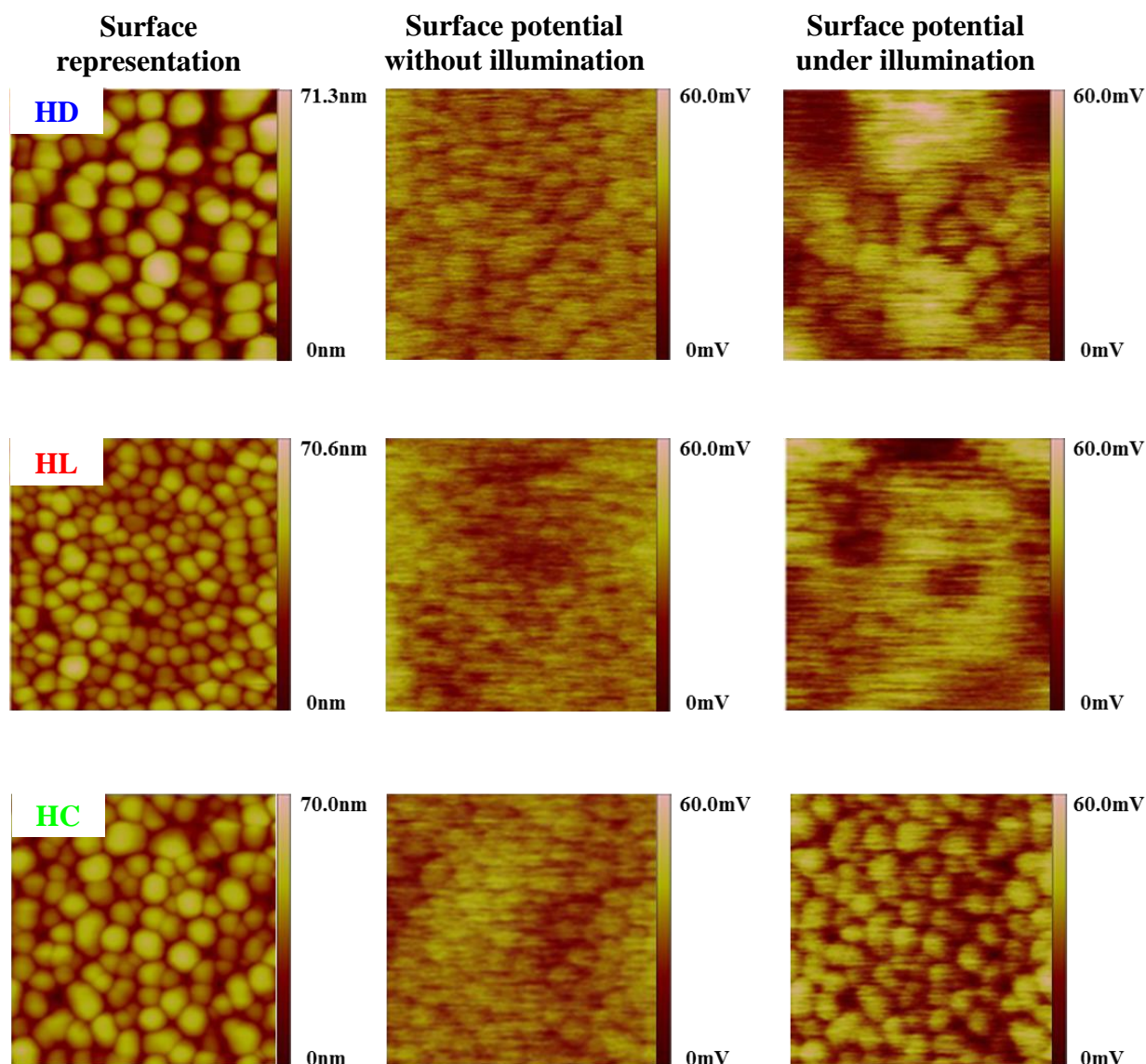


Figure 5.2.1.4. KFM measurements performed for the BiVO_4 thin films sensitized by organic dye molecules D149 (HD), LIGAND (HL) and COMPLEX (HC)

The described charge transfer model between the organic molecule and the semiconducting nanoparticles is based on the treatment of the hybrid system as the tandem of the two components, as described in the work of Hara et al. [52,53] The nature of the connection between the photocatalyst and the organic dye has been investigated for photovoltaic systems and was described as persistent chemical bonding [54,55].

The representative histograms illustrating the charge density distribution versus the surface electrical potential for the systems with anchored D149 molecules were performed. The KFM images presented in **Fig. 5.2.1.5.** demonstrate the occurrence of drastic changes on the electrical activity of the BiVO₄ based systems under light radiation. The maximum electrical potential undergoes a net change from 33/25 mV under dark to 35/55 mV with light exposure for the bare/sensitized thin films of the BiVO₄. The potential distribution changes critically between the bare BiVO₄ film surface and that with organic dyes.

The difference of surface potential between the bare and sensitized samples without radiation exposure was estimated to be equal to 8 mV. The justification was possible to be made taking into account the characteristic electronic phenomena such as the band bending, the Fermi levels pinning, the change on the work function expected at the organic/semiconducting heterojunction. The performed analysis is based on the donor-acceptor interfaces model using the electronic band alignment theory to account for the charge transfer mechanism.

Theoretical energy band diagram of the pure monoclinic BiVO₄ and the one with anchored organic dye is presented in **Fig. 5.2.1.6.** On the left side the mentioned figure shows the electronic band structure of the bare bismuth vanadate. The valence band and conduction band are placed at -7.29 eV and -4.79 eV, respectively, while the Fermi level is located at -5.29 eV (**Fig. 5.2.1.6.** left side) [56]. As reported by Chang et al. the BiVO₄ belongs to the n-type class of semiconductors, because its Fermi level is located closer to the conduction band (0.5 eV) than to the valence band (2.0 eV) [57]. The diagram on the left side illustrates also the work function Φ defined by the Fermi level and the vacuum level. The fact that the surface potential of sensitized systems may decrease is extremely important for describing the mechanism of the electric charge transfer process. The schema presented in **Fig. 5.2.1.6.** on the right panel shows the BiVO₄/organic dye heterojunction. The system presents a typical model of a hybrid system with the charge transfer between components.

The process proceeds by excitation of an electrons from the HOMO (-5.07 eV) to LUMO (-2.36 eV) level of the dye molecule and then transfer them to the semiconductor conduction band (-4.79 eV) [58].

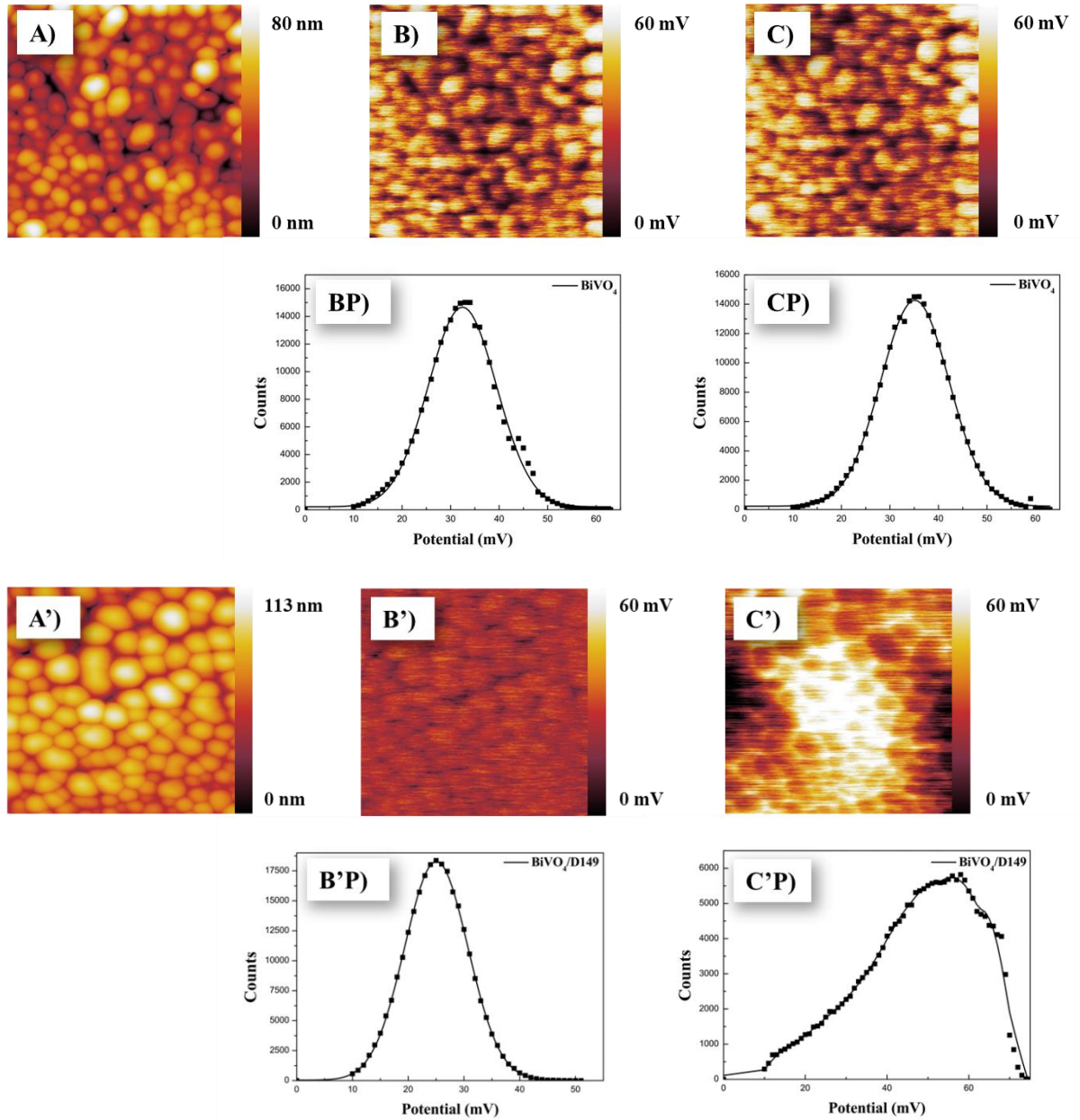


Figure 5.2.1.5. Topography (A, A') and surface potential distribution of the BiVO₄ thin films (B, C) and BiVO₄ with anchored D149 molecules (B', C') without illumination (B and B') and under illumination (C and C'). The histograms BP, CP, B'P, C'P represent the population of the charge distribution of the samples B, C, B', C', respectively

As a result of combining the inorganic and organic components in the BiVO₄/D149 system a new Fermi pinning level ($E_{F_{D-A}}$) is created. It is located above the Fermi level (E_F) of pure BiVO₄ and extends to the whole heterojunction system.

In the BiVO₄/D149 hybrid systems a donor-acceptor interface is produced by a chemical bond occurring between semiconductor and the organic molecule [59,60]. In this architecture design, the organic dye assumes the role of a donor, and the semiconductor material acts as an electron acceptor.

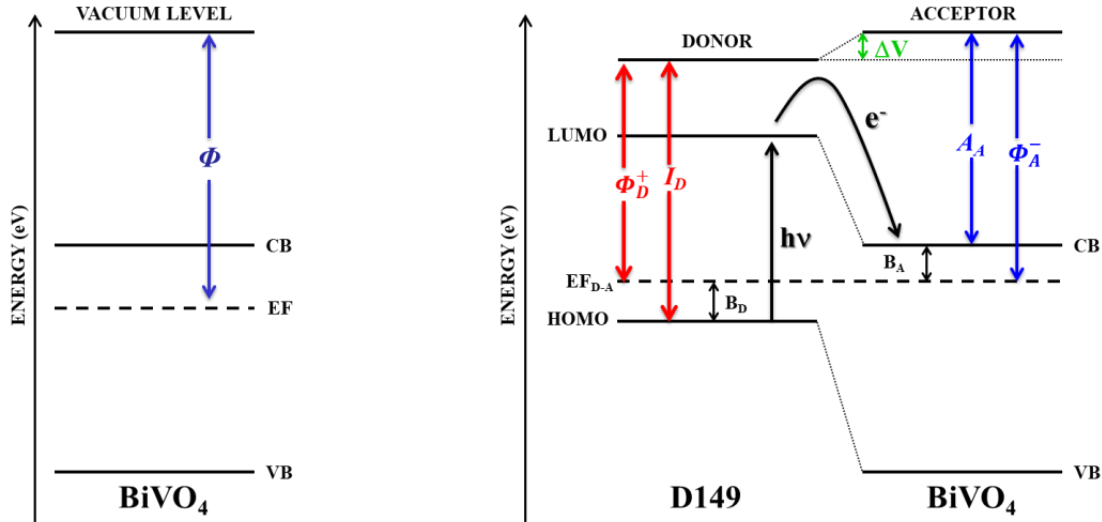
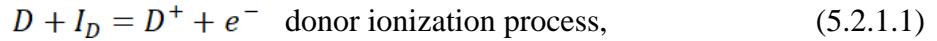


Figure 5.2.1.6. Theoretical energy band diagram and band alignment at the interface: case of virgin thin film of the BiVO₄ (left side) and sensitized donor-acceptor interface created by the D149 (right side)

Schematic processes in separating components are shown as follow:



Thus, the difference between the energy of the acceptor electron affinity and the donor ionization energy must be equal to potential difference (ΔV). Unfortunately, the change in surface potential cannot be described simply as a direct relationship between these two values confirmed by theoretical and experimental investigations [61]. In heterojunction appears an creation of the Fermi pinning level [62-64] causing the occurrence of additional correlations between the donor ionization energy and the acceptor electron affinity. The B_D and B_A describe the Coulomb energy of charge transfer of the newly formed EF_{D-A} band for the donor and acceptor, respectively. The correlation between the Coulomb energy and the potential change ΔV can be recorded in the following way:

$$\Delta V = (A_A + B_A) - (I_D - B_D) \quad (5.2.1.3)$$

Based on **Fig. 5.2.1.6**, the following relations can be established for the work function of donor and acceptor:

$$\Phi_A^- = A_A + B_A, \quad (5.2.1.4)$$

$$\Phi_D^+ = I_D - B_D. \quad (5.2.1.5)$$

Simultaneously the relation $\Phi_A^- - \Phi_D^+ = \Delta V$ holds only when $\Phi_A^- > \Phi_D^+$.

In conclusion, the main reason of the difference between surface potential in virgin and sensitized films may be related to the work function and its modification by the electrical peculiarities of anchored dyes. A higher work function in virgin BiVO₄ surface limits the charge transfer. At the donor-acceptor interfaces, it can be expected that electronic band alignment (Fermi pinning level) favours charge mobility and leads in that case to the observed drastic change of electrical potential distributions without additional illumination. Qualitatively, the above observations point out different behaviours of electrical activity on the BiVO₄ as function of the irradiation and the involvement of anchored dyes able to facilitate charge transfer through electronic modifications at the interface between the BiVO₄ surface and the sensitizing dyes.

5.2.2. Optical properties of the BiVO₄/dye thin films

An optical properties of the BiVO₄ thin films sensitized by organic dyes were investigated and the results are summarized in the **Fig. 5.2.2.1**. The extension of the optical spectra is enhanced in the spectral visible range up to 700 nm by using the dyes. This effect improves the applicability of the system for visible light driven photoactivity. The broad UV-vis absorption band measured for the BiVO₄/D149 system (HD) is located between 480 nm and 630 nm. The optical spectrum is composed by the absorption bands emanating from the inorganic thin film and the one related to the used organic dye (see **Fig. 5.2.2.1**). The appearance of the mentioned absorption band illustrates the influence of the dye on the sensitized network and traduces the involvement of charge transfer band as it was described by Hori et al. [65]. Similarly, the mentioned phenomenon occurs in the BiVO₄/LIGAND system (HL), but it can be seen that the effect of the dye in this case is not so significant as it is noticed for the HD hybrid system. Unfortunately, the COMPLEX attached to the BiVO₄ only changed the absorption spectrum of the system to a lesser extent. The change has not reached the limit of absorption, which is entirely in line with the absorption of the bare film of the BiVO₄ and no additional band that implies a charge transfer band is observed.

This allows to assume that the COMPLEX did not create a coherent system with semiconductor substrate and thus only settled on the surface by intermolecular interaction rather than chemical bonding. This may mean weak interactions between components of the system which, under the influence of external factors, can be separated into individual components.

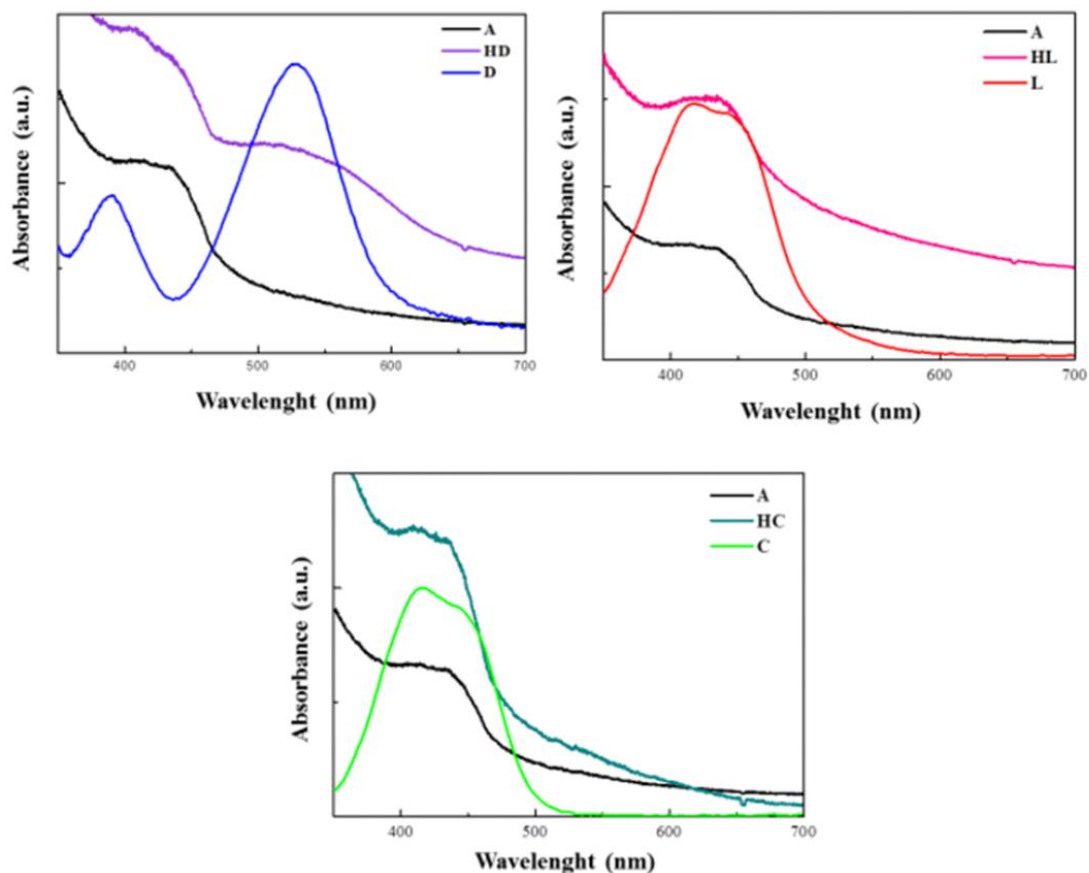


Figure 5.2.2.1. UV-vis absorption spectra measured for the BiVO₄ thin film (A), organic dyes D149 (D), LIGAND (L) and COMPLEX (C), and their hybrid systems HD, HL and HC solved in the acetonitrile/tertbutanol (1/1)

5.2.3. Impact of anchored organic dye molecules on the Raman activity

The structural properties of the investigated hybrids were studied by Raman method and the experimental data were compared to the theoretical calculations. The experimental Raman spectra (see **Fig. 5.2.3.1**) show significant differences between the vibrational bands positions and their intensities expected for the individual bonds or groups of atoms. The highest deviations were observed for the BiVO₄/LIGAND hybrid system. In the case of sensitized films by anchored dyes as D149 and COMPLEX, the main intense Raman band is assigned to symmetrical stretching of the V-O mode and is located approximately at the 850 cm⁻¹. From the theoretical Raman spectra calculations (**Fig. 5.2.3.1**, bottom panel) one may see that the main band is located at the 817 cm⁻¹

and corresponds to the symmetrical stretching of the V-O mode. While, the vibrations corresponding to the asymmetric stretching V-O are around 668 cm^{-1} and 728 cm^{-1} . Asymmetric and symmetric deformation of the VO_4^{3-} group occurs at 305 cm^{-1} and 678 cm^{-1} , respectively. On the other hand, the analysis of the $\text{BiVO}_4/\text{COMPLEX}$ system shows a negligible presence of the VO_4^{3-} symmetrical and asymmetric deformation. The Raman spectra analysis confirms that the D149 molecule is chemically bonded to the BiVO_4 nanostructure. The study of vibration properties confirms the above analysis which proved that the $\text{BiVO}_4/\text{D149}$ system has the best compatibility with the BiVO_4 mesoporous material to be used as photocatalyst.

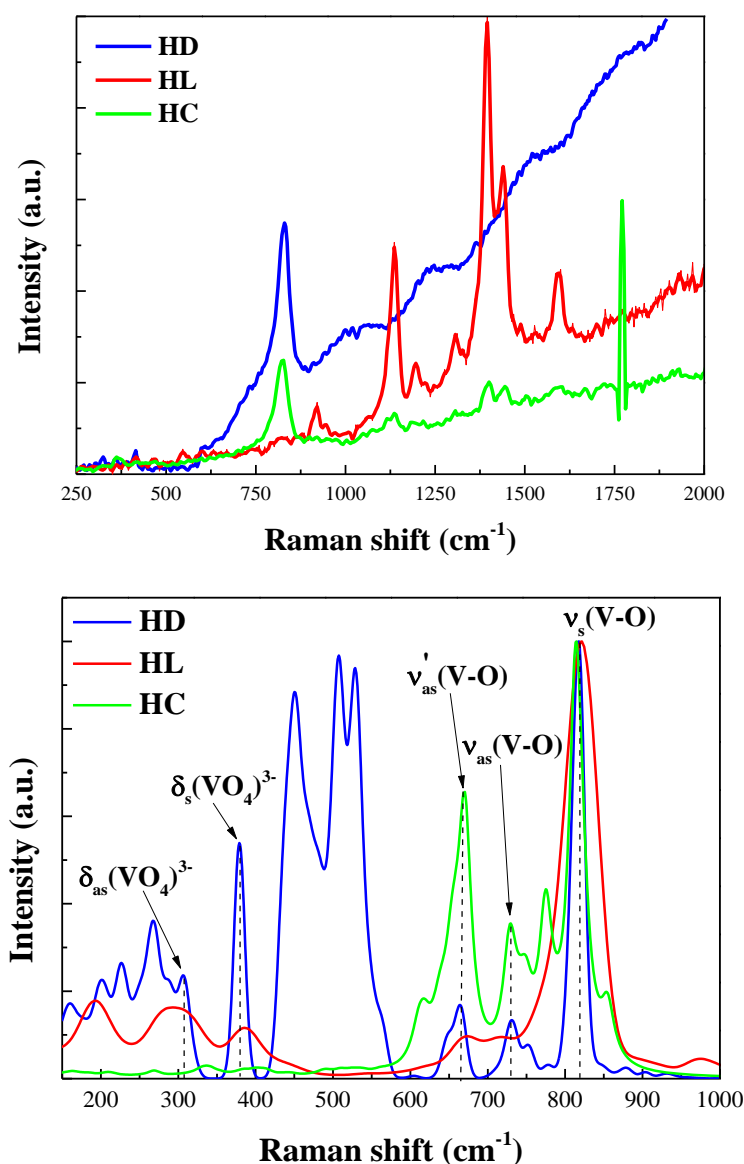


Figure 5.2.3.1. The experimental (top panel) and theoretical (bottom panel) Raman spectra obtained for the BiVO_4 based hybrid systems with anchored D149 (HD), LIGAND (HL) and COMPLEX (HC) dye molecules

5.2.4. Photocatalytic properties of the hybrid systems

The photocatalytic properties of the $\text{BiVO}_4/\text{D149}$, $\text{BiVO}_4/\text{LIGAND}$ and $\text{BiVO}_4/\text{COMPLEX}$ hybrids were investigated by the photocatalytic test performed by using the experimental setup described in **Chapter 4**. For this purpose, the considered samples were placed in a 10^{-5}mol/l methylene blue (MB) solution and irradiated by a Xe-lamp beam. Based on the observed MB absorption spectrum in solution, the evolution of dye concentration changes over time was obtained. As shown in **Fig. 5.2.4.1**, only a small photodegradation of the MB over time was seen and suggest quite low photoactivity of the hybrid films irrespective to the nature of the sensitizing dyes. Based on the dependence of $\ln(C_0/C)$ over time photocatalytic yields were determined.

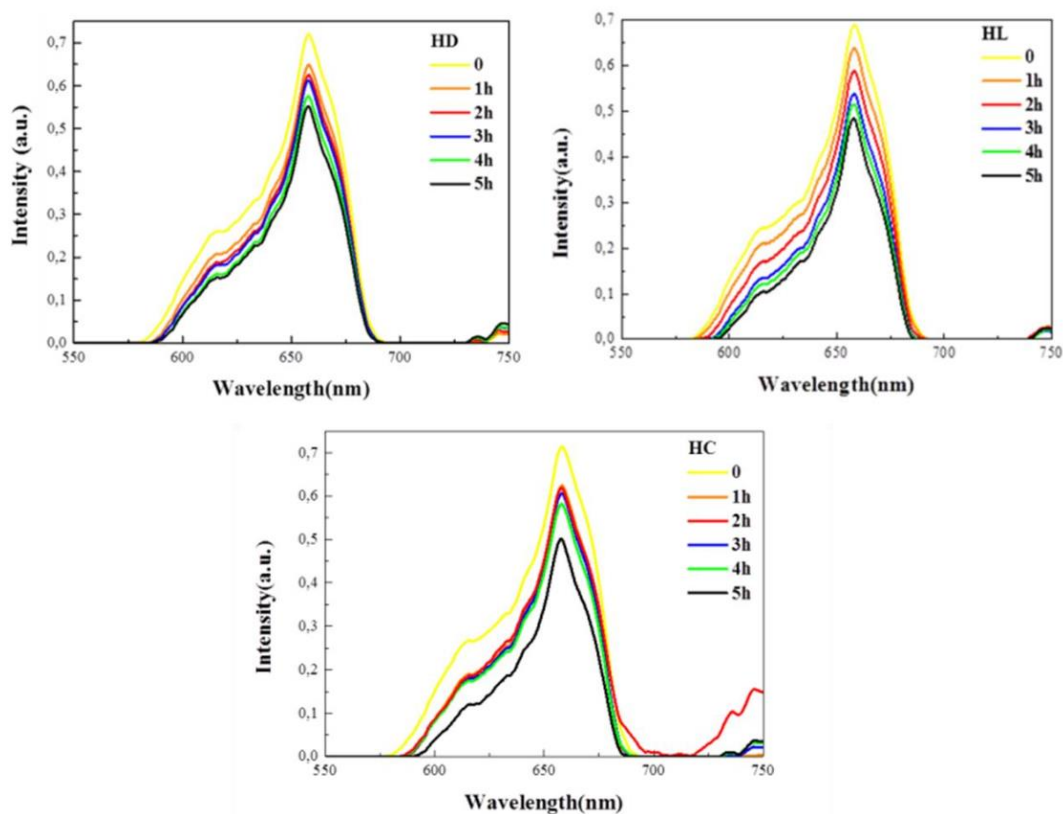


Figure 5.2.4.1. UV-vis absorption spectra measured for the HD, HC and HL hybrids in methylene blue solution

The photocatalytic activity of the BiVO_4 based hybrids was obtained as follow: 25% for $\text{BiVO}_4/\text{D149}$, 30% for $\text{BiVO}_4/\text{LIGAND}$ as well as for $\text{BiVO}_4/\text{COMPLEX}$ systems (**Fig. 5.2.4.2**).

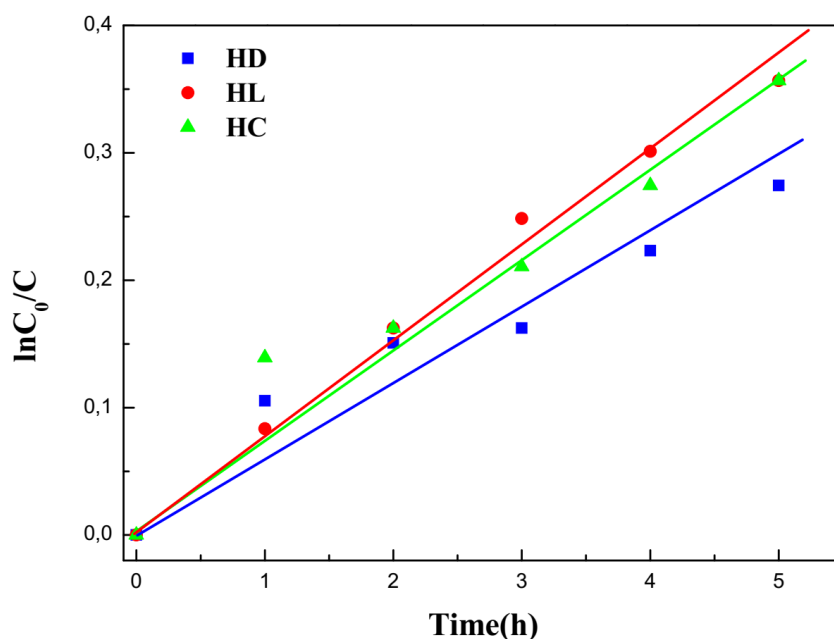


Figure 5.2.4.2. The MB degradation in time evaluated for the HD, HL and HC hybrid systems

The obtained values suggest that the photocatalytic processes observed in the investigated hybrids are less efficient than using the pure mesoporous BiVO₄ material. This may be due to the fact that most of the active surface of the photocatalyst has been stuck by attaching sensitizers to it. This means a smaller surface able to generate the active oxygen and hydroxyl radicals which cause the decomposition of organic molecules in solution. The absence of changes on MB absorption spectra in solution during the experiment indicates that the dyes did not penetrate the test solution and were adsorbed on the surface throughout the process, which means that the effect of increasing the concentration of dye in solution can be ruled out.

5.2.5. Conclusion

On the basis of a combined strategy of computational and experimental investigations, the transfer of electric charge between the dye molecules and the nanocrystals has been demonstrated. Only the BiVO₄ sensitized by the D149 molecules exhibits compatible electronic band alignment and it can be proposed to be used for the photoactivated processes and applications. In the case of materials sensitized by LIGAND and COMPLEX molecules, no significant changes in electronic or optical properties have been observed in relation to the bare BiVO₄ thin film.

The analysis using AFM instrumentation in connection with the investigations of the surface potential distribution (KFM) of mesoporous BiVO₄ sensitized with organic dye

molecules confirmed the previously obtained results of the theoretical analysis of the electron density distribution on the HOMO-LUMO orbital. The tests were carried out for the BiVO₄ thin film samples with anchored D149, LIGAND and COMPLEX molecules before and during additional sample irradiation. For the HD and HL samples, the surface potential under the additional irradiation is blurred, while for the HC sample the reverse phenomenon was observed. In this case the potential focused on the particles of the material which was confirmed comparing the image with the surface representation.

Analyzing the optical properties of the investigated hybrid systems, one may conclude that for the BiVO₄/D149 additional absorption band appears between 480 nm and 630 nm. The mentioned band corresponds to the absorption spectra of the D149. In this case the charge transfer band is observed indicating the influence of the sensitized organic molecule on the absorption capacity of the hybrid system. Anchored LIGAND and COMPLEX molecules do not create any additional absorption band. Probably it is caused by unstable connection between the organic and inorganic parts of the system.

Synthesized hybrid systems were tested as photocatalytic active materials.

Their photocatalytic capacity was estimated to be equal to 25% for the BiVO₄/D149 and 30% for the BiVO₄/LIGAND as well as for the BiVO₄/COMPLEX. The obtained values can prove effective blocking of the active surface of the photocatalyst by anchoring organic molecules on the surface of the BiVO₄. This may mean that the D149 connection process has been running with maximum efficiency.

5.3. References

- [1] Accelrys Inc, Materials Studio 8.0, 2017
- [2] Zo. Zhao, Z. Li, Z. Zou, Electronic structure and optical properties of monoclinic clinobisvanite BiVO₄, *Phys. Chem. Chem. Phys.* 2011, 13, 4746–4753
- [3] M.E. Grillo, J.W. Andzelm, N. Govind, G. Fitzgerald, K.B. Stark, Lecture Notes in Physics 10 Computational Materials Science with Materials Studio: Applications in Catalysis, 207-221
- [4] Segall, M. D.; Lindan, P. J. D.; Probert, M. J.; Pickard, C. J.; Hasnip, P. J.; Clark, S. J.; Payne, M. C.: First-principles simulation: ideas, illustrations and the CASTEP code. *J. Phys. Cond. Matter.* 14 (2002) 2717–2744

- [5] J. P. Perdew, K. Burke and M. Ernzerhof, Generalized Gradient Approximation Made Simple, *Phys. Rev. Lett.* 1996, 77, 3865-3868
- [6] H.J. Monkhorst, J.D. Pack, Special points for Brillouin-zone integrations, *Phys. Rev. B* 1976, 13, 5188- 5192
- [7] G. Kresse, D. Joubert, From ultrasoft pseudopotentials to the projector augmented-wave method, *Physical Review B* 1999, 59, 3, 1758-1775
- [8] P. Armand, J.Ch. Gilbert, S. Jan-Jégou, A BFGS-IP algorithm for solving strongly convex optimization problems with feasibility enforced by an exact penalty approach. *Mathematical Programming* 2002, 92, 393–424
- [9] J. Ma, L.-W. Wang, The role of the isolated 6s states in BiVO₄ on the electronic and atomic structures, *Appl. Phys. Lett.* 2014, 105, 172102(1-4)
- [10] Z. Zhao, Z. Li, Z. Zou, Electronic structure and optical properties of monoclinic clinobisvanite BiVO₄, *Phys. Chem. Chem. Phys.* 2011,13, 4746-4753
- [11] K. Ding, B. Chen, Y. Li, Y. Zhang, Z. Chen, J. Comparative density functional theory study on the electronic and optical properties of BiMO₄ (M $\frac{1}{4}$ V, Nb, Ta), *Mater.Chem. A* 2014, 2, 8294- 8303
- [12] R. Venkatesan, S. Velumani, A. Kassiba, Mechanochemical synthesis of nanostructured BiVO₄ and investigations of related features, *Mater. Chem. Phys.* 2012, 135, 842-848
- [13] J. K. Cooper, S. Gul, F. M. Toma, L. Chen, J. W. Ager, J. Yano, I. D. Sharp, Indirect bandgap and optical properties of monoclinic bismuth vanadate, *J. Phys. Chem. C* 2015, 119, 2969-2974
- [14] Z.-F. Huang, L. Pan, J.-J. Zou, X. Zhang, L. Wang, Nanostructured bismuth vanadate-based materials for solar-energy-driven water oxidation: a review on recent progress, *Nanoscale* 2014, 6, 14044-14079
- [15] Z. Zhao, W. Luo, Z. Li, Z. Zou, Density functional theory study of doping effects in monoclinic clinobisvanite BiVO₄, *Phys. Lett. A* 2010, 374, 4919-4927
- [16] A. Walsh, Y. Yan, M. N. Huda, M. M. Al-Jassim, S. H. Wei, Band Edge Electronic Structure of BiVO₄: Elucidating the Role of the Bi s and V d Orbitals, *Chem. Mater.* 2009, 21, 547-551

- [17] D. J. Payne, M. D. M. Robinson, R. G. Egdell, A. Walsh, J. McNulty, K. E. Smith, L. F. J. Piper, The nature of electron lone pairs in BiVO₄, *Appl. Phys. Lett.* 2011, 98, 212110(1-4)
- [18] L. Ren, L. Ma, L. Jin, J.-B. Wang, M. Qiu, Y. Yu, Template-free synthesis of BiVO₄ nanostructures: II. Relationship between various microstructures for monoclinic BiVO₄ and their photocatalytic activity for the degradation of rhodamine B under visible light, *Nanotechnology* 2009, 20, 405602-405611
- [19] A. Gajewicz, T. Puzyn, B. Rasulev, D. Leszczynska, J. Leszczynski, Metal Oxide Nanoparticles: Size-Dependence of Quantum-Mechanical Properties, *Nanoscience & Nanotechnology-Asia* 2011, 1, 53-58
- [20] M. J. Frisch, G. W. Trucks, H. B. Schlegel, G. E. Scuseria, M. A. Robb, J. R. Cheeseman, G. Scalmani, V. Barone, B. Mennucci, G. A. Petersson, H. Nakatsuji, M. Caricato, X. Li, H. P. Hratchian, A. F. Izmaylov, J. Bloino, G. Zheng, J. L. Sonnenberg, M. Hada, M. Ehara, K. Toyota, R. Fukuda, J. Hasegawa, M. Ishida, T. Nakajima, Y. Honda, O. Kitao, H. Nakai, T. Vreven, J. A. Montgomery, Jr., J. E. Peralta, F. Ogliaro, M. Bearpark, J. J. Heyd, E. Brothers, K. N. Kudin, V. N. Staroverov, R. Kobayashi, J. Normand, K. Raghavachari, A. Rendell, J. C. Burant, S. S. Iyengar, J. Tomasi, M. Cossi, N. Rega, J. M. Millam, M. Klene, J. E. Knox, J. B. Cross, V. Bakken, C. Adamo, J. Jaramillo, R. Gomperts, R. E. Stratmann, O. Yazyev, A. J. Austin, R. Cammi, C. Pomelli, J. W. Ochterski, R. L. Martin, K. Morokuma, V. G. Zakrzewski, G. A. Voth, P. Salvador, J. J. Dannenberg, S. Dapprich, A. D. Daniels, Ö. Farkas, J. B. Foresman, J. V. Ortiz, J. Cioslowski, and D. J. Fox, *Gaussian 09*, Gaussian, Inc., Wallingford CT, 2009
- [21] J.B. Foresman, Æ. Frisch, *Exploring Chemistry with Electronic Structure Methods*, Second Edition. U. S. A.: Gaussian, Inc. 1993
- [22] B. Delley, An all-electron numerical method for solving the local density functional for polyatomic molecules, *J. Chem. Phys.* 1990, 92, 508-517
- [23] B. Vlasisavljevich, L. Gagliardi, P. C. Burns, Understanding the Structure and Formation of Uranyl Peroxide Nanoclusters by Quantum Chemical Calculations, *J. Am. Chem. Soc.* 2010, 132, 14503–14508

- [24] S.T. Bromley, M.A. Zwijnenburg, Th. Maschmeyer, Fully Coordinated Silica Nanoclusters: $(\text{SiO}_2)_N$ Molecular Rings, *Phys. Rev. Lett.* 2003, 90, 3, 35502 (1-4)
- [25] R. Poteau, F. Spiegelmann, Calculation of the electronic spectrum of Li_2 using effective core pseudopotentials and dependent core polarization potentials, *J. Mol. Spectrosc* 1995, 171, 299-308
- [26] M. Makowska-Janusik, O. Gladii, A. Kassiba, J. Boucle, N. Herlin-Boime, Cluster Approach To Model Titanium Dioxide as Isolated or Organic Dye Sensitized Nanoobjects, *J. Phys. Chem. C* 2014, 118, 6009–6018
- [27] F. Jensen, Introduction to Computational Chemistry, *Wiley*, 2017, 428
- [28] K. V. R. Prasad, K. B. R. Varma, Dielectric, thermal and pyroelectric properties of ferroelectric bismuth vanadate single crystals, *Mater. Chem. Phys.* 1994, 38, 406-410
- [29] O.V. Kharissova, M. Osorio, M. Sánchez Vázquez, B.I. Kharisov, Computational chemistry calculations of stability for bismuth nanotubes, fullerene-like structures and hydrogen-containing nanostructures, *J Mol Model* 2012, 18, 3981–3992
- [30] S. Sarkar, K. K. Chattopadhyay, Size-dependent optical and dielectric properties of BiVO_4 nanocrystals, *Phys. E* 2012, 44, 1742-1746
- [31] S. Sarkar, N. S. Das and K. K. Chattopadhyay, Optical constants, dispersion energy parameters and dielectric properties of ultra-smooth nanocrystalline BiVO_4 thin films prepared by rf-magnetron sputtering, *Solid State Sci.* 2014, 33, 58-66
- [32] S. Donga, J. Feng, Y. Li, L. Hu, M. Liu, Y. Wang, Y. Pi, J. Sun, Shape-controlled synthesis of BiVO_4 hierarchical structures with unique natural-sunlight-driven photocatalytic activity, *Appl. Catal. B* 2014, 152–153, 413-424
- [33] X. Zhang, L. Du, H. Wang, X. Dong, X. Zhang, C. Ma, H. Ma, Highly ordered mesoporous BiVO_4 : Controllable ordering degree and super photocatalytic ability under visible light, *Microporous and Mesoporous Materials* 2013, 73 175-180

- [34] J. Haiyan, D. Hongxing, M. Xue, Z. Lei, D. Jiguang, J. Kemeng, Morphology-Dependent Photocatalytic Performance of Monoclinic BiVO₄ for Methyl Orange Degradation under Visible-Light Irradiation, *Chin. J. Catal.* 2011, 32, 939–949
- [35] X. Meng, L. Zhang, H. Dai, Z. Zhao, R. Zhang, Y. Liu, Surfactant-assisted hydrothermal fabrication and visible-light-driven photocatalytic degradation of methylene blue over multiple morphological BiVO₄ single-crystallites, *Mater. Chem. Phys.* 2011, 125, 59–65
- [36] E. Alarcón-Lladó, L. Chen, M. Hettick, N. Mashouf, Y. Lin, A. Javeya, J.W. Ager, BiVO₄ thin film photoanodes grown by chemical vapor deposition, *Phys. Chem. Chem. Phys.* 2014, 16, 1651-1657
- [37] S. Sun, W. Wang, D. Li, L. Zhang, D. Jiang, Solar Light Driven Pure Water Splitting on Quantum Sized BiVO₄ without any Cocatalyst, *ACS Catal.* 2014, 4, 3498–3503
- [38] S. Mouli Thalluri, C. Martinez Suarez, S. Hernández, S. Bensaid, G. Saracco, N. Russo Elucidation of important parameters of BiVO₄ responsible for photocatalytic O₂ evolution and insights about the rate of the catalytic process, *Chemical Engineering Journal* 2014, 245, 124–132
- [39] A. Zhang, J. Zhang, The effect of hydrothermal temperature on the synthesis of monoclinic bismuth vanadate powders, *Materials Science-Poland* 2009, 27, 4-1
- [40] T. Ohno, T. Tsubota, K. Nishijima, Z. Miyamoto, Degradation of Methylene Blue on Carbonate Species-doped TiO₂ Photocatalysts under Visible Light, *Chem. Lett.* 2004, 33, 6, 750-75
- [41] S. Yang, L. Gao, New Method to Prepare Nitrogen-Doped Titanium Dioxide and Its Photocatalytic Activities Irradiated by Visible Light, *J. Am. Ceram. Soc.* 2004, 87,9, 1803–1805
- [42] R. López, R. Gómez, Band-gap energy estimation from diffuse reflectance measurements on sol–gel and commercial TiO₂: a comparative study, *J Sol-Gel Sci Technol* 2012, 61, 1–7

- [43] C. Karunakaran, S. Kalaivani, P. Vinayagamoorthy, S. Dash, Electrical, optical and visible light-photocatalytic properties of monoclinic BiVO₄ nanoparticles synthesized hydrothermally at different pH, *Mater. Sci. Semicond. Process.* 2014, 21, 122–131
- [44] Y. H. Ng, A. Iwase, A. Kudo, R. Amal, Reducing Graphene Oxide on a Visible-Light BiVO₄ Photocatalyst for an Enhanced Photoelectrochemical Water Splitting, *J. Mater. Sci. Lett.* 2010,1, 2607–2612
- [45] T.-Y. Kim, N.-M. Park, K.-H. Kim, Y.-W. Ok, T.-Y. Seong, C.J. Choi, G.Y. Sung, Quantum confinement effect of silicon nanocrystals in situ grown in silicon nitride films, *Appl. Phys. Lett.* 2004, 85, 5355- 5357
- [46] W.W. Yu, L. Qu, W. Guo, X. Peng, Experimental Determination of the Extinction Coefficient of CdTe, CdSe, and CdS Nanocrystals, *Chem. Mater.* 2003, 15, 2854-2860
- [47] M. Makowska-Janusik, A. Kassiba, J. Bouclé, J. F. Bardeau, S. Kodjikian, A. Désert, Vibrational density of states in silicon carbide nanoparticles: experiments and numerical simulations, *J. Phys.: Condens. Matter* 2005, 17, 5101–5110
- [48] M. A. Ruiz Preciado, A. Kassiba, A. Morales-Acevedo, M. Makowska-Janusik, Vibrational and electronic peculiarities of NiTiO₃ nanostructures inferred from first principle calculations, *RSC Adv.* 2015, 5, 17396–17404
- [49] I. Guezguez, A. Ayadi, K. Ordon , K. Iliopoulos, D. G. Branzea, A. Migalska-Zalas, M. Makowska-Janusik , A. El-Ghayoury, B. Sahraoui, Zinc induced a dramatic enhancement of the non-linear optical properties of an azo-based iminopyridine ligand, *J. Phys. Chem. C* 2014, 118, 14, 7545–7553
- [50] J.J. P. Stewart, Optimization of parameters for semiempirical methods V: Modification of NDDO approximations and application to 70 elements, *J Mol Model* 2007, 13,1173–1213
- [51] F.Jensen, Introduction to Computational Chemistry, Wiley, 2017, 428
- [52] K. Hara, M. Kurashige, Y. Danoh, C. Kasada, A. Shinpo, S. Suga, K. Sayama, H. Arakawa, Design of new coumarin dyes having thiophene moieties for highly efficient organic-dye-sensitized solar cells, *New J. Chem.* 2003, 27, 783–785

- [53] J.M. Macak, M. Zlamal, J. Krysa, P. Schmuk, Self-Organized TiO₂ Nanotube Layers as Highly Efficient Photocatalysts, *Small* 2007, 3, 2, 300–304
- [54] T. Hannappel, B. Burfeindt, W. Storck, F. Willig, Measurement of Ultrafast Photoinduced Electron Transfer from Chemically Anchored Ru-Dye Molecules into Empty Electronic States in a Colloidal Anatase TiO₂ Film, *J. Phys. Chem. B* 1997, 101, 6799-6802
- [55] F. Sauvage, D. Chen, Pa. Comte, F. Huang, L.-P. Heiniger, Y.-B. Cheng, R. A. Caruso, M. Graetzel, Dye-Sensitized Solar Cells Employing a Single Film of Mesoporous TiO₂ Beads Achieve Power Conversion Efficiencies Over 10%, *ACSNANO* 2010, 4, 8, 4420–4425
- [56] I.D. Sharp, J.K. Cooper, F.M. Toma, R. Buonsanti, Bismuth Vanadate as a Platform for Accelerating Discovery and Development of Complex Transition-Metal Oxide Photoanodes *ACS Energy Lett.* 2017, 2, 139–150
- [57] X. Chang, T. Wang, P. Zhang, J. Zhang, A. Li, J. Gong, Enhanced Surface Reaction Kinetics and Charge Separation of p–n Heterojunction Co₃O₄/BiVO₄ Photoanodes, *J. Am. Chem. Soc.* 2015, 137, 8356–8359
- [58] X.-F. Ren, J. Zhang, G.-J. Kang, Theoretical Studies of Electronic Structure and Photophysical Properties of a Series of Indoline Dyes with Triphenylamine Ligand, *Journal of Nanomaterials* 2015, 1-9
- [59] K. Kakiage, Y. Aoyama, T. Yano, T. Otsuka, T. Kyomen, M. Unnoc, M. Hanaya, An achievement of over 12 percent efficiency in an organic dye-sensitized solar cell, *Chem. Commun.* 2014, 50, 6379-6381
- [60] G. Chen, K. Zheng, X. Mo, D. Sun, Q. Meng, G. Chen, Metal-free indoline dye sensitized zinc oxide nanowires solar cell, *Mater. Lett.* 2010, 64, 1336–1339
- [61] D. Çakir, M. Bokdam, M.P. de Jong, M. Fahlman, G. Brocks, Modeling charge transfer at organic donor-acceptor semiconductor interfaces, *Appl. Phys. Lett.* 2012, 100, 203302(1-4)
- [62] C.C. Hobbs, L.R. C. Fonseca, A. Knizhnik, V. Dhandapani, Fermi-Level Pinning at the Polysilicon/Metal Oxide Interface-Part I, *IEEE Transactions On Electron Devices* 2004, 51, 971 – 977

- [63] Z. Liu, M. Kobayashi, B.C. Paul, Z. Bao, Y. Nishi, Contact engineering for organic semiconductor devices via Fermi level depinning at the metal-organic interface, *Physical Review B* 2010, 82, 035311(1-6)
- [64] H. Peisert, A. Petr, L. Dunsch, T. Chass, M. Knupfer, Interface Fermi Level Pinning at Contacts Between PEDOT: PSS and Molecular Organic Semiconductors, *ChemPhysChem* 2007, 8, 386 – 390
- [65] T. Hori, H. Moritou, N. Fukuoka, J. Sakamoto, A. Fujii, M. Ozaki, Photovoltaic Properties in Interpenetrating Heterojunction Organic Solar Cells Utilizing MoO₃ and ZnO Charge Transport Buffer Layers, *Materials* 2010, 3, 4915-4921

Chapter 6

General Conclusions

The thesis work concerns the investigations of mesoporous materials based on BiVO_4 sensitized by selected organic dyes to form hybrid functional materials. The performed investigations start from a synthesis of mesoporous samples as powders or thin films and the experimental investigations of their electronic, optical and structural properties. As relevant support for experiments, computer simulations and quantum-chemical calculations were used to shed light on the photoinduced charge transfer phenomena. Quantum-chemical calculations illustrate exhaustively the effect of individual components of the hybrid systems on their electronic and optical properties. They contribute to quantitative interpretation of the mechanism of photoinduced electric charge transfer involved in the investigated hybrid materials. Thus, it was shown that the combination of experimental and theoretical approaches draws precise roadmap of the physical phenomena that govern the photocatalytic properties of the BiVO_4 . The quantum-chemical calculations performed for the bulk BiVO_4 single crystal gives the following results:

1. The calculated electronic properties of the bulk BiVO_4 depend on the computational procedure implemented in quantum-chemical codes. The significant influence on the electronic properties of the investigated material lies in Bi–O and V–O bond lengths and their tendency to be symmetrical following the optimization procedure. The possible reason for such isotropic bond lengths arrangement in the case of the Bi–O is due to the strong correlation between the Bi 6s and the O 2p orbitals.
2. The calculations showed that the features of the evaluated energy band are similar for both the optimized and frozen BiVO_4 structure as well. Nevertheless, the energy band gap for the optimized structure is lower by 0.24 eV compared to that of the frozen structure.

3. In semiconducting oxides, the valence band formed by localized oxygen p orbitals leads to an increase in the effective mass of the holes. As the valence band of the BiVO_4 is hybridized by the O 2p and Bi 6s electrons, a strong correlation between them causes a decrease in the effective mass of the holes and an increase in their mobility. Light mass of holes is expected to facilitate efficient photoinduced charge separation and mobility, suggesting a possibility of high quantum efficiency in photocatalysis. This low effective mass facilitates the migration of the charge carriers as electrons and holes to the surface of the photocatalyst inducing then the redox formation of radicals.

The performed work uses the appropriate methodology for the investigation of the electronic properties of the nanostructured BiVO_4 as nanoparticles or mesoporous-like BiVO_4 . The relevant results are hereafter outlined:

4. The changes of the $\Delta E_{\text{HOMO-LUMO}}$ calculated for the BiVO_4 nanoparticles following the size changes exhibit size quantum confinement effects. The obtained data are in agreement with the results presented in already reported literatures. These results suggest that the considered nanosized clusters must have an amorphous fraction at their surface and a crystalline order in their core part. Such nano-objects reflect the nature of the BiVO_4 nanostructures. The performed calculations for partially reconstructed cluster surfaces show that for nanoparticles smaller than 1.1 nm their physical peculiarities are generally dominated by surface effects. For larger particles (sizes above 1.8 nm), the surface influence is less pronounced compared to core atoms, being located at the same coordinates as those involved in bulk crystal structure.
5. The quantum-chemical calculations point out that the HOMO orbital is built by the O 2p states and the LUMO is created by V 3d orbitals. Compared to the bulk material one could conclude that the size reduction of the BiVO_4 cluster does not drastically change its electronic properties.
6. The HOMO and LUMO orbitals spread at the surface of the cluster and confirm the key role of the surface in the photoactivated processes of electron transitions from HOMO to LUMO orbitals. Increasing the contact surface of nanoparticles with surrounding environment by synthesising meso- or nanoporous materials, will also improve the photocatalytic performances.

The above presented theoretical analysis of the electronic properties of the BiVO₄ nanostructures underlines the relevance of mesoporous bismuth vanadate to enhance the photocatalytic activity. In this case the experimental synthesis of mesoporous samples was realized by using the surfactant P123. This synthesis method stabilizes the crystalline monoclinic sheelite structure in the mesoporous powder. For the thin films synthesis, the role of the substrate is also a matter of interest due to its effect on the morphology of the films as revealed from the shape and sizes of the experimental work for the deposition of BiVO₄ particles. The UV-vis absorption spectra obtained for films deposited on borofloat substrate are located in the range 350 - 470 nm, i.e. a fraction of visible spectral range can be harvested. The experimental band gap for BiVO₄ thin films estimated from the Kubelka-Munk model was found equal to 2.55 eV in agreement with theoretical prediction (2.60 eV) obtained by using the semi-empirical PM6 parameterized method performed on partially reconstructed (BiVO₄)₁₈ cluster with a size of 1.2 nm. The surface of the partially reconstructed nanoparticle was modified according to the environmental effect of the interacting bismuth vanadate. In this case, the implemented cluster model of partially modified structures is a good model for a mesoporous material to predict its electronic and optical properties.

For the hybrid systems dedicated to improve the photocatalytic properties of the BiVO₄ based nanostructures, dyes molecules were anchored on the inorganic surfaces. The relevant investigations are summarized as follows:

7. The chosen dyes are labelled as D149, LIGAND and COMPLEX which are polar molecules with separated HOMO and LUMO orbitals. An excitation by light irradiation generates a shift of the electronic distribution from the middle of the organic group to the anchoring moieties, thus favouring electron injection from dye to BiVO₄.
8. The location of the HOMO and LUMO orbitals calculated for the hybrid structures was analysed. In the case of (BiVO₄)₁₈/D149, it was observed that the localization of the HOMO and LUMO orbitals leads to the photoactivation of the dye and in consequence to the photoinduced charge transfer from the D149 molecule to BiVO₄ nanoparticle. In the case of (BiVO₄)₁₈/LIGAND, the HOMO and LUMO orbitals are located in the BiVO₄ network. This suggests that the anchored dye does not have significant effect on the charge transfer across the system. In this situation the dye molecule is not photoactive and the built system is not appropriate for the photocatalytic applications. In the case of the

(BiVO₄)₁₈/COMPLEX, the HOMO orbital is located at the nanoparticle but the LUMO spreads on the COMPLEX molecule. This suggests that, a photoinduced electrons flow from the inorganic nanocrystal to the dye molecule limiting then the redox reactions which can manifest at the level of the inorganic network. Thus, the obtained numerical predictions point out the relevance of the (BiVO₄)₁₈/D149 hybrid system for photocatalytic activity.

9. The system based on the BiVO₄ sensitized by D149 molecules exhibits compatible electronic band alignment suitable for the photoactivated processes. In the case of materials sensitized by LIGAND and COMPLEX molecules, no significant changes in electronic or optical properties have been observed compared to the bare BiVO₄ thin film.
10. AFM and KFM measurements on the hybrid systems confirmed the theoretically predicted results and the model of the photoinduced charge transfer from dye to nanostructure was validated.
11. Analysing the UV-vis absorption spectra for the (BiVO₄)₁₈/D149 hybrid system shows that the charge transfer band traduces the influence of the sensitized organic molecule on the absorption capacity of the hybrid systems. Anchored LIGAND and COMPLEX molecules do not create any additional absorption band.
12. The investigated hybrid systems were experimentally tested as photocatalytic active materials. Their photocatalytic activity was estimated from the degradation ratio of methylene blue (MB) in solutions. This ratio varies from 25 % for BiVO₄/D149 to 30% for BiVO₄/LIGAND similarly to BiVO₄/COMPLEX. These measurements were realized in the configuration where the dyes cover the inorganic surfaces in contact with the (MB) solutions. It would be relevant to proceed by using sensitized powders or alternatively free standing films sensitized by D149. This is a part of the perspectives of future developments based on the already carried out work.

To sum up, mesoporous BiVO₄ materials are promising systems for photocatalysis due to the design of large contact surface required in heterogeneous catalysis with a high efficiency. The methodology of sensitizing the inorganic surfaces by charge transfer dyes was implemented and investigated theoretically by relevant numerical methods along with experimental realization of the considered hybrid systems. This work paves the way for future development to realize efficient photocatalysts with competitive

performances compared to the traditional wide band gaps semiconducting oxides as TiO_2 or ZnO which harvest only UV radiation.

For the near future, the investigations can be devoted to the photoefficiency of the new functionalized hybrid materials. It is also worth noting that selected transition metal elements may also be considered to modulate the electronic and optical features of the BiVO_4 materials. The goal will be to find the metal ions doping compatible with BiVO_4 mesoporous architectures giving the best photocatalytic efficiencies. This approach will open potential applications of these systems in the environment preservation as for water depollution or for new sources of energy through photocatalytic production of hydrogen.

List of Figures

Figure 1.2.1.1.	Photocatalytic efficiency of ZnO/Cu ₂ O based photocatalysts in the photodegradation of methyl orange.....	6
Figure 1.2.1.2.	Rates of photocatalytic degradation of Rhodamine B concentration [C(t)] by ZnO/carbon nanofiber (mass ratio ZnO: carbon electrospun nanofibers for ZC1- 4:1 and ZC2- 8:1).....	6
Figure 1.2.2.1.	Smooth and porous surface.....	8
Figure 1.2.2.2.	HOMO–LUMO energy gap splitting vs size calculated by the density functional theory methods as GGA and TDLDA for unpassivated (TiO ₂) _n anatase structures.....	10
Figure 1.2.3.1.	Local coordination of V and Bi ions in (a) tetragonal scheelite (t-s), (b) monoclinic scheelite (m-s), (c) and zircon–type (z-t) of BiVO ₄ structure. The bond lengths are demonstrated in Å (red: V, purple: Bi, and gray: O).....	11
Figure 1.2.3.2.	Representation of the of BiVO ₄ crystal structure (blue: Bi, red: O, green: V). The base centered monoclinic primitive cell is indicated by the dashed black lines.....	11
Figure 1.2.3.3.	Partial density of states (PDOS) for the monoclinic BiVO ₄ crystal form.....	12
Figure 1.2.3.4.	The calculated band structure (left) and PDOS (right) of monoclinic BiVO ₄	12
Figure 1.2.3.5.	UV-Vis absorption spectra of the BiVO ₄ thin films annealed at 400, 500 and 600°C with a ramping rate of 3°C/min (left) and the calculated band gap extrapolation according to UV-Vis absorption spectra and Kubelka-Munk function (right)...	14
Figure 1.2.4.1.	SEM images of BiVO ₄ prepared by the sol-gel method calcinated at a) 400°C b) 450°C c) 400°C.....	16
Figure 1.2.4.2.	SEM images of the BiVO ₄ prepared by the hydrothermal method. Autoclave was heated at a) 120°C, 6h b) 120°C, 12h c) 160°C, 24h	16

Figure 1.2.4.3.	SEM images of porous BiVO ₄ synthesized with surfactant a) DMMP b) P123 porous silica template c) silica fiber immobilized-CNFs polymer d) colloidal PS spheres e) PVA f) PS balls.....	17
Figure 1.2.5.1.	Photocatalytic evolution of the O ₂ from aqueous AgNO ₃ solutions (0.05 mol/L, 320 mL) under visible light irradiation ($\lambda > 420$ nm) (left) and under ultraviolet light irradiation ($300 < \lambda < 380$ nm) (right) on (a) tetragonal BiVO ₄ and (b) monoclinic BiVO ₄ structure.....	19
Figure 1.3.1.	Schematic diagram for the charge transfer under radiation for the hybrid organic/inorganic system.....	25
Figure 4.1.1.	Annealing process applied during the thin film preparation of the BiVO ₄	84
Figure 4.1.2.	Diagram of production of thin layers of BiVO ₄ deposited by dip coating on borofloat substrate.....	85
Figure 5.1.1.1.	Electron energy structure calculated by DFT/PBE methodology of monoclinic frozen BiVO ₄ structure.....	91
Figure 5.1.1.2.	The PDOS calculated by DFT/PBE method for relaxed (left panel) and frozen BiVO ₄ structure.....	93
Figure 5.1.1.3.	Structure of (BiVO ₄) ₂₆ nanocrystal with size 1.3 nm projected along [010] crystallographic direction.....	94
Figure 5.1.1.4.	The $\Delta E_{HOMO-LUMO}$ energy gap splitting vs size calculated by PM6 semi-empirical method for frozen and optimised BiVO ₄ cluster represented by the number of (BiVO ₄) _n units.....	96
Figure 5.1.1.5.	The energy gap splitting ($\Delta E_{HOMO-LUMO}$) versus size of the system calculated by PM6 method for (BiVO ₄) _n for surface and bulk representations.....	97
Figure 5.1.1.6.	The partial density of states calculated by PM6 semi-empirical method for the partially reconstructed cluster with size 1.2 nm	100
Figure 5.1.1.7.	XRD analysis of the BiVO ₄ powder synthesized by using P123 (A) and F127 (B) surfactant.....	101
Figure 5.1.1.8.	XRD pattern of mesoporous BiVO ₄ thin film prepared by using P123 as surfactant (A). Also shown the standard pattern JCPDS-14-0688 which assign the crystalline structure of BiVO ₄ to monoclinic scheelite phase.....	102

Figure 5.1.1.9.	SEM images of the thin films of monoclinic BiVO ₄ deposited on the silicon (a and b) and on borofloat substrates (c and d) using the dip coating method.....	103
Figure 5.1.1.10.	AFM image of the thin film of BiVO ₄ deposited on a borofloat substrate. The analyzed sample size is about size 1μm x 1μm.....	104
Figure 5.1.2.1.	The UV-vis absorption spectra measured for the borofloat (BF) and the thin film of the monoclinic BiVO ₄ deposited on the borofloat substrate.....	105
Figure 5.1.2.2.	(Top panel) Theoretical UV-vis absorption spectra calculated for bulk (solid line) and nanosized (dashed line) BiVO ₄ structures by using DFT/PBE and semi-empirical PM6 parameterised method, respectively. (Bottom panel) Tauc plot of [F(R)hv] ² versus hv for the of BiVO ₄ monoclinic thin film deposited on the borofloat substrate.....	107
Figure 5.1.3.1.	IR spectra calculated by PM6 methodology for frozen (top panel) and optimised (bottom panel) (BiVO ₄) _n clusters of different sizes.....	108
Figure 5.1.3.2.	Raman spectra calculated by PM6 methodology for frozen (top panel) and optimized (bottom panel) (BiVO ₄) _n clusters....	110
Figure 5.1.3.3.	Raman spectra calculated by PM6 methodology for frozen (black solid line) and optimised (black dashed line) (BiVO ₄) _n clusters and the experimental one (red line).....	112
Figure 5.1.4.1.	UV-vis spectra of degradation methylene blue dyes in solution by thin film of monoclinic BiVO ₄ under irradiation.....	113
Figure 5.1.4.2.	Kinetics of the degradation of the MB dyes obtained from the time evolution of the intensity of the absorption band related to MB dyes in a solution.....	113
Figure 5.2.1.1.	Structure of the organic dye molecules: D149, LIGAND and COMPLEX.....	117
Figure 5.2.1.2.	The HOMO and LUMO orbitals of the D149, LIGAND and COMPLEX organic dyes molecules calculated by the semiempirical PM6 parameterized method.....	119
Figure 5.2.1.3.	Representation of the HOMO and LUMO orbitals calculated for the (BiVO ₄) ₁₈ cluster sensibilized by D149 (HD), LIGAND (HL) and COMPLEX (HC) molecules.....	120

Figure 5.2.1.4.	KFM measurements performed for the BiVO ₄ thin films sensitized by organic dye molecules D149 (HD), LIGAND (HL) and COMPLEX (HC).....	122
Figure 5.2.1.5.	Topography (A, A') and surface potential distribution of BiVO ₄ thin films (B, C) and BiVO ₄ with anchored D149 (B', C') without illumination (B and B') and under illumination (C and C'). The histograms BP, CP, B'P, C'P represent the population of the charge distribution of the samples B, C, B', C', respectively.....	124
Figure 5.2.1.6.	Theoretical energy band diagram and band alignment at the interface: case of virgin thin film of the BiVO ₄ (left side) and sensitized donor-acceptor interface created by the D149 (right side).....	125
Figure 5.2.2.1.	UV-vis absorption spectra measured for the BiVO ₄ thin film (A), organic dyes D149 (D), LIGAND (L) and COMPLEX (C), and their hybrid systems HD, HL and HC solved in the acetonitrile/tertbutanol (1/1).....	127
Figure 5.2.3.1.	The experimental (top panel) and theoretical (bottom panel) Raman spectra obtained for the BiVO ₄ based hybrid systems with anchored D149 (HD), LIGAND (HL) and COMPLEX (HC) dye molecules.....	128
Figure 5.2.4.1.	UV-vis absorption spectra measured for the HD, HC and HL hybrids in methylene blue solution.....	129
Figure 5.2.4.2.	The MB degradation in time evaluated for the HD, HL and HC hybrid systems.....	130

List of Tables

Table 1.2.5.1.	Summary of several monoclinic BiVO ₄ samples synthesized by different routes relative to the photocatalytic efficiency.....	21
Table 5.1.1.1.	Lengths of the Bi-O and V-O bonds as well as lattice parameters for the frozen and relaxed structure of BiVO ₄ single crystal.....	90
Table 5.1.1.2.	The HOMO and LUMO orbitals representation of (BiVO ₄) _n frozen clusters with <i>n</i> = 12, 18, 24, 30, 36 calculated by the PM6 parametrised method.....	99
Table 5.1.3.1.	Maximum of Raman Intensity - location of symmetrical stretching of V-O mode for the structure after and without optimization process.....	111

List of Schemas

Schema 1.1.	The system of dependencies of physics fields on which photocatalysis is based.....	1
Schema 1.1.1.	Processes occurring in the semiconductor after absorption of suitable radiation.....	3
Schema 1.1.2.	Location of valence and conduction band for the selected semiconducting oxides used as photocatalysts and redox potentials for water species.....	3
Schema 1.2.1.1	Band structure of the zinc oxide and titanium dioxide.....	5
Schema 3.1.1.	An exemplary arrangement of atoms in a crystalline lattice with the designed different groups (families) of mutually parallel crystallographic planes.....	58
Schema 3.1.2.	Diagram of X-ray reflection from two parallel atomic planes.....	58
Schema 3.1.3.	a) X-ray Diffraction from a single crystal, b) Diffraction reflections from a polycrystalline (powder) sample consisting of a large number of fine, randomly oriented crystallites.....	60
Schema 3.2.1.	Effect of an electron beam on a sample surface.....	62
Schema 3.2.2.	Range and spatial distribution of emission of different types of electrons in a sample.....	62
Schema 3.3.1.	(a) Force curve versus interatomic distance in AFM (b) contact mode (c) non-contact mode.....	64
Schema 3.5.1.	Diagram of electron, vibration and rotation transitions in a diatomic molecule. E_n are electron levels, V_n are vibration levels, I_n are rotational levels, <i>a</i> - illustrates electronic, <i>b</i> - vibration, <i>c</i> – rotational transitions.....	69
Schema 3.6.1.	Diagram of energy presenting different types of scattering..	74

